Atomic Quantum Metrology with Narrowband Entangled and Squeezed States of Light

DISSERTATION

submitted for the degree of
Doctor of Philosophy
by
Florian Wolfgramm

ICFO - The Institute of Photonic Sciences
UPC - Universitat Politècnica de Catalunya

Thesis Advisor: Prof. Dr. Morgan W. Mitchell

Barcelona, December 2011

Abstract

The use of light, especially of laser light, is in many cases the most sensitive way to perform measurements. However, the highest sensitivity that can be achieved with laser light as probe is bounded by the standard quantum limit (SQL). As many instruments are approaching this fundamental limit, it becomes crucial to explore ways to overcome the SQL. Quantum metrology offers the possibilities to increase the sensitivities of the most accurate measurements beyond the SQL by using photonic quantum states of light as a tool. Two well-known classes of quantum states that provide a metrological advantage and break the SQL are squeezed states and a certain class of entangled states, called NOON states. While it is of special interest to apply these quantum states to atomic systems, such as atomic vapors, this requires quantum states of the highest quality in terms of purity, fidelity, brightness, and indistinguishability. Most importantly, for the probing of atomic systems, the quantum states need to be extremely narrowband to match the atomic linewidths. As NOON states are usually generated in a broadband spontaneous parametric down-conversion (SPDC) process, they are not compatible with narrowband atomic resonances.

The goal of this thesis was the generation of suitable narrowband entangled and squeezed quantum states of light and their application to atomic systems. To increase the rate of atom-resonant SPDC photons by orders of magnitude, we used a cavity-enhanced setup. Polarization-squeezed states and polarization-entangled NOON states were created. The spectral brightness of the generated NOON states is one of the highest of pairs of indistinguishable photons reported so far. The photon pairs were carefully characterized by full quantum state tomography showing high fidelities with a perfect NOON state. After filtering the photon source output by a novel filter based on the "interaction-free measurement" scheme, a cross-correlation measurement demonstrated its potential as a narrowband heralded single-photon source, needed for example in quantum information. To apply these states in a quantum metrology scheme and to show the metrological advantage, we chose an atomic magnetometer as a model system. The assembled shot-noise-limited magnetometer is based on the Faraday effect in a vapor of hot rubidium atoms. It could be demonstrated that both quantum states perform better in the magnetometer application

than any classical state, i.e., they break the SQL. In the case of NOON states, this is the first use of multi-photon coherence in an atomic experiment. In addition to applications in quantum metrology, the presented techniques of quantum-light generation and filtering are also directly applicable to quantum information tasks, especially to the use in quantum memories.

Resumen

El uso de la luz, en particular la luz láser es, en muchos casos, el método que permite realizar mediciones de la manera más sensible. No obstante, la mayor sensibilidad que se puede conseguir gracias a la luz láser como sistema de sondeo queda delimitada por el límite cuántico estándar (SQL). Visto que muchos instrumentos se están acercando a este límite fundamental, es crucial explorar formas de superar el SQL. La metrología cuántica ofrece la posibilidad de incrementar la sensibilidad de las medidas más precisas más allá del SQL empleando los estados cuánticos de luz como herramienta. Dos categorías conocidas de estados cuánticos que brindan una ventaja metrológica y rompen con el SQL son los estados "comprimidos" y ciertas categorías de estados entrelazados llamados estados "NOON". Aunque es de especial interés aplicar estos estados cuánticos a los sistemas atómicos, como a los vapores atómicos, se requieren estados cuánticos de óptima calidad en términos de pureza, fidelidad, luminosidad e identidad. Lo más importante para los sistemas atómicos de investigación es que los estados cuánticos sean de banda extremadamente estrecha para que coincidan con el ancho de banda de átomos. Puesto que los estados NOON suelen ser generados en un proceso de conversión espontánea paramétrica descendente (SPDC) de banda ancha, no son compatibles con las resonancias atómicas de banda estrecha.

El objeto de esta tesis fue la generación de estados cuánticos de luz apropiados de banda estrecha, entrelazados y comprimidos, y su aplicación en los sistemas atómicos. Para incrementar el número de fotones generados por SPDC resonantes con la transición atómica por órdenes de magnitud, se empleó un sistema aumentado por un resonador. Se crearon estados de polarización comprimida y estados NOON de polarización entrelazada. La luminosidad espectral de los estados NOON generada supone una de las más altas que se hayan reportado hasta el momento entre pares de fotones idénticos. Los pares de fotones fueron cuidadosamente caracterizados por medio de una tomografía completa del estado cuántico que muestra la gran fidelidad con un estado NOON perfecto. Después de filtrar la producción de la fuente de fotones por medio de un novedoso filtro basado en el esquema "interaction-free measurement", una medida de correlación cruzada demostró su potencial como fuente de fotones individuales anunciados de banda estrecha que resulta necesaria, por ejemplo,

en la información cuántica. Para aplicar estos estados en un esquema de metrología cuántica y demostrar la ventaja metrológica, elegimos un magnetómetro atómico como sistema modelo. El montaje del magnetómetro delimitado por el límite cuántico estándar se basa en el efecto Faraday en un vapor de átomos de rubidio calientes. Se podía demostrar que el comportamiento de ambos estados cuánticos es superior en la aplicación con el magnetómetro que cualquier estado clásico, es decir, que superan el SQL. En el caso de los estados NOON, este es el primer uso de la coherencia multifotónica en un experimento atómico. Además de las aplicaciones en la metrología cuántica, las técnicas presentadas de generación de luz cuántica y filtración también son directamente aplicables a las tareas de información cuántica, en especial al uso en las memorias cuánticas.

Exploration is the physical expression of the intellectual passion. And I tell you, if you have the desire for knowledge and the power to give it physical expression, go out and explore. Some will tell you that you are mad, and nearly all will say, 'What is the use?' For we are a nation of shopkeepers, and no shopkeeper will look at research which does not promise him a financial return within a year. And so you will sledge nearly alone, but those with whom you sledge will not be shopkeepers: that is worth a good deal. If you march your winter journeys you will have your reward, so long as all you want is a penguin's egg.

Aspley Cherry-Garrard
The Worst Journey in the World: Antarctic 1910-1913

Contents

The concept of progress acts as a protective mechanism to shield us from the terrors of the future.
-from "Collected Sayings of Muad'Dib"

– Frank Herbert, *Dune*

1

Introduction

The ability to perform precise measurements has had a major influence on the progress of science and technology. For example, the possibility to measure the direction of the earth's magnetic field led to a revolution in sea travel, because it allowed the determination of the course even when the sky was cloudy and celestial navigation was not possible. This new technique therefore contributed to increased sea trade and eventually to the discovery of unknown continents. Later, the position (especially the longitude) could be determined with much higher precision after the invention of the sea clock by John Harrison. Today, the use of GPS increases the precision in positioning down to the scale of meters.

As the measurement techniques were improving increasingly fast over the last century, in some fields, measurements have for the first time become so precise that they are not limited anymore by technical shortcomings, but by more fundamental restrictions of nature itself.

It is possible to increase the precision of an experiment by repeating the measurement many times and taking the average of the outcomes. A simple example of this strategy is counting the number of rain drops that fall on a given area, e.g., a tin roof, per second. If the measurement is performed over a long period of time, the average rate of rain drops N can be determined very accurately, but the error, i.e., the deviation for any particular measurement of one second will be $\sqrt{N}$. Completely analogous

is the behavior of photons in a laser beam. When the number of photons from a laser that hit a detector per second N is measured, the intrinsic error or quantum noise will be $\sqrt{N}$. Photons in a laser beam and rain drops follow the same behavior as they are both governed by the statistics of random independent events: the Poisson distribution.

The $\sqrt{N}$-limit is generally called shot-noise limit and in quantum physics also standard quantum limit (SQL). The relative error that is connected with the SQL is $\delta N \propto \sqrt{N}/N = N^{-1/2}$. This $N^{-1/2}$-noise, is the limiting factor in many precision measurements that use laser light as a probe. When only classical resources (or lasers) are used, an experiment cannot be more accurate than the SQL, but often it is possible to decrease the relative error by using a very large number of photons. In many cases, however, it is not possible to use a high optical power because the system could be destroyed or at least altered. Examples of such systems are single atoms [1, 2, 3], molecules [4, 5], atomic quantum states [6, 7, 8], and biological cells [9]. For these – often very interesting – fragile systems another strategy has to be pursued to increase the precision of measurement.

Fortunately, quantum physics offers a way to overcome the SQL. When instead of a laser beam, quantum states of light are used to probe the system, the relative error can be decreased below the SQL from $N^{-1/2}$ toward N^{-1}, the so-called Heisenberg limit. The most prominent quantum states of light that break the SQL are squeezed states and a certain class of entangled states, called NOON states. While squeezed states are easier to generate and closer to applications, NOON states give a higher metrological advantage per photon and ideally achieve the Heisenberg limit [10]. NOON states are two-mode entangled states that consist of N photons. The metrological advantage of NOON states could be demonstrated experimentally more than a decade ago [11, 12], although for non-fragile systems.

One of the principal goals of this thesis is to demonstrate a quantum metrological advantage in the measurement of a fragile system. The system of choice is a hot ensemble of atoms. This system has special requirements, namely the NOON states have to be narrowband and atom-resonant. The reason why, to date, NOON states were not used to beat the SQL in an atomic system lies in the difficulty to generate NOON states with the right properties, especially the correct bandwidth, to interact with atoms. While the natural linewidth of an atom is of the order of a few MHz, the bandwidth of NOON states is usually many GHz or THz wide. The process that is usually exploited to create NOON states is

spontaneous parametric down-conversion (SPDC), which is a convenient process as it generates pairs of photons. The two photons of a pair are in the same mode and can form a NOON state with N=2, a so-called 2-NOON state [13]. In the past, high efforts were made to increase the size of NOON states and 'NOON-like' states by superposing a 2-NOON state with a coherent beam [14, 15] or by using double-pair emission of an SPDC crystal [16]. The bandwidth in these experiments is usually larger than 100 GHz, i.e., more than four orders of magnitude larger than the natural atomic linewidth. Although the recent experiments that have demonstrated up to 5-NOON states are not suitable for interaction with atoms, these techniques could be adapted to the narrowband regime.

In this thesis an approach is followed that decreases the bandwidth without sacrificing the count rate. When the SPDC process takes place inside an optical cavity that is resonant with the down-converted light, the cavity geometry enhances the spontaneous emission into the cavity modes [17, 18]. For the spatial modes this is convenient because the down-conversion is enhanced into the fundamental Gaussian mode of the cavity and spectrally the modes of the cavity can be designed to match the atomic lindewidths. To select the spectral mode that is atom-resonant, additional filtering of the cavity-enhanced SPDC output is necessary, but the filter requirements are less stringent than for free-space SPDC and a much higher count rate after the filter is achieved. When the SPDC cavity is stabilized onto the frequency of the atomic transition, the generated polarization-entangled NOON states after the filter have all properties to interact efficiently with atoms.

Following a complementary approach, we generate polarization-squeezed states of light in a technically similar manner. Also the production of squeezing is based on an SPDC process inside an optical cavity, which in this regime is known as optical parametric oscillator (OPO).

We demonstrate the potential of both squeezed states and NOON states on a metrological system that relies on light-matter interaction, the atomic magnetometer [19]. In an atomic magnetometer a sample of atoms, placed in an unknown field, experiences energy level shifts due to the Zeeman effect. These level shifts are detected optically in an interferometric scheme, by Faraday rotation. The rotation can be either caused by the normal Faraday effect, i.e., the atomic sample is unpolarized, or – for a larger signal – by the paramagnetic Faraday effect in a polarized sample. At present, the most sensitive instruments for low-frequency magnetic field measurements operate in this way. Notably, they achieve high sensitivities in the

low frequency range (DC-1 kHz), allowing them to detect bio-magnetic fields. [20]. While these magnetometers are reaching higher and higher sensitivities, they are approaching fundamental quantum limits [21, 22].

In our proof-of-principle experiments we use an atomic magnetometer based on the normal Faraday effect as a test system to apply the generated atom-resonant and narrowband quantum states in a metrological context.

While the quantum states of light that are generated are used for quantum metrology, these states are also applicable to other fields of quantum science and technology. It is demonstrated in this thesis that the generated photon pairs that form the NOON state can be used as atom-resonant heralded single photons. These single photons are interesting for quantum information tasks, e.g., quantum memories and quantum computing. Quantum memories are supposed to store information imprinted on a single photon into an atomic system. As the atomic system can be based on an ensemble of atoms in a gas or a solid-state medium, the requirements on the spectral properties of the single photons are very similar to those in quantum metrology. Also the indistinguishability of the generated photons is of great interest for quantum computing, since in schemes for linear optical quantum computing highly indistinguishable photons are required as resource [23].

This thesis is organized in the following way:

Chapter 2 provides the theoretical background for the whole thesis. First, the physics of parametric down-conversion and cavity enhancement are reviewed and important parameters for the characterization of the cavity output are introduced. Then, the theory of quantum state tomography and the theory of NOON states, including the description of their metrological advantage, are presented. The chapter briefly summarizes the theoretical description of quadrature squeezing and polarization squeezing and the application to phase estimation measurements. Finally, normal and paramagnetic Faraday effect are presented as a way to apply a phase shift on a polarized light beam by an atomic system.

Chapter 3 describes the design, construction, and characterization of the cavity-enhanced down-conversion source used in subsequent experiments. The design of the down-conversion apparatus is presented. The source is characterized by measurements of brightness, time-correlations, and photon indistinguishability, and compared to theory. It also describes the characterization of a two-photon NOON state and the experimental reconstruction of the polarization density matrix of the cavity output by

quantum state tomography.

Chapter 4 presents the generation of atom-resonant, ultra-narrowband photon pairs and heralded single photon states. The spectral filtering of the down-converted photons by an atomic based filter is described. The filtered photons are shown to be narrowband and to match atomic resonances in frequency and bandwidth.

Chapter 5 describes the demonstration of a quantum-enhanced measurement of a magnetic field with NOON states. The experimental results are analyzed in terms of Fisher information, which shows that the information content acquired per photon is larger than achievable with the best classical state.

Chapter 6 describes a squeezed-light-enhanced atomic magnetometer. An optical parametric oscillator is shown to produce polarization-squeezed light. The implementation of a quantum noise lock between a squeezed vacuum beam and a local oscillator beam is described. The generated phase-stable, atom-resonant squeezed state is shown to improve the sensitivity of an atomic magnetometer below the standard quantum limit.

Chapter 7 summarizes the main results and discusses possible implications of the work.

Without sensibility no object would be given to us, and without understanding none would be thought. Thoughts without content are empty, intuitions without concepts are blind.

– Immanuel Kant, *Critique of Pure Reason*

2

Theoretical background

lTheory-chapter This chapter summarizes and provides references for the theoretical framework of the experiments presented in the following chapters and develops the specific theory to describe the experiments. The presentations in this chapter include the physics of cavity-enhanced spontaneous parametric down-conversion, quantum state tomography with a focus on polarization tomography of indistinguishable photons and the relationship between tomography and Hong-Ou-Mandel interference, phase estimation including the improvement of classical interferometric schemes with non-classical probe light, the theory of polarization squeezing and Faraday rotation in an atomic ensemble.

2.1 Cavity-enhanced down-conversion

2.1.1 Nonlinear frequency conversion

When a light beam enters into a medium, the medium responds to the electromagnetic field. There are several mechanisms that contribute to the polarization of the medium. At optical frequencies these are mainly the displacement of ions within a crystal lattice and the change in the electronic charge distribution inside the atoms. Macroscopically the de-

pendence of the polarization vector $\mathbf{P}$ on the electric field vector $\mathbf{E}$ can be described as

$$\mathbf{P} = \epsilon_0 \chi \mathbf{E}, \tag{2.1}$$

where ϵ_0 is the electric permittivity of vacuum and χ is the electric susceptibility. When the susceptibility is the same in all spatial directions, the medium is called isotropic. Only then can χ be written as a scalar, otherwise it has tensorial character. The magnitude of the electric susceptibility can itself depend on the electric field:

$$\chi(\mathbf{E}) = \chi^{(1)} + \chi^{(2)}\mathbf{E} + \chi^{(3)}\mathbf{E}\mathbf{E} + ... \tag{2.2}$$

This can be understood in the following way: For low intensities the potential that an electronic charge sees inside an atom can be approximated by a harmonic potential. For high intensities, i.e., for large displacements, this approximation is not valid anymore. Inserting Eq. (2.2) into Eq. (2.1) yields the electric field dependence of the polarization:

$$\mathbf{P}(\mathbf{E}) = \epsilon_0 \chi^{(1)}\mathbf{E} + \epsilon_0 \chi^{(2)}\mathbf{E}\mathbf{E} + \epsilon_0 \chi^{(3)}\mathbf{E}\mathbf{E}\mathbf{E} + ... \tag{2.3}$$

The first term, which is always present, describes the linear optical effects, such as reflection and absorption, whereas higher order terms become important at relatively higher light intensities. The most widely used effects of the $\chi^{(2)}$-nonlinearity are sum-frequency generation and difference-frequency generation with their special cases second-harmonic generation (SHG) and spontaneous parametric down-conversion (SPDC). A second-order nonlinearity is only present in media that do not show inversion symmetry. Usually crystals are chosen as media for applications of second-order effects. These 'nonlinear crystals' can show high second-order nonlinearities and the search for new materials with high nonlinearities is an active field of research.

Since isotropic matter will not show any second-order nonlinear effects, in media like gases, liquids and amorphous solids, the dominant nonlinear effects are coming from the $\chi^{(3)}$-term. This third-order term gives rise to, e.g., the optical Kerr effect, third-harmonic generation (THG) and four-wave mixing (FWM). In general, one of the main applications of nonlinear optical effects is the creation of beams with wavelengths different from the input wavelengths.

For this thesis the most important nonlinear effect and also the most widely used method for the generation of non-classical states of light is

spontaneous parametric down-conversion (SPDC). Inside a suitable crystal a pump photon, typically in the ultra-violet frequency range, is annihilated and two photons, typically in the infrared, are created. These photons – that are called signal and idler – can be correlated in various degrees of freedom. The SPDC process is capable of producing NOON states as well as squeezed states. The following discussion is therefore focusing on SPDC.

In SPDC, energy conservation of the participating photons has to be strictly fulfilled:

$$\hbar\omega_p = \hbar\omega_s + \hbar\omega_i, \tag{2.4}$$

where $\omega_{p,s,i}$ are the angular frequencies of pump, signal and idler beam. When the frequency of the pump beam ω_p is very narrow, energy conservation leads to a strong frequency anti-correlation between the frequencies of the two generated photons.

Momentum conservation, which is also referred to as phase matching, requires

$$\hbar\mathbf{k}_p = \hbar\mathbf{k}_s + \hbar\mathbf{k}_i, \tag{2.5}$$

with $|\mathbf{k}_j| = k_j = 2\pi n_j/\lambda_j$, the vacuum wavelength λ_j and the refractive index of the medium n_j ($j \in p, s, i$) for the wave vectors of pump, signal and idler fields. Depending on the phase-matching conditions, the signal and idler fields can be mutually parallel (type-I) or orthogonally (type-II) polarized.

2.1.2 Phase matching

All nonlinear effects require phase matching of the participating wave vectors. In other words, all the contributions of waves generated at different positions inside the crystal have to add up constructively. Since the index of refraction depends on direction of propagation, wavelength and temperature, there is in general a phase mismatch between the waves. This phase mismatch provokes a flowing-back of energy into the fundamental wave after the coherence length (Fig. 2.1.(a)). In order to avoid this, phase matching has to be guaranteed over the full length of the crystal. In the case of frequency-degenerate SPDC, the phase mismatch Δk along a given direction is

$$\Delta k = k_p - k_s - k_i = \frac{2\pi}{\lambda_s}(2n_p - n_s - n_i), \tag{2.6}$$

where $n_{p,s,i}$ are the refractive indices of pump, signal and idler waves respectively and λ_s is the vacuum wavelength of signal and idler waves.

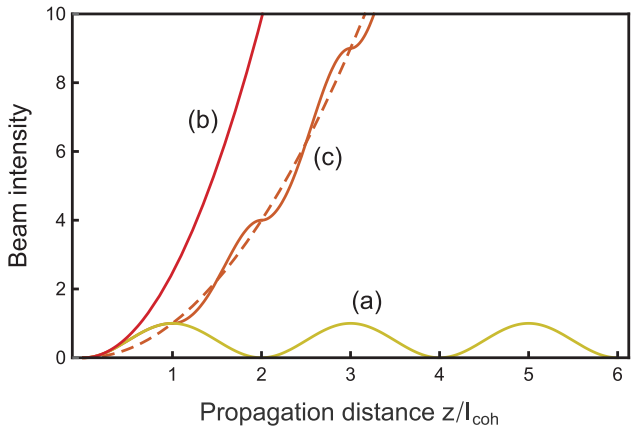

Figure 2.1: Different phase-matching situations. Intensity of the generated SPDC light as a function of the crystal length in units of the coherence length l_{coh}. (a) No phase matching, (b) Birefringent phase matching, (c) Quasi-phase matching.

The coherence length l_{coh} is proportional to the reciprocal phase mismatch:

$$l_{coh} = \frac{\pi}{\Delta k} = \frac{\lambda_s}{2(2n_p - n_s - n_i)} \tag{2.7}$$

In typical nonlinear crystals the differences in refractive index between pump, signal and idler are of the order of a few percent, which leads to a typical coherence length between 5 µm and 50 µm.

Birefringent phase matching

In birefringent crystals the refractive index depends on polarization, angle of propagation, wavelength and temperature. Under certain conditions it is therefore possible to achieve $(2n_p - n_s - n_i) \to 0$ which leads to a long coherence length ($l_{coh} \to \infty$) (Fig. 2.1.(b)). While the phase velocity of the waves is matched, the angle of propagation between ordinary and extraordinary polarized beams differs in general, which gives rise to a spatial walk-off between signal and idler beams. This limits the useful crystal length and leads to an elliptic beam profile of the generated extraordinary beam. To avoid walk-off it is favorable to inject the input beam into the crystal in direction of one of the crystal axes where no walk-off occurs. For some crystals this so-called *non-critical* phase matching can be achieved in such an orientation by temperature tuning.

Quasi-phase matching

Instead of temperature and angle tuning it is possible to avoid the flowing back of energy into the fundamental mode by swapping the sign of the susceptibility after the coherence length. The phase mismatch is then compensated by the so-called *quasi-phase matching* (QPM) (Fig. 2.1.(c)). It is referred to as higher order quasi-phase matching, when the period of the susceptibility is changed after an odd multiple integer of the coherence length. In QPM the direction of propagation is not determined anymore by the phase-matching condition, but can be chosen to coincide with the direction of maximum nonlinearity or one of the crystal axes in order to avoid spatial walk-off between signal and idler waves. Compared to perfect birefringent phase matching the efficiency of m'th order quasi-phase matching is reduced by a factor of $2/m\pi$.

The periodic poling of the crystal is normally achieved by applying large electric fields with alternating signs to a ferroelectric crystal that produce a swap of the ferroelectric domains with alternating polarity. Commonly used crystals are, e.g., lithium niobate ($LiNbO_3$) and potassium titanyl phosphate (KTP). The shorter the poling period is, the more challenging is the fabrication of periodically-poled crystals.

Mathematically, the additional k-parameter is described by a QPM-term:

$$\Delta k(T) = k_p(\omega_p, T) - k_s(\omega_s, T) - k_i(\omega_i, T) - \frac{2\pi}{\Lambda(T)} \tag{2.8}$$

Ideally, the poling period Λ is chosen so that $\Delta k = 0$. The k-parameter of each function however is a function of the frequency and the refractive index which itself is a function of the frequency and the temperature. It is therefore interesting to study the behavior of the function close to the point where the frequencies of signal (ω_s^0) and idler (ω_i^0) guarantee perfect phase matching. Consequently, Δk is expanded in a Taylor series around (ω_s^0, ω_i^0). This derivation is following the approach by Fedrizzi *et al.* [24] to analyze the spectral bandwidth of the down-conversion output and the temperature bandwidth of the phase-matching condition:

$$\begin{aligned}\Delta k(T) = \overbrace{k_p(\omega_p, T) - k_s(\omega_s^0(T), T) - k_i(\omega_i^0(T), T) - \frac{2\pi}{\Lambda(T)}}^{=0} \\ - k_s'(\omega_s^0(T), T)(\omega_s - \omega_s^0(T)) - k_i'(\omega_i^0(T), T)(\omega_i - \omega_i^0(T))\,,\end{aligned} \tag{2.9}$$

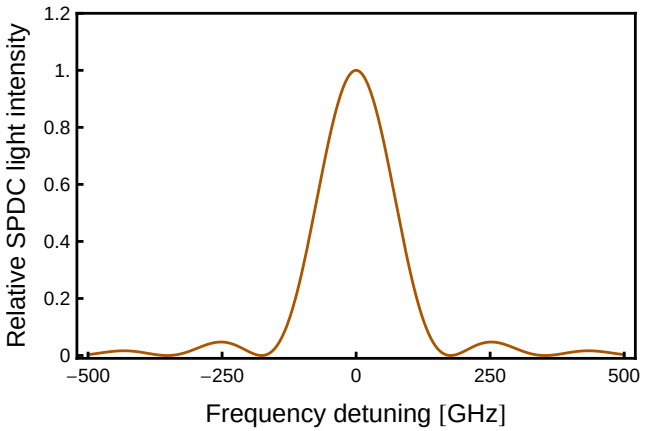

Figure 2.2: Theoretical frequency phase-matching curve. The curve shows the spectral sinc^2-dependence of the SPDC intensity.

with $k'_{s,i} = \frac{dk_{s,i}}{d\omega_{s,i}}\Big|_{\omega_{s,i}=\omega^0_{s,i}}$. From the phase mismatch Δk the intensity distribution of the beam generated in a nonlinear crystal of length l can be calculated (Fig. 2.2):

$$I \propto \mathrm{sinc}^2\left(\frac{\Delta k l}{2}\right) \tag{2.10}$$

The full width at half maximum (FWHM) of the spectral bandwidth of this function can be written as:

$$\Delta\omega = \frac{2\pi}{l\,|k'_s - k'_i|}\,. \tag{2.11}$$

The temperature bandwidth is calculated based on Sellmeier equations for the refractive indices [25, 26]. For a SHG process, in which the two photons of the fundamental wave that are up-converted are of orthogonal polarization, the temperature bandwidth of this SHG interaction is given by the following expression [25, 26]:

$$\Delta T = \frac{0.886\lambda_s}{l}\left|\frac{\partial n_s}{\partial T} + \frac{\partial n_i}{\partial T} - \frac{2\partial n_p}{\partial T}\right|^{-1} \tag{2.12}$$

The reverse process of spontaneous parametric down-conversion, in which the down-converted photons are of orthogonal polarization (type-II), the temperature bandwidth is [25, 26]:

$$\Delta T = \frac{0.886}{L}\left|\frac{1}{\lambda_s}\frac{\partial n_s}{\partial T} + \frac{1}{\lambda_i}\frac{\partial n_i}{\partial T} - \frac{1}{\lambda_p}\frac{2\partial n_p}{\partial T}\right|^{-1} \tag{2.13}$$

For the case of degenerate SPDC this reduces to the same formula as Eq. (2.12), which means the expected temperature bandwidth is the same for these two inverse processes. An analytical treatment that shows that the efficiencies of SHG and SPDC have the same shape is based on Green functions [27].

Boyd-Kleinman theory

Another parameter besides the phase matching to maximize the down-conversion efficiency is the focusing. It is well known that focussing of the pump beam increases the rate of down-converted photons [28]. The optimal focussing in the classical case was studied by Boyd and Kleinman in great detail [29]. For non-critical phase matching the optimal ratio between the crystal length l and the confocal parameter b is $l/b_{opt} \approx 2.84$. The confocal parameter is two times the Rayleigh range, $b = 2z_r = 2\pi n\omega_0^2/\lambda_0$, with the refractive index of the medium n and the vacuum wavelength λ_0. This results in an optimal beam waist of

$$w_{opt} \approx \sqrt{\frac{l\,\lambda_0}{2\pi\,2.84\,n}}\,. \tag{2.14}$$

2.1.3 Cavity enhancement

Even when the efficiency of the SPDC process is optimized in terms of phase matching and mode matching as described before, the produced photon flux at narrow bandwidths (∼MHz) is still low. It can be increased by letting the SPDC process take place inside an optical resonator. This cavity design enhances the generation into the spatial and spectral cavity modes. The temporal and spectral properties of the two-photon wave packets will depend on the cavity geometry. Therefore the cavity parameters have to be chosen carefully to 'tailor' the desired quantum states.

In the following, the parameters of a ring cavity of length L will be introduced. We assume that the cavity consists of three high-reflecting mirrors and an output-coupler of reflectivity R_{OC}. The losses at the high-reflecting mirrors as well as other absorption and scattering losses in the cavity are denoted as P_{loss}.

- **Free spectral range**
  The free spectral range FSR is the spectral distance between two

transmission modes of the cavity and is – for a ring cavity – defined as

$$FSR = \frac{c}{L}. \tag{2.15}$$

- **Cavity round-trip gain**
  The cavity round-trip gain g_{rt} is the factor by which the intensity in the resonator is increased after one round trip. Notably, $g_{rt} < 1$ for a passive cavity. Assuming a Fabry-Pérot cavity it depends on the reflectivity of the outcoupling mirror R_{OC} and the additional loss in the cavity P_{loss}:
  $$g_{rt} = \sqrt{R_{OC}(1 - P_{loss})}\,. \tag{2.16}$$

- **Cavity escape efficiency**
  The cavity escape efficiency P_{esc} is the probability that an intracavity photon is coupled out of the cavity through the output coupler as opposed to being absorbed or scattered in the cavity:
  $$P_{esc} = \frac{1 - R_{OC}}{P_{loss} + 1 - R_{OC}}. \tag{2.17}$$

- **Cavity finesse**
  For g_{rt} near 1 the cavity finesse $\mathcal{F}$ is defined as
  $$\mathcal{F} = \frac{\pi\sqrt{g_{rt}}}{1 - g_{rt}}\,. \tag{2.18}$$

- **Cavity linewidth**
  The cavity linewidth $\Delta\nu$ is the FWHM of individual spectral cavity modes and can be calculated by taking the ratio between the free spectral range and the finesse:
  $$\Delta\nu = \frac{FSR}{\mathcal{F}} \tag{2.19}$$

- **Cavity round-trip time**
  The cavity round-trip time τ_{rt} is defined as the time that a photon needs to make a round trip in the cavity of length L. It is the inverse of the FSR:
  $$\tau_{rt} = \frac{1}{FSR} = \frac{L}{c} \tag{2.20}$$

- **Cavity ring-down time**
  The cavity ring-down time τ_{rd} is defined as the time after which a photon that was coupled into the cavity (or was created in the cavity) persists in the cavity with a probability of $1/e$. It is inversely proportional to the cavity linewidth $\Delta\nu$:

$$\tau_{rd} = \frac{1}{\Delta\nu} \tag{2.21}$$

2.1.4 Time-correlation function

Pioneering work on cavity-enhanced down-conversion, both, experimentally and theoretically was done by Z. Y. Ou *et al.* [17, 18]. They developed a theory for a type-I phase-matched cavity-enhanced SPDC setup by adopting the theory of an optical parametric oscillator (OPO) below threshold developed for the generation of squeezed states by Collett and Gardiner [30]. Later the theory was extended to type-II single-resonant [31] and type-II double-resonant [32, 33, 31, 34, 35] processes. In the following, the theory developed in [31, 34, 35] is summarized and the main result of the cross-correlation function is presented.

SPDC is an important process for quantum optics, because it generates photon pairs. These show more interesting features than coherent light. In order to distinguish between the different statistics of coherent, thermal and non-classical states, the cross-correlation function of the light field can be measured. The normalized intensity cross-correlation function for a single field is defined as

$$g^{(2)}(\tau) \equiv \frac{\langle \hat{E}^\dagger(t+\tau)\hat{E}^\dagger(t)\hat{E}(t)\hat{E}(t+\tau)\rangle}{\langle \hat{E}^\dagger(t)\hat{E}(t)\rangle^2}, \tag{2.22}$$

where $\hat{E}$ is the electric field operator. This cross-correlation function $g^{(2)}(\tau)$ is 1 for a coherent state and all classical fields show $g^{(2)}(\tau = 0) \geqslant 1$, but it can be $0 \leqslant g^{(2)}(\tau) \leqslant \infty$ for a non-classical state. A value of $g^{(2)}(\tau = 0)$ below 1 is therefore a non-classical signature.

For an SPDC process, the cross-correlation function of signal and idler modes is

$$g^{(2)}_{s,i}(\tau) \equiv \frac{\langle \hat{E}^\dagger_s(t+\tau)\hat{E}^\dagger_i(t)\hat{E}_i(t)\hat{E}_s(t+\tau)\rangle}{\langle \hat{E}^\dagger_i(t)\hat{E}_i(t)\rangle\langle \hat{E}^\dagger_s(t+\tau)\hat{E}_s(t+\tau)\rangle}, \tag{2.23}$$

where $\hat{E}_{s,i}$ are the electric field operators of the signal and idler fields.

In order to obtain an explicit expression of the cross-correlation function (Eq. (2.23)), the operators of the electric field have to be evaluated. The positive-frequency electric free-field operators of signal and idler waves propagating in x-direction are

$$\hat{E}^{(+)}_{s,i}(x,t) = \sqrt{\frac{\hbar\omega_{s,i}}{2\epsilon_0 cA}} \int_{-\infty}^{+\infty} \frac{d\Omega}{\sqrt{2\pi}} \hat{a}_{s,i}(\omega_{s,i}+\Omega) e^{i(\omega_{s,i}+\Omega)(x/c-t)}, \tag{2.24}$$

with $[\hat{a}_{s,i}(\omega), \hat{a}^\dagger_{s,i}(\omega')] = \delta(\omega-\omega')$ [36]. In this equation A denotes the transverse cross-section of the wave and $a_{s,i}$ are the photon annihilation operator of the signal and idler modes. Since a type-II process with mutually orthogonal polarizations of signal and idler waves is considered, $[\hat{a}_s(\omega), \hat{a}^\dagger_i(\omega')] = 0$ can be assumed.

The main result and the one that is of most interest for the following experimental implementation is the cross-correlation function for a double-resonant cavity-enhanced SPDC process, which takes the following form:

$$\begin{aligned} g^{(2)}_{s,i}(\tau) \propto \Bigg| & \sum_{m_s,m_i=0}^{\infty} \frac{\sqrt{\gamma_s\,\gamma_i\,\omega_s\,\omega_i}}{\Gamma_s+\Gamma_i} \\ & \times \begin{cases} e^{-2\pi\Gamma_s(\tau-(\tau_0/2))}\mathrm{sinc}(i\pi\tau_0\Gamma_s) & \tau \geqslant \frac{\tau_0}{2} \\ e^{+2\pi\Gamma_i(\tau-(\tau_0/2))}\mathrm{sinc}(i\pi\tau_0\Gamma_i) & \tau < \frac{\tau_0}{2} \end{cases} \Bigg|^2, \end{aligned} \tag{2.25}$$

where $\gamma_{s,i}$ are the cavity damping rates for signal and idler, $\omega_{s,i}$ are the central frequencies, τ_0 is the difference between the transit times of a signal and idler photon through the SPDC crystal, $\Gamma_{s,i} \equiv \gamma_{s,i}/2 + i m_{s,i}\Delta\omega_{s,i}$ with mode indices $m_{s,i}$ and free spectral ranges $\Delta\omega_{s,i}$ [34, 31].

2.1.5 Indistinguishability

Indistinguishability is a key resource in many protocols in quantum information, quantum metrology and quantum communication. The KLM proposal [23], e.g., suggests to use linear optics and indistinguishable photons for quantum computing.

The meaning of 'indistinguishability' in this context does not refer to the bosonic character of photons. Of course, all photons are indistinguishable in that sense. The word 'indistinguishability' is used here in a more operational sense. Photons can be distinct in various degrees of freedom. For example, two photons can be in different spatial, temporal, frequency or polarization modes. For two photons to be distinguishable in this sense,

they need to be distinct in at least two degrees of freedom. One has – in principle – to be able to say, for example: "The horizontally polarized photon always arrives before the vertically polarized one." or "The blue photon is in spatial mode 1, the red photon in mode 2."

If the photons are distinct in only one degree of freedom, they can be indistinguishable. A way to quantify the degree of indistinguishability is the Hong-Ou-Mandel (HOM) experiment. The HOM effect is a purely quantum two-photon interference effect with no classical analog [37, 38]. Two indistinguishable photons that meet on a beam splitter are leaving the beam splitter in the same mode, i.e., ideally no coincident detection events would be measured at the two output ports. Strictly speaking, the photons do not need to meet at a common place. This is because, as Pittman *et al.* [39] have shown, the HOM effect can be understood as the interference of the two-photon amplitude. It is thus not necessary that the photons meet; what is important is that the two-photon amplitudes are indistinguishable, e.g., that no path-information is obtained. When the path of one of the photons is varied with respect to the other, a dip in the coincidence counts is observed at zero time delay between the two paths. The visibility of the HOM interference dip is a measure for the quality of single-photon and pair-photon sources. A limited interference visibility in a polarization HOM experiment is often due to distinguishing information in other degrees of freedom, such as arrival time. Typically, this second distinguishing degree of freedom is something not measured, and only reveals itself through its effect on coherence and interference visibilities.

The following calculation assumes that the two incoming photons are indistinguishable and enter from two different input ports of a beam splitter with reflectivity r. The input modes are labeled 1 and 2 and the output modes 3 and 4 (Fig. 2.3). Analog reasoning applies to the polarization Hong-Ou-Mandel effect, in which the two photons are in the same spatial mode, but in different polarization modes.

We model the beam splitter by the following transformations of the creation operators: $\hat{a}_1^\dagger \rightarrow \sqrt{r}\hat{a}_3^\dagger + \sqrt{1-r}\hat{a}_4^\dagger$ and $\hat{a}_2^\dagger \rightarrow \sqrt{1-r}\hat{a}_3^\dagger - \sqrt{r}\hat{a}_4^\dagger$, where r is the reflectivity of the beam splitter. In the following, the reflectivity of the beam splitter is set to 50% ($r = 1/2$). The creation operator $\hat{a}_j^\dagger$ creates a photon in the j'th mode with $[\hat{a}_k^\dagger, \hat{a}_l^\dagger] = 0$. Within the constraint that the transformation be unitary, there is some freedom in the choice of the relative phases. When each of the input modes of a beam splitter contains one single photon, the output can be described in

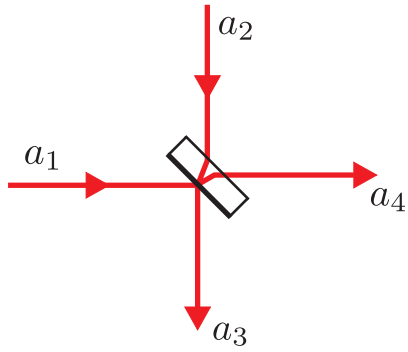

Figure 2.3: Beam splitter modes of Hong-Ou-Mandel effect. Beam splitter with incoming modes 1 and 2 and outgoing modes 3 and 4. Due to the Hong-Ou-Mandel effect, indistinguishable photons impinging from modes 1 and 2 exit the beam splitter on the same output port.

the following way:

$$\begin{aligned}\hat{a}_1^\dagger \hat{a}_2^\dagger \left|vac\right\rangle &\rightarrow \frac{1}{2}(\hat{a}_3^\dagger + \hat{a}_4^\dagger)(\hat{a}_3^\dagger - \hat{a}_4^\dagger)\left|vac\right\rangle \\ &= \frac{1}{2}(\hat{a}_3^\dagger \hat{a}_3^\dagger - \hat{a}_4^\dagger \hat{a}_4^\dagger)\left|vac\right\rangle \\ &= \frac{1}{\sqrt{2}}(\left|2\right\rangle_3 \left|0\right\rangle_4 - \left|0\right\rangle_3 \left|2\right\rangle_4) \end{aligned} \tag{2.26}$$

The probability amplitudes that both photons take different paths after the beam splitter cancel, which results in a "bunching" of the two photons in the same output port.

In contrast, if the two photons are distinct in two degrees of freedom, e.g., if they are in two different spatial modes 1 and 2 and in two different temporal modes, denoted by t_1 and t_2, the HOM effect does not take place:

$$\begin{aligned}\hat{a}_{1,t_1}^\dagger \hat{a}_{2,t_2}^\dagger \left|vac\right\rangle &\rightarrow \frac{1}{2}(\hat{a}_{3,t_1}^\dagger + \hat{a}_{4,t_1}^\dagger)(\hat{a}_{3,t_2}^\dagger - \hat{a}_{4,t_2}^\dagger)\left|vac\right\rangle \\ &= \frac{1}{2}(\hat{a}_{3,t_1}^\dagger \hat{a}_{3,t_2}^\dagger - \hat{a}_{3,t_1}^\dagger \hat{a}_{4,t_2}^\dagger + \hat{a}_{4,t_1}^\dagger \hat{a}_{3,t_2}^\dagger - \hat{a}_{4,t_1}^\dagger \hat{a}_{4,t_2}^\dagger)\left|vac\right\rangle \\ &= \frac{1}{\sqrt{2}}(\left|1\right\rangle_{3,t1} \left|1\right\rangle_{3,t2} \left|0\right\rangle_{4,t1} \left|0\right\rangle_{4,t2} \\ &\quad - \left|1\right\rangle_{3,t1} \left|0\right\rangle_{3,t2} \left|0\right\rangle_{4,t1} \left|1\right\rangle_{4,t2} \\ &\quad + \left|0\right\rangle_{3,t1} \left|1\right\rangle_{3,t2} \left|1\right\rangle_{4,t1} \left|0\right\rangle_{4,t2} \\ &\quad - \left|0\right\rangle_{3,t1} \left|0\right\rangle_{3,t2} \left|1\right\rangle_{4,t1} \left|1\right\rangle_{4,t2}) \end{aligned} \tag{2.27}$$

2.1.6 Heralded single photons

The cavity-enhanced SPDC scheme described in the previous sections is not only able to provide photon pairs, but can also be used as a heralded single-photon source. In this mode of operation, one of the photons of a pair, the idler, is detected and 'heralds' the presence of the other photon, the signal, which state can be a very good approximation of a single-photon Fock state. The lower the contribution of higher photon numbers, the better is this approximation.

E. Bocquillon *et al.* [40] have identified two critical figures of merit for heralded single-photon sources. The first, $g^{(2)}_{S,I}(\tau)$, describes the cross-correlation of signal and idler beams, a measure of reliability of the heralding mechanism. The cross-correlation function was discussed in Section 2.1.4. The second, $g^{(2)}_c(\tau)$, describes the conditional auto-correlation of the signal beam, a measure of the single-photon character of the heralded state. $g^{(2)}_c(0) < 1$ indicates non-classical behavior; $g^{(2)}_c(0) = 0$ for an ideal single-photon source.

The signal auto-correlation function, given a trigger detection of the idler, is [41, 40, 34]

$$g^{(2)}_c(\tau) = \frac{\langle \hat{E}^\dagger_S(t+\tau)\hat{E}^\dagger_S(t)\hat{E}_S(t)\hat{E}_S(t+\tau)\rangle}{\langle \hat{E}^\dagger_S(t)\hat{E}_S(t)\rangle\langle \hat{E}^\dagger_S(t+\tau)\hat{E}_S(t+\tau)\rangle}. \tag{2.28}$$

The crucial figure of merit is the value of the auto-correlation function of signal photons $g^{(2)}_c(\tau)$ at $\tau = 0$. This function is given as [42, 41, 40]

$$g^{(2)}_c(0) = \frac{p_{ab}}{p_a p_b}, \tag{2.29}$$

where p_{ab} is the probability to detect a triggered coincidence of channels a and b and p_a and p_b are the probabilities of triggered single detections of channel a or b, respectively.

2.2 Quantum state tomography

2.2.1 Density matrix formalism

In any physics experiment it is desirable to have as much knowledge as possible about the considered system. In quantum mechanics the complete – accessible – knowledge of a quantum state is contained in the

corresponding density matrix. While it is possible to represent a pure state by a state vector, under laboratory conditions states normally show non-perfect purity and consequently have to be described by the density matrix formalism, which is especially useful to determine the degree of purity and fidelity of a measured mixed state.

If the measured system is in state $|\psi_i\rangle$ with probability p_i, the density matrix of the system is defined as the weighted sum over these states:

$$\hat{\rho} = \sum_i p_i \, |\psi_i\rangle \, \langle\psi_i| \tag{2.30}$$

with non-negative p_i and $\sum_i p_i = 1$. The density matrix has to be hermitian, positive semi-definite and of unit trace. The degree of purity of a state is defined as the trace over the square of the density matrix: $\mathrm{Tr}\{\hat{\rho}^2\}$. The purity ranges between 1 for a perfectly pure state and $1/d$ for a completely mixed state, where d is the dimension of the density matrix.

In this thesis mostly two-photon states are of interest. The density matrix of a general mixed polarization two-photon state takes the following form:

$$\hat{\rho} = \begin{pmatrix} \rho_{11} & |\rho_{12}|e^{i\phi_{12}} & |\rho_{13}|e^{i\phi_{13}} & |\rho_{14}|e^{i\phi_{14}} \\ |\rho_{21}|e^{i\phi_{21}} & \rho_{22} & |\rho_{23}|e^{i\phi_{23}} & |\rho_{24}|e^{i\phi_{24}} \\ |\rho_{31}|e^{i\phi_{31}} & |\rho_{32}|e^{i\phi_{32}} & \rho_{33} & |\rho_{34}|e^{i\phi_{34}} \\ |\rho_{41}|e^{i\phi_{41}} & |\rho_{42}|e^{i\phi_{42}} & |\rho_{43}|e^{i\phi_{43}} & \rho_{44} \end{pmatrix}. \tag{2.31}$$

Because of the hermiticity and the trace condition of the density matrix, this reduces to 15 independent components that are often written in a lower-triangular matrix. An n-photon polarization state is described by a $2^n \times 2^n$ matrix with $4^n - 1$ independent elements.

Projective measurements

The tomographic characterization of the state, described at the end of this chapter, is well described by the formalism of projective measurements. In this formalism, measurement of a quantum system is described by projection operators. A more general approach, the POVM formalism (Positive Operator-Valued Measure) is also widely used in quantum information [43].

Since the density matrix describes the complete state of the quantum system − possibly restricted to a certain degree of freedom such as spin

or polarization − it is possible to calculate the expectation value of any measurement of an observable with hermitian operator $\hat{A}$:

$$\langle \hat{A} \rangle = \sum_i p_i \langle \psi_i | \hat{A} | \psi_i \rangle = \mathrm{Tr}\{\hat{\rho}\hat{A}\}. \tag{2.32}$$

The observable $\hat{A}$ has the following decomposition:

$$\hat{A} = \sum_i a_i \hat{\Pi}_i, \tag{2.33}$$

where $\hat{\Pi}_i$ are the projection operators that project the system onto the eigenspace of $\hat{A}$ with eigenvalue a_i.

2.2.2 General quantum state tomography

The task of quantum state tomography is to deduce the density matrix from the outcomes of a given set of measurements. As measurements in quantum mechanics can leave the system in a different state, two consecutive measurements of non-commuting observables will in general not reflect the state of the initial system. Measurements on a single system are thus insufficient to investigate in which state the system was before the measurement. To acquire this information it is necessary to be able to make measurements on several identical copies of the considered system. The different copies can be projected onto different bases to get full information about the system. This procedure is analogous to other tomographic methods. In medical applications, for example, two-dimensional images of the human body in different bases are made in order to reconstruct the three-dimensional tissue.

In quantum optics different systems and degrees of freedom can be of interest. Quantum state tomography has been performed in various fields of quantum physics, such as trapped ions [44] and super-conducting qubits [45, 46, 47]. The first tomography of a state of entangled photons has been performed by A. G. White *et al.* [48, 49]. Depending on the system of interest, possible degrees of freedom are spin, orbital angular momentum, position or polarization. For applications of photonic quantum states, polarization is often the most useful and therefore most interesting degree of freedom. In this thesis we will discuss exclusively polarization state tomography.

2.2.3 Linear tomographic reconstruction

In this section the formalism of linear tomographic reconstruction is presented. This method was used to analyze our experimental data and to reconstruct the density matrix of the generated quantum states. We follow the seminal work by the group of P. G. Kwiat [48, 49, 50].

Consider the density matrix $\hat{\rho}$ of an unknown state generated in the laboratory. The projection of this unknown polarization state onto a specific polarization basis can be measured experimentally. Polarization analyzers and single-photon detectors allow the measurement of the photon rate in a particular polarization state $|\psi_\mu\rangle$. The normalization of the rate yields the probability that the unknown state is in $|\psi_\mu\rangle$. Mathematically, the projection is described by a projection operator $\hat{\Pi}_\mu = |\psi_\mu\rangle \langle\psi_\mu|$. The probability to find $\hat{\rho}$ in the polarization state $|\psi_\mu\rangle$ is

$$P_\mu = \mathrm{Tr}\{\hat{\rho}\,\hat{\Pi}_\mu\} = \langle\psi_\mu|\,\hat{\rho}\,|\psi_\mu\rangle\,. \tag{2.34}$$

Measurements in different polarization bases are necessary to acquire sufficient information to reconstruct the whole density matrix. The tomographic reconstruction requires $4^n - 1$ $(= d^2 - 1)$ measurements for a partially mixed state, where n is the number of photons and d is the dimension of the Hilbert space ($d = 2^n$ for the two polarization basis vectors). In contrast, a perfectly pure state is determined by $2d - 1$ linearly independent parameters [48]. We restrict the following discussion to the case that the data set consists of outcomes of 4^n linearly independent measurements. It should be noted that, if the number of measurements is larger than 4^n, the over-complete set still permits reconstruction [50, 51].

In analogy to the Stokes parameters of a single-photon polarization state, the polarization density matrix of a multiphoton state can be parameterized as

$$\hat{\rho} = \frac{1}{2^n} \sum_{\nu=1}^{4^n} \hat{\Gamma}_\nu S_\nu \tag{2.35}$$

with the generalized Stokes parameters $S_\nu = \mathrm{Tr}\{\hat{\Gamma}_\nu \hat{\rho}\}$. The $\hat{\Gamma}$-matrices can be constructed as tensor-products of Pauli matrices:

$$\hat{\Gamma}_\nu = \hat{\sigma}_{i_1} \otimes \hat{\sigma}_{i_2} \otimes ... \otimes \hat{\sigma}_{i_n}, \tag{2.36}$$

where $i_j \in \{0, 1, 2, 3\}$ and

$$\hat{\sigma}_0 = \begin{pmatrix} 1 & 0 \\ 0 & 1 \end{pmatrix}, \; \hat{\sigma}_1 = \begin{pmatrix} 0 & 1 \\ 1 & 0 \end{pmatrix} \tag{2.37}$$

$$\hat{\sigma}_2 = \begin{pmatrix} 0 & -i \\ i & 0 \end{pmatrix}, \hat{\sigma}_3 = \begin{pmatrix} 1 & 0 \\ 0 & -1 \end{pmatrix}. \tag{2.38}$$

While the generalized Pauli-matrices represent one possible set of matrices for the parametrization of the density matrix, there are other choices. In general, all sets of matrices that have the following properties can be used [49]:

$$\mathrm{Tr}\{\hat{\Gamma}_\nu \hat{\Gamma}_\mu\} = \delta_{\nu,\mu} \tag{2.39}$$

$$\hat{A} = \sum_\nu \hat{\Gamma}_\nu \mathrm{Tr}\{\hat{\Gamma}_\nu \cdot \hat{A}\} \tag{2.40}$$

for all arbitrary $2^n \times 2^n$ matrices $\hat{A}$. Inserting (2.35) into (2.34) gives

$$\begin{aligned} P_\mu &= \langle\psi_\mu| \frac{1}{2^n} \sum_{\nu=1}^{4^n} \hat{\Gamma}_\nu S_\nu |\psi_\mu\rangle \\ &= \frac{1}{2^n} \sum_{\nu=1}^{4^n} S_\nu \hat{B}_{\nu,\mu} \end{aligned} \tag{2.41}$$

where $\hat{B}_{\nu,\mu}$ is the $4^n \times 4^n$ matrix $\hat{B}_{\nu,\mu} = \langle\psi_\mu| \hat{\Gamma}_\nu |\psi_\mu\rangle$. If $\hat{B}$ is invertible, i.e., if $\hat{B}$ is non-singular, the generalized Stokes parameters can be deduced from the measurement probabilities P_μ:

$$S_\nu = 2^n \sum_{\mu=1}^{4^n} (\hat{B}^{-1})_{\nu,\mu} P_\mu \tag{2.42}$$

For the density matrix this means:

$$\hat{\rho} = \sum_{\mu=1}^{4^n} \sum_{\nu=1}^{4^n} (\hat{B}^{-1})_{\nu,\mu} \hat{\Gamma}_\nu P_\mu = \sum_{\mu=1}^{4^n} \hat{M}_\mu P_\mu \,, \tag{2.43}$$

with $\hat{M}_\mu = \sum_{\nu=1}^{4^n} (\hat{B}^{-1})_{\nu,\mu} \hat{\Gamma}_\nu$.

It is thus possible to reconstruct $\hat{\rho}$ from the coincidence measurements in different bases. Often, this straight-forward approach gives the desired density matrix of the system. Sometimes, however, this method fails to give a physical density matrix. Because of experimental imperfections and fluctuations in the coincidence counts due to the statistical distribution, it is possible that the reconstructed density matrix shows negative eigenvalues and hence fails the criterion of positive semi-definiteness. If this happens, a different approach has to be followed that makes sure that the reconstructed matrix fulfills all requirements on a density matrix.

2.2.4 Maximum-likelihood estimation

This section describes the method that was used in our experimental reconstruction when the linear tomography failed to produce a physical density matrix.

Maximum-likelihood estimation takes into account the physicality of the density matrix by constructing a matrix that is *a priori* hermitian, positive semi-definite and of unit trace. A likelihood function gives the probability that any given state would produce the measured data. Usually the likelihood function is expressed in terms of a set of parameters which define the density matrix. A maximization of this likelihood function results in the density matrix that is most likely to represent the unknown state given the measured data. Following this strategy, it is possible that the discovered maximum is not a global maximum, but a local one. To avoid this, it is useful to perform the tomographic reconstruction through linear inversion as explained in Section 2.2.3. The parameters that are found in this procedure can be used as a set of start parameters for the maximum likelihood estimation.

The positive semi-definiteness and the hermiticity condition (see also Section 2.2.1) are automatically achieved when the matrix $\hat{\rho}$ is of the form: $\hat{\rho} = \hat{T}^\dagger \hat{T}$. To ensure that the matrix has unit trace, the matrix is normalized:

$$\hat{\rho} = \frac{\hat{T}^\dagger \hat{T}}{\mathrm{Tr}\{\hat{T}^\dagger \hat{T}\}}. \tag{2.44}$$

The $\hat{T}$-Matrix of dimension $2^n \times 2^n$ has $4^n - 1$ independent real parameters and can be parameterized in tridiagonal form:

$$\hat{T} = \begin{pmatrix} t_1 & 0 & \cdots & 0 \\ t_{2^n+1} + i t_{2^n+2} & t_2 & \cdots & 0 \\ \vdots & \vdots & \ddots & \vdots \\ t_{4^n-1} + i t_{4^n} & t_{4^n-3} + i t_{4^n-2} & \cdots & t_{2^n} \end{pmatrix}. \tag{2.45}$$

The likelihood function depends on the statistics of the counting events. The coincidence counts follow a Poisson distribution that can be approximated by a Gaussian distribution for large numbers. The conditional probability of obtaining a set of data $\{n_\nu\}=\{n_1, ..., n_{4^n}\}$, given that the system is described by the density matrix $\hat{\rho}$, is

$$P(\{n_\nu\}|\hat{\rho}) = \frac{1}{\mathcal{N}_1} \prod_{\nu=1}^{4^n} \exp\left(-\frac{(n_\nu - \bar{n}_\nu)^2}{2\sigma_\nu^2}\right), \tag{2.46}$$

where $\bar{n}_\nu$ is the number of expected counts in the νth measurement

$$\bar{n}_\nu = \mathcal{N}_2 \langle \psi_\nu | \hat{\rho} | \psi_\nu \rangle , \tag{2.47}$$

with the normalization constants $\mathcal{N}_1$ and $\mathcal{N}_2$. The standard deviation σ_ν of the Gaussian distribution is given by $\sigma_\nu = \sqrt{\bar{n}_\nu}$. With this, the conditional probability becomes

$$P(\{n_\nu\}|\hat{\rho}) = \frac{1}{\mathcal{N}_1} \prod_{\nu=1}^{4^n} \exp\left(-\frac{(n_\nu - \bar{n}_\nu)^2}{2\bar{n}_\nu} \right). \tag{2.48}$$

To simplify this equation and the search for its maximum, the logarithm of the equation is taken:

$$\log P(\{n_\nu\}|\hat{\rho}) - \log \mathcal{N}_1^{-1} = \sum_{\nu=1}^{4^n} \frac{-(n_\nu - \bar{n}_\nu)^2}{2\bar{n}_\nu} = -\mathcal{L} \tag{2.49}$$

The function $\mathcal{L}$ is called likelihood function and has to be *minimized* in order to find a *maximum* for the probability. $\mathcal{L}$ is a function of the 4^n t-parameters and the 4^n measurement outcomes n_ν. Those t-parameters have to be found that are most likely to result in the measured data. In our reconstruction algorithm, the numerical minimization was done using the MATLAB-function *fminsearch* which is an unconstrained nonlinear optimization method based on [52].

2.2.5 Tomography and Hong-Ou-Mandel visibility

As described in Section 2.1.5, the HOM effect gives information about the indistinguishability of two photons in the sense that a high HOM dip visibility implies a high degree of indistinguishability. A low HOM visibility, however, can also stem from a non-perfect preparation of the state or from decoherence. In order to identify the reason for a non-perfect HOM visibility, the information from the HOM experiment is not sufficient. In contrast, quantum state tomography gives full information about the density matrix and can be used to identify the experimental insufficiencies. In this section the connection between HOM visibility and quantum state tomography is investigated.

If two photons are completely distinguishable in the sense explained in Section 2.1.5, they do not perform the HOM effect. This is independent of whether the measurement apparatus is sensitive to the respective degree of

freedom or not. Consider, for example, a measurement on the polarization of photons from a type-II SPDC process. The apparatus is sensitive to polarization, which is thus called an accessible degree of freedom. If one of the photons of a photon pair is delayed with respect to the other one in a way that their temporal overlap is basically zero, the HOM effect will not take place. This is true, even if the temporal resolution of the detection system is not capable of measuring this time difference. Timing information on this time scale would be an inaccessible degree of freedom for the measurement apparatus. Information in inaccessible degrees of freedom can thus influence the measurement outcomes of accessible degrees of freedom.

For the case that the photons can be distinguishable in inaccessible degrees of freedom, a special kind of quantum state tomography was developed by R. B. A. Adamson *et al.* [53, 54, 51]. In the following, this approach is described and connected to the HOM visibility. The description is restricted to the two-photon case that is of relevance in this thesis. The treatment of higher dimensional Hilbert spaces is elaborated on in [54].

The density matrix decomposes into two subspaces: one subspace represents the states that are symmetric under polarization exchange, the other subspace contains the anti-symmetric part. There is no coherence between these subspaces. For the two-photon case, the anti-symmetric subspace consists of just one element and the density matrix takes the following form:

$$\hat{\rho} = \begin{pmatrix} \begin{pmatrix} & \hat{\rho}_S & \end{pmatrix} & \begin{matrix} \cdot \\ \cdot \\ \cdot \end{matrix} \\ \begin{matrix} \cdot & \cdot & \cdot \end{matrix} & \begin{pmatrix} \hat{\rho}_A \end{pmatrix} \end{pmatrix}, \tag{2.50}$$

where $\hat{\rho}_S$ is a 3×3 matrix describing the symmetric portion of the polarization state and $\hat{\rho}_A$ is a 1×1 matrix describing the anti-symmetric portion. We use a dot $(\cdot)$ to indicate coherences between the symmetric and anti-symmetric parts of the state. These coherences, if observed, could allow us to distinguish the photons. But because our analyzer is insensitive to the hidden degrees of freedom where the distinguishing information exists, these coherences are effectively zero.

We use the symmetry-ordered basis $\{|H_1, H_2\rangle, |\psi^+\rangle, |V_1, V_2\rangle, |\psi^-\rangle\}$, with $|\psi^\pm\rangle \equiv (|H_1, V_2\rangle \pm |V_1, H_2\rangle)/\sqrt{2}$, where subscripts $1, 2$ label the photons, as described in reference [53]. In this basis, a general polarization

state is described by a density matrix of the form

$$\hat{\rho} = \begin{pmatrix} \begin{pmatrix} \rho_{HH,HH} & \rho_{HH,\psi^+} & \rho_{HH,VV} \\ \rho_{\psi^+,HH} & \rho_{\psi^+,\psi^+} & \rho_{\psi^+,VV} \\ \rho_{VV,HH} & \rho_{VV,\psi^+} & \rho_{VV,VV} \end{pmatrix} & \begin{matrix} 0 \\ \\ \end{matrix} \\ \begin{matrix} 0 & \\ & \end{matrix} & \begin{pmatrix} \rho_{\psi^-,\psi^-} \end{pmatrix} \end{pmatrix}. \tag{2.51}$$

For simplicity, in the following the subscripts will be labeled with numbers:

$$\hat{\rho} = \begin{pmatrix} \begin{pmatrix} \rho_{11} & \rho_{12} & \rho_{13} \\ \rho_{21} & \rho_{22} & \rho_{23} \\ \rho_{31} & \rho_{32} & \rho_{33} \end{pmatrix} & \begin{matrix} 0 \\ \\ \end{matrix} \\ \begin{matrix} 0 & \\ & \end{matrix} & \begin{pmatrix} \rho_{44} \end{pmatrix} \end{pmatrix} \tag{2.52}$$

We now calculate the coincidence probability for a state $\hat{\rho}$ analyzed in an arbitrary polarization basis. The result allows us to predict the HOM visibility for an arbitrary state, and also the visibility in a polarization interferometer. These visibilities are often reported as indicators of the quality of a state, and our goal here is to make contact between the tomographic results and the simpler but less complete visibilities.

Concretely, we imagine an analyzer consisting of wave plates before a polarizing beam splitter (PBS). One input polarization $|\alpha\rangle \equiv \cos\theta\,|H\rangle - \sin\theta\exp[i\phi]\,|V\rangle$ leaves via one output port of the PBS and the orthogonal polarization $|\beta\rangle \equiv \sin\theta\,|H\rangle + \cos\theta\exp[i\phi]\,|V\rangle$ leaves via the other output port. A coincidence (one photon in each output) indicates a state with one α photon and one β photon, but does not distinguish the photons or indicate the symmetry of the state. It is a projective measurement onto the subspace spanned by $|\alpha_1,\beta_2\rangle$ and $|\alpha_2,\beta_1\rangle$, described by a projection operator $\hat{\Pi}_{\alpha,\beta} \equiv \hat{P}_{|\alpha_1,\beta_2\rangle} + \hat{P}_{|\beta_1,\alpha_2\rangle}$ where $\hat{P}_{|\Psi\rangle} \equiv |\Psi\rangle\langle\Psi|$. The probability of coincidence is $\hat{P}_{coinc} = \mathrm{Tr}\{\hat{\rho}\hat{\Pi}_{\alpha,\beta}\}$. In the symmetry-ordered basis, we find

$$\hat{\Pi}_{\alpha,\beta} = \begin{pmatrix} \frac{1}{2}\sin^2 2\theta & \frac{1}{2\sqrt{2}}e^{-i\phi}\sin 4\theta & -\frac{1}{2}e^{-2i\phi}\sin^2 2\theta & 0 \\ \frac{1}{2\sqrt{2}}e^{i\phi}\sin 4\theta & \cos^2 2\theta & -\frac{1}{2\sqrt{2}}e^{-i\phi}\sin 4\theta & 0 \\ -\frac{1}{2}e^{2i\phi}\sin^2 2\theta & -\frac{1}{2\sqrt{2}}e^{i\phi}\sin 4\theta & \frac{1}{2}\sin^2 2\theta & 0 \\ 0 & 0 & 0 & 1 \end{pmatrix}. \tag{2.53}$$

We now consider the HOM situation encountered in the experiment described in Section 2.1.5. The splitting is balanced, i.e., $\theta = \pi/4$, so that the coincidence probability is

$$P_{coinc} = \rho_{44} + \frac{1}{2}(\rho_{11} + \rho_{33}) - \mathrm{Re}[e^{2i\phi}\rho_{13}]. \tag{2.54}$$

In the experiment, it is possible to introduce a delay between the H and V parts of the state, to achieve zero delay or a large delay. For zero delay, we have $P_{coinc}^{(\text{zero delay})} = \rho_{44} + (\rho_{11} + \rho_{33})/2 - \text{Re}[e^{2i\phi}\rho_{13}]$ as above. A large delay, however, makes H photons distinguishable from V photons and thereby removes the coherence between states $|H_1, V_2\rangle$ and $|V_1, H_2\rangle$. Equivalently, it changes ρ by $\rho_{22} \to (\rho_{22} + \rho_{44})/2$ and $\rho_{44} \to (\rho_{22} + \rho_{44})/2$. Using $\text{Tr}\{\rho\} = 1$, we can express the coincidence probability away from the dip as

$$P_{coinc}^{(\text{delay})} = \frac{1}{2} - \text{Re}[e^{2i\phi}\rho_{13}]. \tag{2.55}$$

The visibility of the HOM dip is

$$V_{HOM} \equiv \frac{P_{coinc}^{(\text{delay})} - P_{coinc}^{(\text{zero delay})}}{P_{coinc}^{(\text{delay})} + P_{coinc}^{(\text{zero delay})}} = \frac{\rho_{22} - \rho_{44}}{2 - (\rho_{22} - \rho_{44}) - 4\text{Re}[e^{2i\phi}\rho_{13}]}. \tag{2.56}$$

We note that this depends on few of the density matrix elements, and thus a variety of different states could have the same HOM dip visibility.

We can also calculate the visibility in an interferometric measurement based on polarization rotations. We assume a wave plate or other optical device applies a unitary rotation to both photons of the state, and they are detected in the α, β state as above. The ψ^- component is invariant under any unitary transformation affecting both photons, and thus contributes a constant ρ_{44} to the coincidence probability. In contrast, the contribution of the triplet component may oscillate between zero and $\rho_{11} + \rho_{22} + \rho_{33} = 1 - \rho_{44}$. A limit on interferometric visibility is thus

$$V_{INT} \leq \frac{1 - \rho_{44}}{1 + \rho_{44}}. \tag{2.57}$$

2.3 Phase estimation

The previous sections presented theoretical background necessary for the characterization of quantum states. In the following, the application of quantum states in a metrological context will be discussed.

When a physical parameter of a system is to be determined, often this parameter is not measured directly. Instead, the parameter is estimated indirectly via a probe. Regardless of the specific implementation the estimation procedure can be described on an abstract level (Fig. 2.4): First, the probe state is prepared. Then the probe is sent to the system, of which some physical parameter should be measured, and interacts with

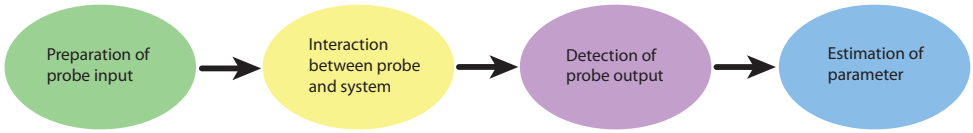

Figure 2.4: Generic parameter-estimation scheme.

it. After that, certain parameters of the output probe are measured and from the acquired information the unknown parameter of the system is estimated. In this scheme, the measurement error is necessarily related to the uncertainty in the measurement of the probe.

The parameter estimation problem is often translated into the measurement of a phase difference. This is desirable, because the measurement of a relative phase between two paths is possible with high sensitivity in an optical interferometer. While classically there is no limit for the sensitivity, quantum physics sets lower limits on the uncertainty in phase, because of the discrete nature of light quanta. The uncertainty in photon number of the optical probe state enters into the phase uncertainty. The aim of quantum estimation theory is to minimize this uncertainty [55, 56, 10].

In this section we analyze the uncertainty scaling in the measured variable in units of the photon number. We derive the fundamental limits for separable states and NOON states. The presented treatment assumes a lossless interferometer in order to derive the fundamental scaling law under optimal conditions. The accounting of losses and the search for the optimal input states under loss situations is an active field of research. For details see [57, 58, 59, 60, 61]. There are different ways in which the theory of phase estimation can be treated. In the following, we present three different approaches. The first is based on the uncertainty principle, the second on operators and the third on Fisher information.

2.3.1 Uncertainty principle approach

An intuitive argument is based on the Heisenberg uncertainty principle, by which the lower limit for the product of phase fluctuation $\delta\phi$ and photon number fluctuation δN is given by:

$$\delta\phi \, \delta N \geqslant 1 \,. \tag{2.58}$$

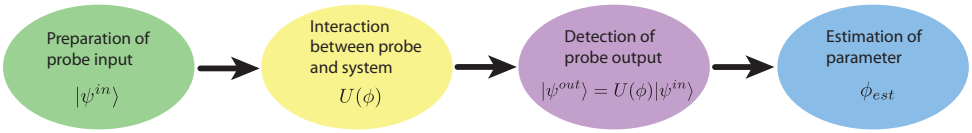

Figure 2.5: Generic phase-estimation scheme.

For coherent light, Poisson statistics of the photon distribution implies an uncertainty in photon number of

$$\delta N = \sqrt{\langle N \rangle}\,, \tag{2.59}$$

which limits the phase precision to the so-called shot noise:

$$\delta\phi \geqslant \frac{1}{\sqrt{\langle N \rangle}}\,. \tag{2.60}$$

However, it can be shown that this shot-noise 'limit' can be broken with non-classical states of light like squeezed and entangled states. In principle, the fluctuations in photon number can be as high as the photon number, leading to the so-called Heisenberg limit:

$$\delta\phi \geqslant \frac{1}{\langle N \rangle}\,. \tag{2.61}$$

The above reasoning is not a rigorous derivation as pointed out in [62] and [63]. The reason is that Eq. (2.58) is derived by operator algebra, while no Hermitian operator for phase exists [62]. For example, Eq. (2.58) does not hold for the vacuum state. A more rigorous treatment will be given below.

2.3.2 Operator approach

Consider the generic parameter estimation scheme of Fig. 2.4. The steps of this approach can be written mathematically in terms of operators (Fig. 2.5): After preparing the input probe state $|\psi^{in}\rangle$, the interaction between probe state and system is represented by a unitary operator $\hat{U}(\phi)$. The output state after the interaction is $|\psi^{out}\rangle = \hat{U}(\phi)\,|\psi^{in}\rangle$. When the interaction takes place in only one of the arms of an optical interferometer, the unitary operator acts only on this mode: $\hat{U}(\phi) = e^{i\phi a_2^\dagger a_2}$.

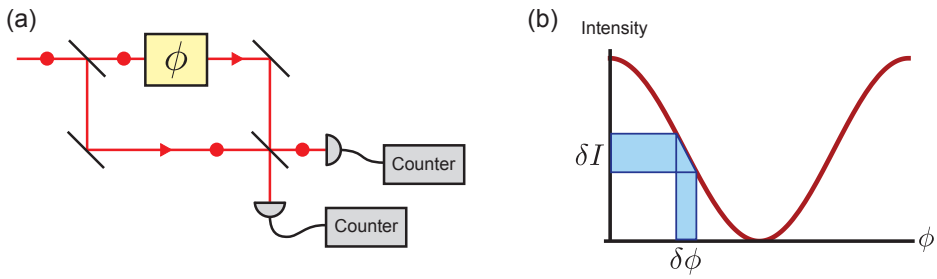

Figure 2.6: Interferometer with product state input. (a) The relative phase between the interferometer arms is modeled by an additional phase shift in one arm. (b) The intensity at each detector shows a sinusoidal dependence on the phase shift. The uncertainty in intensity translates into an uncertainty in phase.

Phase estimation with product states

Consider an entangled single-photon state as input of an optical interferometer (Fig. 2.6):

$$|\psi_{SP}^{in}\rangle = \frac{1}{\sqrt{2}}(|1,0\rangle_{1,2} + |0,1\rangle_{1,2}), \tag{2.62}$$

where the two modes are realized by the different spatial modes. Under these conditions the output state becomes:

$$\begin{aligned} |\psi_{SP}^{out}\rangle_{1,2} &= [\hat{\mathbb{1}} \otimes \hat{U}(\phi)]\, |\psi_{SP}^{in}\rangle_{1,2} \\ &= [\hat{\mathbb{1}} \otimes e^{i\phi a_2^\dagger a_2}] \frac{1}{\sqrt{2}}(|1,0\rangle_{1,2} + |0,1\rangle_{1,2}) \\ &= \frac{1}{\sqrt{2}}(|1,0\rangle_{1,2} + e^{i\phi}\, |0,1\rangle_{1,2}) \end{aligned} \tag{2.63}$$

The expectation value of the operator for a single-photon (SP)

$$\hat{A}_{SP1} = |0,1\rangle\langle 1,0| + |1,0\rangle\langle 0,1| \tag{2.64}$$

is

$$\langle \hat{A}_{SP1} \rangle = \langle \psi | \hat{A}_{SP1} | \psi \rangle = \frac{1}{2}(e^{i\phi} + e^{-i\phi}) = \cos\phi\,. \tag{2.65}$$

In all practical applications, not one but N photons will be sent to get an estimation of the phase. Mathematically the corresponding operator $\hat{A}_N$ can be described by a sum of operators $\hat{A}_{SPi}$ of each single photon, where

each operator acts only on the i'th single photon, that is represented by the state $|\psi\rangle_{SPi}$:

$$\hat{A}_N = (|0,1\rangle\langle 1,0| + |1,0\rangle\langle 0,1|)_{SP1} + ... + (|0,1\rangle\langle 1,0| + |1,0\rangle\langle 0,1|)_{SPN}\,, \tag{2.66}$$

Calculating the expectation value over all N states gives:

$$\begin{aligned}\langle \hat{A}_N \rangle &= \langle\psi|_{SPN} ... \langle\psi|_{SP1} \hat{A}_N |\psi\rangle_{SP1} ... |\psi\rangle_{SPN} \\ &= \langle\psi| \hat{A}_{SP1} |\psi\rangle_{SP1} + ... + \langle\psi| \hat{A}_{SPN} |\psi\rangle_{SPN} \\ &= N\cos\phi \end{aligned} \tag{2.67}$$

Since $\hat{A}^2_{SP1}$ is the identity operator and $\hat{A}^2_N$ is a sum of N identity operators, the expectation value for $\hat{A}^2_{SP1}$ is 1 respectively N for $\hat{A}^2_N$, giving a variance for $\hat{A}_N$ of:

$$(\delta\hat{A}_N)^2 = \langle\hat{A}^2_N\rangle - \langle\hat{A}_N\rangle^2 = N(1-\cos^2\phi) = N\sin^2\phi. \tag{2.68}$$

The variance of the phase can be approximated from this result:

$$\begin{aligned}(\delta\phi)^2 &\approx (\delta\hat{A}_N)^2 \left(\frac{d\langle\hat{A}_N\rangle}{d\phi}\right)^{-2} \\ &= N\sin^2\phi \;\; \frac{1}{N^2\sin^2\phi} \\ &= \frac{1}{N} \\ \implies \delta\phi &\approx \frac{1}{\sqrt{N}} \end{aligned} \tag{2.69}$$

This means that the lower bound for the uncertainty in phase is given by the shot-noise limit.

Phase estimation with NOON states

The uncertainty can be reduced to the Heisenberg limit, when entangled states are used [64, 65, 66, 56].

A NOON state is a highly entangled state that represents the superposition of the state when N photons are in mode 1 and no photon is in mode 2 and vice versa (Fig. 2.7).

$$|N::0\rangle_{1,2} = \frac{1}{\sqrt{2}}\left(|N,0\rangle_{1,2} + |0,N\rangle_{1,2}\right) \tag{2.70}$$

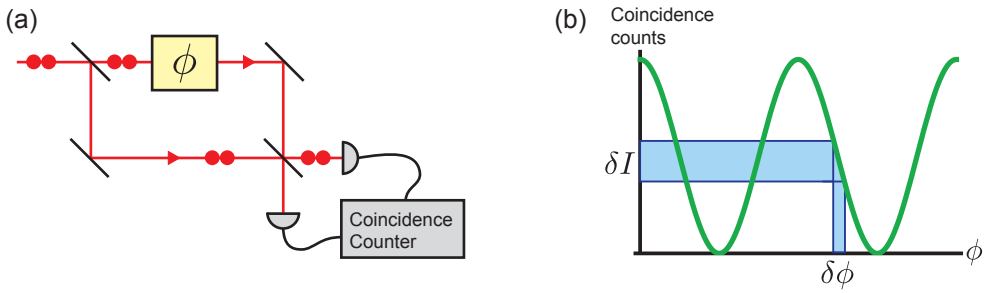

Figure 2.7: Interferometer with NOON state input. (a) The additional phase shift is acquired N times by the N-photon NOON state. (b) The phase dependence of the coincidence counts oscillates faster by a factor of N compared to a product state input. The steeper slope results in a reduced phase uncertainty.

In order to generate a NOON state in the interferometer, the first beam splitter has to be special in the sense that it either transmits or reflects all N photons. In the two-photon case this can be achieved by the Hong-Ou-Mandel effect. The output state of the interferometer is given by:

$$\begin{aligned} |\psi^{out}_{NOON}\rangle_{1,2} &= \left[\hat{\mathbb{1}} \otimes \hat{U}(\phi)\right] |\psi^{in}_{NOON}\rangle_{1,2} \\ &= [\hat{\mathbb{1}} \otimes e^{i\phi a_2^\dagger a_2}] \frac{1}{\sqrt{2}} (|N,0\rangle_{1,2} + |0,N\rangle_{1,2}) \\ &= \frac{1}{\sqrt{2}} (|N,0\rangle_{1,2} + e^{iN\phi} |0,N\rangle_{1,2}). \end{aligned} \tag{2.71}$$

It should be noted that in this case the phase shift in the second term enters with a factor of N. The expectation value for the NOON state of the operator

$$\hat{A}_{NOON} = |0,N\rangle\langle N,0| + |N,0\rangle\langle 0,N| \tag{2.72}$$

is now

$$\langle \hat{A}_{NOON} \rangle = \langle \psi | \hat{A}_{NOON} | \psi \rangle = \frac{1}{2} \left(e^{iN\phi} + e^{-iN\phi} \right) = \cos N\phi. \tag{2.73}$$

The variance of $\hat{A}_{NOON}$ is analog to Eq. (2.68)

$$(\delta \hat{A}_{NOON})^2 = \langle \hat{A}^2_{NOON} \rangle - \langle \hat{A}_{NOON} \rangle^2 = 1 - \cos^2 N\phi = \sin^2 N\phi, \tag{2.74}$$

which gives a phase variance of

$$\begin{aligned}(\delta\phi)^2 &\approx (\delta\hat{A}_{NOON})^2 \left(\frac{d\langle\hat{A}_{NOON}\rangle}{d\phi}\right)^{-2} \\ &= \sin^2 N\phi \ \frac{1}{N^2 \sin^2 N\phi} \\ &= \frac{1}{N^2} \\ \implies \delta\phi &\approx \frac{1}{N}. \end{aligned} \tag{2.75}$$

This shows that the shot-noise limit can be beaten, when NOON states are used as an input resulting in a minimum phase uncertainty given by the Heisenberg limit. This property of NOON states that is called super-resolution has been demonstrated experimentally [12, 67, 14]. In these experiments, the phase shift between two orthogonal polarization modes was imprinted by a wave plate.

NOON state detection

The previous derivation assumed the availability of the operator $\hat{A}_{NOON} = |0,N\rangle\langle N,0| + |N,0\rangle\langle 0,N|$. Experimentally, it is normally not possible to implement such an operator. At the output of the interferometer, the NOON state is recombined on a beam splitter and the phase information has to be deduced from the signal of (number-resolving) single-photon counters at the output ports of the beam splitter. In this section we evaluate the limits in phase estimation under experimental conditions.

A NOON state can be written in terms of creation and annihilation operators for modes 1 and 2:

$$|\psi\rangle = \frac{1}{\sqrt{2}}\left[\frac{1}{\sqrt{N!}}(\hat{a}_1^\dagger)^N + e^{iN\phi}\frac{1}{\sqrt{N!}}(\hat{a}_2^\dagger)^N\right]|0\rangle\,. \tag{2.76}$$

The second analyzing beam splitter transforms the modes in the following way:

$$\hat{a}_1^\dagger = \frac{1}{\sqrt{2}}(\hat{a}_3^\dagger + \hat{a}_4^\dagger) \qquad \hat{a}_2^\dagger = \frac{1}{\sqrt{2}}(\hat{a}_3^\dagger - \hat{a}_4^\dagger)\,. \tag{2.77}$$

For the operators of the NOON state this yields:

$$(\hat{a}_1^\dagger)^N = \sum_{k=0}^{N} \left(\frac{1}{\sqrt{2}}\right)^N c_k (\hat{a}_3^\dagger)^{N-k} (\hat{a}_4^\dagger)^k \tag{2.78}$$

$$(\hat{a}_2^\dagger)^N = \sum_{k'=0}^{N} \left(\frac{1}{\sqrt{2}}\right)^N c_{k'} (\hat{a}_3^\dagger)^{N-k'} (-\hat{a}_4^\dagger)^{k'} , \tag{2.79}$$

where c_k are the binomial coefficients $c_k = \binom{N}{k}$. Inserted into Eq. (2.76) this gives:

$$|\psi\rangle = \left(\frac{1}{\sqrt{2}}\right)^{N+1} \frac{1}{\sqrt{N!}} \Bigg[\sum_{\substack{k=0 \\ k\ even}}^{N} c_k (\hat{a}_3^\dagger)^{N-k} (\hat{a}_4^\dagger)^k (1 + e^{iN\phi}) + \sum_{\substack{k=0 \\ k\ odd}}^{N} c_k (\hat{a}_3^\dagger)^{N-k} (\hat{a}_4^\dagger)^k (1 - e^{iN\phi}) \Bigg] |0\rangle . \tag{2.80}$$

The two different sums for even and odd k in this expression correspond to even and odd photon numbers on the two single-photon counters, if N itself is even. For $N = 2$ these different outcomes can easily be distinguished as the odd state induces coincidences of detection events at the two photon counters, whereas the even state does not. For NOON states with higher photon numbers the difference between even and odd states can be measured with number resolving photon counters or further splitting of the beam after the beam splitter. The respective operators

$$\hat{A}_{even} = |0, N\rangle\langle 0, N| + |2, N-2\rangle\langle 2, N-2| + ... + |N, 0\rangle\langle N, 0| \tag{2.81}$$

$$\hat{A}_{odd} = |1, N-1\rangle\langle 1, N-1| + ... + |N-1, 1\rangle\langle N-1, 1| \tag{2.82}$$

$$\hat{A}_{+} = \hat{A}_{even} + \hat{A}_{odd} \tag{2.83}$$

$$\hat{A}_{-} = \hat{A}_{even} - \hat{A}_{odd} \tag{2.84}$$

have the following expectation values:

$$\langle \hat{A}_{even} \rangle = \frac{1}{4}[(1 + e^{-iN\phi})(1 + e^{iN\phi})] = \frac{1}{2}[1 + \cos N\phi] \tag{2.85}$$

$$\langle \hat{A}_{odd} \rangle = \frac{1}{4}[(1 - e^{-iN\phi})(1 - e^{iN\phi})] = \frac{1}{2}[1 - \cos N\phi] \tag{2.86}$$

$$\langle \hat{A}_{+} \rangle = 1 \tag{2.87}$$

$$\langle \hat{A}_{-} \rangle = \cos N\phi . \tag{2.88}$$

Even and odd number states show different oscillatory behavior when the phase is varied, but both expectation values show a period of $N\phi$ meaning that a smaller phase difference is resolvable compared to a non-entangled state. The variance of the difference operator between even and odd states $\hat{A}_-$ is:

$$(\delta\hat{A}_-)^2 = \langle\hat{A}_-^2\rangle - \langle\hat{A}_-\rangle^2 = 1 - \cos^2 N\phi = \sin^2 N\phi\,. \tag{2.89}$$

Analog to Eq. (2.69) the phase variance becomes

$$(\delta\phi)^2 \approx (\delta\hat{A}_-)^2 \left(\frac{d\langle\hat{A}_-\rangle}{d\phi}\right)^{-2} = \sin^2 N\phi\ \frac{1}{N^2\sin^2 N\phi}\,, \tag{2.90}$$

which results in a phase uncertainty of

$$\delta\phi \approx \frac{1}{N}. \tag{2.91}$$

2.3.3 Fisher information approach

The results of the previous section can also be derived in a different way using the formalism of Fisher information.

Consider the interferometric scheme of the previous sections. The output state of the interferometer is measured by projection measurement. In general, the output state is a mixed state and therefore has to be described by the density matrix $\hat{\rho}$. The probability to detect outcome i given an unknown true value of the phase of ϕ is

$$P(i|\phi) = \mathrm{Tr}\{\hat{\Pi}_i\,\hat{\rho}(\phi)\} \tag{2.92}$$

The maximum information that can be deduced from the measurement outcomes about the unknown phase is called Fisher information (FI) [68, 69, 70]:

$$\mathcal{I}(\phi) = \sum_i P(i|\phi)\left(\frac{\partial \ln P(i|\phi)}{\partial\phi}\right)^2. \tag{2.93}$$

It should be noted that the FI is additive, i.e., the FI provided by several independent measurements sums up to the total FI. The maximum of the FI over all possible measurements is called quantum Fisher information (QFI). For pure states the QFI in an interferometric setup is given by [58, 59, 71]:

$$\mathcal{I} = 4\left[\langle\psi'(\phi)|\psi'(\phi)\rangle - |\langle\psi'(\phi)|\psi(\phi)\rangle|^2\right], \tag{2.94}$$

where $|\psi'(\phi)\rangle$ denotes the derivative $\partial|\psi(\phi)\rangle/\partial\phi$. From Eq. (2.94) the FI of a single-photon state at the output of an interferometer can easily be calculated to be $\mathcal{I} = 1$. Instead, for an N-photon NOON state input the FI becomes $\mathcal{I} = N^2$.

The FI is an important parameter in quantum estimation theory, as it is related to a strict lower bound on the phase uncertainty. This bound is the so-called Cramér-Rao bound [72, 73, 69, 58]:

$$\delta\phi \geqslant \frac{1}{\sqrt{\mu\,\mathcal{I}}}, \tag{2.95}$$

where μ is the number of repetitions of the experiment.

Inserting the values of the FI for a single-photon state and N repetitions gives the same limit in phase estimation as in the previous sections, the shot-noise limit:

$$\delta\phi \geqslant \frac{1}{\sqrt{N}}. \tag{2.96}$$

The Cramér-Rao bound for a NOON state input (without repetitions) leads to the Heisenberg limit:

$$\delta\phi \geqslant \frac{1}{N}. \tag{2.97}$$

2.4 Squeezed states of light

So far, the thesis has discussed non-classical states of light in the single-photon or discrete-variable regime, where the intensity of light is a discrete variable, i.e., photons can be counted. When the light intensity is increased, so that discrete photon events are not resolved anymore, the intensity effectively becomes a continuous variable. Quantum effects, however, can still be observable [74]. In the experiment described in Chapter 6, quadrature-squeezed light is produced and converted into polarization-squeezed light, which is then used to improve the performance of a phase estimation measurement. The following section briefly introduces the concepts of quadrature squeezing and polarization squeezing, before the metrological advantage of squeezed light is discussed.

2.4.1 Quadrature squeezing

One set of continuous variables that describes the quantum state of a system are the so-called quadrature operators of the light field [75]:

$$\hat{X}_1 \equiv \hat{a} + \hat{a}^\dagger \qquad \hat{X}_2 \equiv i(\hat{a}^\dagger - \hat{a}). \tag{2.98}$$

These satisfy the commutation relation $[\hat{X}_1, \hat{X}_2] = 2i$. For the variances of the quadratures, the following uncertainty relation holds

$$\mathrm{var}(\hat{X}_1)\,\mathrm{var}(\hat{X}_2) \geqslant \frac{1}{4}\left|\langle[\hat{X}_1, \hat{X}_2]\rangle\right|^2 = 1, \tag{2.99}$$

where the variance of operator $\hat{A}$ is defined as $\mathrm{var}(\hat{A}) \equiv \langle\hat{A}^2\rangle - \langle\hat{A}\rangle^2$. While the individual variances of the quadratures of a coherent state are equal to 1, quadrature-squeezed states show a lower variance than a coherent state in one quadrature at the expense of a higher variance in the other quadrature:

$$\mathrm{var}(\hat{X}_1)_{|\xi\rangle} < \mathrm{var}(\hat{X}_1)_{|\alpha\rangle} \qquad \text{or} \qquad \mathrm{var}(\hat{X}_2)_{|\xi\rangle} < \mathrm{var}(\hat{X}_2)_{|\alpha\rangle}, \tag{2.100}$$

where the subscript $|\xi\rangle$ denotes a squeezed state and $|\alpha\rangle$ denotes a coherent state.

Mathematically, the squeezed state is constructed by a squeezing operator, defined in the following way:

$$\hat{S}(\xi) = \exp\left[\frac{1}{2}(\xi^*\hat{a}^2 - \xi\hat{a}^{\dagger 2})\right], \tag{2.101}$$

with $\xi = re^{i\theta}$, where $r \geqslant 0$ is the squeezing parameter and $0 \leqslant \theta \leqslant 2\pi$. The squeezing operator creates and annihilates pairs of photons and can therefore be described as a two-photon generalization of the displacement operator [76]. Sometimes squeezed states are therefore referred to as 'two-photon coherent states' [77].

2.4.2 Polarization squeezing

As it has been the case in the discrete-variable regime, we are interested in the polarization degree of freedom. The polarization state of light is described by the Stokes parameters

$$\begin{aligned}
\hat{S}_0 &= \hat{a}_H^\dagger\hat{a}_H + \hat{a}_V^\dagger\hat{a}_V \\
\hat{S}_1 &= \hat{a}_H^\dagger\hat{a}_H - \hat{a}_V^\dagger\hat{a}_V \\
\hat{S}_2 &= \hat{a}_H^\dagger\hat{a}_V + \hat{a}_V^\dagger\hat{a}_H \\
\hat{S}_3 &= i\hat{a}_V^\dagger\hat{a}_H - i\hat{a}_H^\dagger\hat{a}_V,
\end{aligned} \tag{2.102}$$

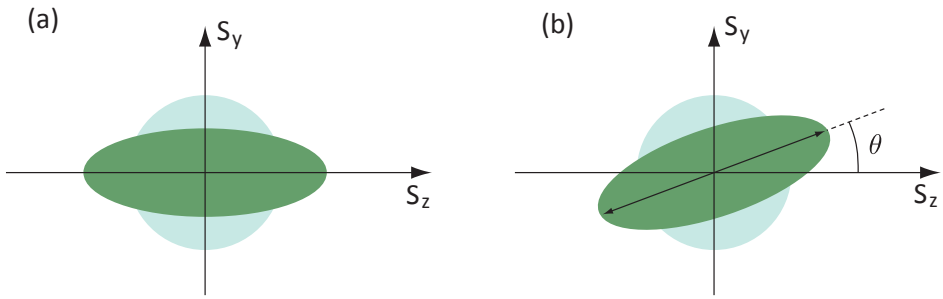

Figure 2.8: Phase-space representation of a polarization-squeezed state. (a) The uncertainty area of a coherent state is represented by a circle (light green), while the uncertainty area of a polarization-squeezed state forms an ellipse (dark green). (b) The angle of the ellipse in phase-space θ is determined by the relative phase between local oscillator and squeezed vacuum.

where the subscripts indicate horizontal (H) and vertical (V) polarization components [78]. Analogously to quadrature squeezing, polarization-squeezed states are those that show a variance smaller than that of a coherent state with the same power for at least one Stokes parameter [74].

There are different ways to produce polarization squeezing. One possibility is to overlap two quadrature squeezed states [74, 79], another to overlap a single quadrature-squeezed beam with a strong coherent beam of orthogonal polarization ('local oscillator') on a polarizing beam splitter [80, 81].

In our experiment, we follow the second approach with a horizontally polarized local oscillator. The combined state shows a strong horizontal polarization, i.e., $\hat{S}_x \approx \hat{S}_0$ with squeezed quantum fluctuations in $\hat{S}_y$ and $\hat{S}_z$. The squeezing behavior of this state can therefore be conveniently visualized by a projection onto the $\hat{S}_y$,$\hat{S}_z$ plane (Fig. 2.8) and so it becomes useful to define the operator $\hat{S}_\phi = \hat{S}_y \cos\phi + \hat{S}_z \sin\phi$, with $\mathrm{var}(\hat{S}_\phi) = \langle N \rangle$. The squeezing criterion for this state becomes

$$\mathrm{var}(\hat{S}_\phi)_{|\xi\rangle} < \mathrm{var}(\hat{S}_\phi)_{|\alpha\rangle} \tag{2.103}$$

for some value of ϕ. While the uncertainty area of a coherent state shows a circle in the phase-space diagram, the uncertainty area of a squeezed state is represented by an ellipse (Fig. 2.8.(a)) [82, 76].

The production of polarization squeezing is a phase-sensitive process. So far, this phase θ was assumed to be fixed at $\theta = 0$. A change of the relative phase between the squeezed vacuum and the local oscillator

corresponds to a rotation of the polarization-squeezing ellipse in the $\hat{S}_y, \hat{S}_z$ plane (Fig. 2.8.(b)) [78].

In the experiment we detect the signal with a balanced polarimeter: The combined signal is rotated by a half-wave plate into the 45 degree basis and split on another polarizing beam splitter. The signals on the two output ports are detected by two photodiodes and then subtracted.

2.4.3 Phase estimation with squeezed states

If squeezed light is used in an interferometric setup, the detection noise can be reduced in the following way.

Consider that one input port of the interferometer a is fed by coherent light $|\alpha\rangle$. If the other input port b is open, i.e., has no input light, phase noise is given by the shot-noise limit. This can be interpreted as phase noise from the open input port, where vacuum fluctuations enter [75]. If instead light that shows less fluctuations than vacuum, i.e., a squeezed vacuum state $|\xi\rangle$ is injected into the open port of the interferometer, the shot-noise limit can be broken.

The input state is a product of the coherent state $|\alpha\rangle$ and the squeezed state $|\xi\rangle$:

$$|\psi_{in}\rangle = |\alpha\rangle_a |\xi\rangle_b = \hat{D}_a(\alpha)\hat{S}_b(\xi)|0\rangle , \tag{2.104}$$

where $\hat{D}_a(\alpha)$ is the displacement operator and $\hat{S}_b(\xi)$ the squeeze operator, acting both on the vacuum state. The state evaluation of this input state in the interferometer can be described by three transformations: The two beam splitter transformations and the additional phase shift in one of the interferometer arms. When these transformations are described in the framework of the SU(2) rotation group as in [83, 76], it can be shown that under the conditions $\theta = \pi/2$ and $N \gg \sinh^2 r$, where N is the number of photons, the phase uncertainty becomes [84, 76]

$$\delta\phi = \frac{e^{-r}}{\sqrt{N}}. \tag{2.105}$$

Since $r \geqslant 0$, a phase uncertainty below the shot-noise level is achieved.

2.5 Faraday effect

As described in the previous sections, quantum light can increase the sensitivity in a phase measurement. The goal of this thesis is to let this

phase shift be imprinted onto the photonic state by an atomic medium. This would allow for measuring an atomic property with better than shot-noise-limited sensitivity. One way to achieve a phase shift from an atomic system is by Faraday rotation [85]. The Faraday effect is a linear magneto-optical effect by which the polarization plane of a linearly polarized probe beam is rotated in a medium that shows optical anisotropy [86, 87].

In the following, the effect of the atomic medium on the optical states is described. This description will be from the perspective of optical interferometry, in which the atomic medium is described by the real and imaginary parts of the refractive index, which will be different for the two circular polarizations. The way in which the atoms produce this refractive index is a subject in itself: A full description of the atomic physics involved in these experiments is quite complex. The various situations encountered in this thesis involve Doppler broadening, atomic transit through probing and pumping beams, optical pumping, linear and nonlinear Zeeman shifts, and radiation trapping. Here only a schematic description is presented and the reader is referred to [88, 8, 89] for details.

The Faraday effect can be understood as a polarization interferometer: The linear input polarization decomposes in left- and right-circular polarization. Due to the anisotropy, the two circular polarizations experience different absorptive and dispersive features of the medium. The acquired phase between the two circular polarizations leads to a rotated linear polarization after the medium, while the differential absorption results in elliptical or circular polarization. In this thesis, a vapor of alkali atoms serves as anisotropic medium. If no magnetic field is applied and the atomic medium is isotropic and in a thermal state, the medium interacts symmetrically with left- and right-circularly polarized light, hence no polarization rotation takes place (Fig. 2.9.(a)). The anisotropy can be induced by an external magnetic field (normal Faraday effect, Fig. 2.9.(b)) or by a population imbalance of Zeeman sublevels (paramagnetic Faraday effect, Fig. 2.9.(c)).

When a magnetic field is applied to the atomic medium in the direction of the propagation of the probe beam, the sublevels shift due to the Zeeman effect, which results in different resonance frequencies for right- and left-circularly polarized light (Fig. 2.9.(b)). For a given frequency of the probe light, this leads to differential absorption (circular dichroism) as well as to differential dispersion (circular birefringence).

Another way to break the symmetry of the interaction of right- and left-circularly polarized light is spin-polarization of the atomic ensemble.

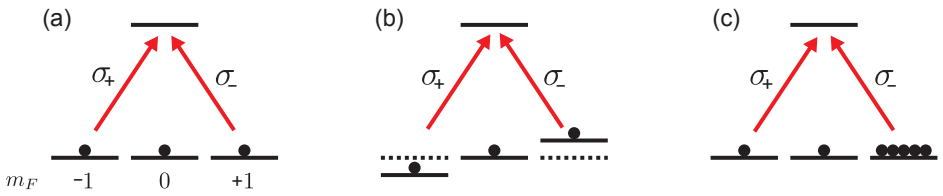

Figure 2.9: Atomic energy level structure of the Faraday effect. Right- (σ_-) and left-circularly (σ_+) polarized light is absorbed by the atomic ensemble. (a) No Faraday effect. Without applied magnetic field and population imbalance the two circular polarizations are absorbed symmetrically. (b) Normal Faraday effect. Due to an external magnetic field the Zeeman sublevels shift. (c) Paramagnetic Faraday effect. The isotropy of the medium is broken by a population imbalance of Zeeman sublevels.

A population imbalance in the Zeeman sublevels results in a stronger absorption of one circular polarization and in a different real part of the refractive index (Fig. 2.9.(c)). The spin-polarization can be induced by optically pumping the atoms with a circularly polarized pump beam [90].

We follow the theory of [91, 92, 93, 88] to provide an expression for the electric field and intensity of a light beam after a Faraday interaction with an atomic medium. We consider a linearly polarized, monochromatic, weak-intensity probe beam propagating in z-direction through an atomic vapor. A magnetic field B_z is applied along the propagation direction. The electric field of the incident beam can be written as:

$$\mathbf{E}(0,t) = E_0 \mathbf{e}_\epsilon \cos\omega t, \tag{2.106}$$

where the electric field vector $\mathbf{E}$ oscillates in the x,y plane: $\mathbf{e}_\epsilon = \mathbf{e}_x \cos\epsilon - \mathbf{e}_y \sin\epsilon$. Inside the anisotropic atomic medium of length L, the propagation of the two orthogonal circular polarization components is governed by different wave numbers $k_\pm$

$$\mathbf{E}(z,t) = \frac{E_0}{2}\left(A_+ \mathbf{e}_+ e^{-i(\omega t - k_+ z)} + A_- \mathbf{e}_- e^{-i(\omega t - k_- z)} + c.c.\right), \tag{2.107}$$

where $k_\pm = \frac{\omega}{c}(n_\pm + i\alpha_\pm)$, $\alpha_\pm$ are the absorption coefficients and $n_\pm$ the refractive indices in the medium for $\sigma_\pm$ polarized light, $A_\pm = A_\pm^r + iA_\pm^i$ and $\mathbf{e}_\pm = \mp\frac{1}{\sqrt{2}}(\mathbf{e}_x \pm i\mathbf{e}_y)$.

To measure the change of the polarization described in Eq. 2.107, often, a polarizer is used in the detection. Certainly, the intensity measured

after the polarizer depends on the relative angle between the polarization direction of the light after interaction with the atomic medium ϵ and the polarizer angle θ

$$I_\theta = (\mathbf{E}(L,t)\cdot\mathbf{e}_\theta)^2, \tag{2.108}$$

where $\mathbf{e}_\theta = \mathbf{e}_x\cos\theta - \mathbf{e}_y\sin\theta$. Evaluating Eq. (2.108), the intensity that is transmitted by the polarizer is then given by [92]

$$\begin{aligned} I_\theta = &\frac{I_0}{4}\left(e^{-2\alpha_+\omega L/c} + e^{-2\alpha_-\omega L/c}\right) \\ &+\frac{I_0}{2}\cos\left[2(\epsilon-\theta) + (n_+ - n_-)\frac{\omega L}{c}\right] e^{-(\alpha_+ + \alpha_-)\omega L/c}. \end{aligned} \tag{2.109}$$

where I_0 is the incident intensity, ω is the angular frequency of the probe light. Using the identities $\cos 2x = 1 - 2\sin^2 x$ and $\cos x = -\cos(x-\pi)$, Eq. (2.109) can be transformed to

$$\begin{aligned} I_\theta = &\frac{I_0}{4}\left(e^{-\alpha_+\omega L/c} - e^{-\alpha_-\omega L/c}\right)^2 \\ &+I_0\,\sin^2\left[(\epsilon-\theta-\frac{\pi}{2}) + (n_+ - n_-)\frac{\omega L}{2c}\right] e^{-(\alpha_+ + \alpha_-)\omega L/c}. \end{aligned} \tag{2.110}$$

The first term describes the differential absorption due to circular dichroism, this is sometimes also called 'parity nonconservation rotation' [92]. The second term leads to Faraday rotation with an overall absorption factor. In the case that the Faraday rotation takes place between crossed polarizers ($\epsilon - \theta = \pi/2$), the transmitted intensity is at a minimum and Eq. (2.110) reduces to the corresponding equation given in [88].

In this thesis, the Faraday effect of two extreme cases of this equation is exploited, for a narrowband atomic-based filter and for the magnetometer application.

2.5.1 Atomic magnetometer based on Faraday effect

For the magnetometer application described in Chapters 5 and 6, it is desirable that the measured signal depends directly on the magnetic field strength. Since both input probe states – NOON states and squeezed states – are sensitive to losses, the absorption in the atomic medium should be kept to a minimum. For these reasons we rely for the magnetometer application on the normal Faraday effect far-off-resonance. At a large

detuning, the differential absorption is negligible and Eq. (2.110) reduces to

$$I_\theta = I_0 \sin^2 \left[(\epsilon - \theta - \frac{\pi}{2}) + (n_+ - n_-)\frac{\omega L}{2c} \right] e^{-(\alpha_+ + \alpha_-)\omega L/c} \ . \quad (2.111)$$

The Faraday rotation angle ϕ is thus given by

$$\phi = (n_+ - n_-)\frac{\omega L}{2c}. \quad (2.112)$$

To measure the Faraday rotation angle, a convenient way is to use a balanced polarimeter setup consisting of a polarizing beam splitter at 45° from the linear input polarization and two photodetectors. The difference signal of the two detectors is zero if no polarization rotation takes place. Any rotation signal can therefore be detected on a zero background. Another advantage of this setup is its insensitivity to circular dichroism. For these reasons, we use this detection scheme in the squeezed light magnetometer presented in Chapter 6. Chapter 5 describes the NOON state probing of an atomic magnetometer. Since the NOON state is composed of two orthogonal polarizations and at the single photon level, not the difference signal is taken, but the coincidence counts between the two output ports of a polarization analyzer are recorded.

2.5.2 Narrowband filter based on Faraday effect

As explained in detail in Chapter 4, the ultra-narrowband filter developed in our group is based on a polarization interferometric scheme, in which the two interferometer modes correspond to the two circular polarizations. One circular polarization needs to be completely absorbed in the interferometer, the other polarization mode should be transmitted. For this reason we work in the regime of the paramagnetic Faraday effect on resonance. In this regime, the circular birefringence is negligible and only the differential absorption of the circular polarizations contributes to the output signal. Under these conditions Eq. (2.110) reduces to

$$I_\theta = \frac{I_0}{4} \left(e^{-\alpha_+ \omega L/c} - e^{-\alpha_- \omega L/c} \right)^2 . \quad (2.113)$$

In the extreme case that one circular polarization is completely absorbed and the other one completely transmitted, the intensity of the transmitted

light takes its maximum of 1/4 of the incident intensity. The atomic-based filter therefore shows a maximum efficiency of 25%.

Light that is close to, but not exactly on resonance will experience a polarization rotation and can be transmitted. This contributes to the linewidth of the filter. In our case, this effect is negligible as the linewidth of the central frequency mode of the incident beam is much narrower than the linewidth of the filter.

Part I

Discrete-variable regime

'Many things I can command the mirror to reveal,' she answered, 'and to some I can show what they desire to see. But the mirror will also show things unbidden, and those are often stranger and more profitable than things which we wish to behold. What you will see, if you leave the mirror free to work, I cannot tell. For it shows things that were, and things that are, and things that yet may be. But which it is that he sees, even the wisest cannot always tell. Do you wish to look?'

– J.R.R. Tolkien, *The Fellowship of the Ring*

3

Cavity-enhanced down-conversion

Our goals in atomic quantum metrology require quantum states of light with certain characteristics, such as high brightness, very narrow bandwidths and high indistinguishability. Spontaneous parametric down-conversion is a convenient way to generate quantum states, but suffers from relatively low brightness, gives little control of bandwidth and does not necessarily provide highly indistinguishable photons. Adding a cavity narrows the bandwidth and also provides resonant enhancement. This chapter describes the design, construction and characterization of the cavity-enhanced down-conversion source used in the thesis.

3.1 Introduction

Spontaneous parametric down-conversion (SPDC) is the standard method in quantum optics to produce single photons, photon pairs and squeezed light. Compared to other sources of quantum light, it is a relatively simple method, the emission shows a narrow bandwidth and its direction is determined by momentum conservation. Depending on the application, the emission can be tailored to be very broadband [94] or very narrowband [28]. While in the latter case the bandwidth is narrow in comparison with most other single-photon sources, it still extends over at least tens of GHz

leaving a big mismatch to the natural atomic linewidths of a few MHz. In order to reduce the bandwidth of the emission to the bandwidth of an atomic transition, the SPDC photons have to be filtered in frequency. A filtering with subsequent cavities is possible [95], but decreases the photon flux by orders of magnitude rendering many experiments with the filtered photons unpractical or impossible. As opposed to the filtering scheme after the generation process, the photons can be tailored in frequency during generation if the SPDC process takes place inside an optical cavity. This field of cavity-enhanced SPDC was started by work of Z. Y. Ou *et al.* [17, 18, 96] and continued with increasing interest in the last few years [97, 98, 33, 99, 100, 101, 102, 34]. The cavity geometry enhances the creation of photon pairs into the spatial and spectral modes of the cavity. All the spectral cavity modes that lie within the phase-matching bandwidth of the SPDC process are populated. The cavity can be designed to achieve atom-resonance of the frequency-degenerate mode. While subsequent filtering is necessary to block the non-degenerate modes and achieve single-mode emission, the filter requirements for cavity-enhanced SPDC are less stringent than for free-space SPDC and a much higher photon rate can be achieved [103, 102, 34, 104, 105].

The following sections describe the design of the SPDC cavity, including the choice of the nonlinear crystal, the experimental setup, and characterization measurements, such as Hong-Ou-Mandel interference and quantum state tomography.

3.2 Photon-source design

3.2.1 Nonlinear crystal

For our experiment, we have the following requirements on the nonlinear crystal: The crystal has to be type-II phase-matched for down-conversion from 397.5 nm to 795 nm, the frequency of the D_1 transition of rubidium. It should show a large nonlinearity for that process and exhibit no spatial walk-off between signal and idler beams. The phase-matching temperature should be above room-temperature to avoid water condensation on the endfaces.

The crystal that provides the best performance with respect to these requirements is a periodically-poled potassium titanyl phosphate (PPKTP) crystal with a poling period for the type-II process of 9.4 µm. At the time

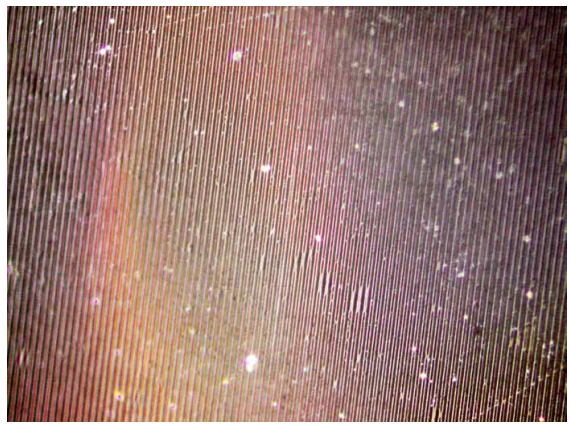

Figure 3.1: Microscopy picture of a type-II PPKTP crystal. The surface has been edged with HF to achieve a contrast in the height of the domains.

when we purchased the crystal, the longest available length was 20 mm and the biggest aperture 1 mm by 2 mm. The long crystal length guarantees a tight phase-matching condition and therefore a narrow bandwidth. The FWHM of the crystal phase-matching bandwidth is calculated to be $1/(|k'_s - k'_i|l) = 148$ GHz, as described in Section 2.1.2. This bandwidth is narrow in the SPDC context, but still orders of magnitude larger than the atomic linewidth of rubidium. The phase-matching temperature is slightly above room temperature. The domain structure of a type-II PPKTP crystal is shown in Fig. 3.1. This microscopy image was taken by coworkers in the group of V. Pruneri at our institute. To study the domain structure of the crystal, its surface was etched with hydrogen fluoride (HF). For differences in the polarity, only domains with the poling in one of the two directions are attacked by the HF, which leads to a contrast in the height of the domains that can be observed under a microscope.

3.2.2 Experimental setup

The exact frequency of the pump beam is achieved by starting with an external cavity diode laser, which is locked to the D_1 transition of rubidium. The locking is done by saturated absorption spectroscopy with the error signal being generated by FM spectroscopy [106, 107, 108]. For this scheme the laser current is modulated at a frequency of 20 MHz. A small part of the laser intensity is sent through a rubidium vapor cell in a double-pass configuration and detected by a photodiode. When the

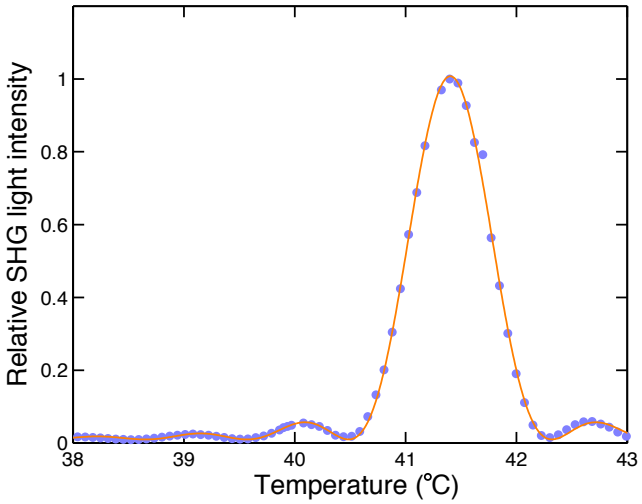

Figure 3.2: Experimental temperature phase-matching curve. The data points show good agreement with the sinc^2-fit function.

frequency of the laser is scanned over the D_1 transition of rubidium, the transmission signal shows the Doppler-broadened absorption lines of this transition. For a certain velocity-class that consists of those atoms that are in rest, the absorption is saturated because of the double-pass configuration, which leads to a spectrally narrow transmission feature. The detected signal is amplified and then mixed with a local oscillator signal at 20 MHz to extract the DC component. This DC component is pre-amplified and sent into a field programmable gate array (FPGA) board that serves as a Labview-controlled PID servo loop. The analog output of the FPGA is the error signal that is fed back to the laser current.

The frequency-locked laser is then amplified by a tapered amplifier (TA) and frequency doubled in a second-harmonic generation (SHG) cavity. Laser, TA unit and SHG cavity are contained in a single box that was bought as a commercial system (Toptica, TA-SHG 110). In the SHG cavity that is also stabilized by FM spectroscopy, a 10 mm long lithium triborate (LBO) crystal works as nonlinear crystal. The frequency-doubled beam is passed through a single-mode fiber for mode cleaning and then mode-matched onto a PPKTP, in which the SPDC process takes place.

In order to determine the crystal's phase-matching temperature, the intensity of the frequency-doubled beam was measured versus the crystal temperature (Fig. 3.2). A diagonally polarized laser beam at 795 nm was injected into the crystal and the power of the SHG signal was measured

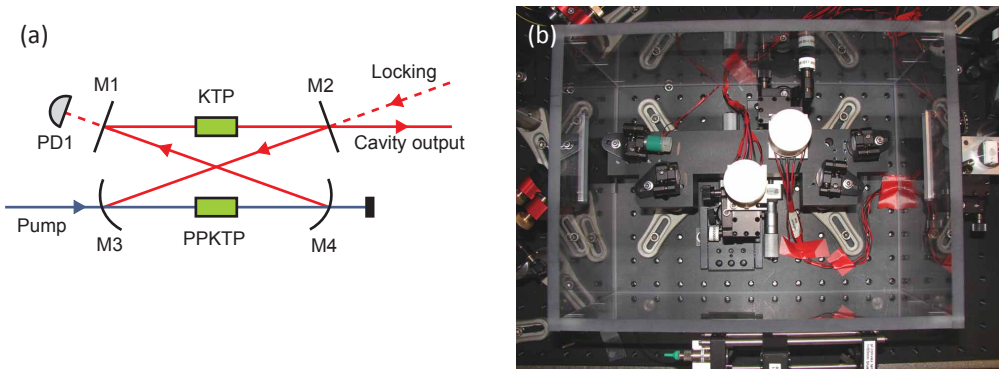

Figure 3.3: Cavity-enhanced SPDC setup. (a) Conceptual scheme. PPKTP, phase-matched nonlinear crystal; KTP, compensating crystal; M1-4, cavity mirrors; PD, photodiode. (b) Photo of the cavity.

with a photodiode. The focussing parameters of the 795 nm beam were chosen to be equal to the expected characteristics of the generated beams in a SPDC process. Fig. 3.2 shows that the data points are in good agreement with a sinc^2-fit function. The fit function has its maximum at 41.4° and a zero-to-zero base bandwidth of 1.8 K. This is close to the estimated 1.4 K calculated from Eq. (2.12) using the $\partial n/\partial T$-parameters from [109]. As SHG and SPDC are supposed to show the same bandwidth, the temperature bandwidth was measured by SHG, which is easier to detect than the signal from SPDC.

3.2.3 Cavity design

Although the PPKTP crystal shows a relatively narrow bandwidth of 148 GHz, this is still orders of magnitude broader than the typical natural atomic linewidth. It is possible to narrow the linewidth without sacrificing the photon rate by letting the SPDC process take place inside an optical cavity. This enhances the emission into the spectrally narrow and spatially single mode of the resonator. The overall enhancement in photon rate is linear in the cavity finesse [32].

Our cavity is a ring cavity built in bow-tie design (Figs. 3.3.(a) and 3.3.(b)). This decreases the losses in the crystal per roundtrip compared to a linear cavity design and allows for a more flexible use of the input ports. The cavity is formed by two flat mirrors (M1, M2) and two concave mirrors (M3, M4) with a curvature radius of 100 mm at a distance of 119 mm. The cavity geometry was chosen to provide the desired beam

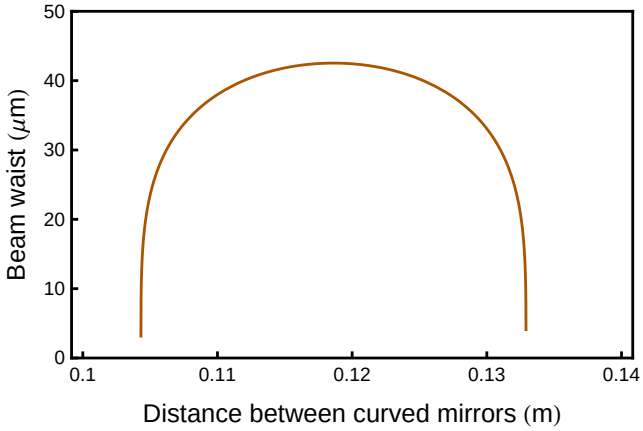

Figure 3.4: Intra-cavity beam waist size. Dependence of the cavity beam waist on the distance between the curved cavity mirrors. The waist is relatively constant over a distance of about 1 cm.

waist at the center of the PPKTP crystal. The optimum waist size for the down-conversion process as calculated from the Boyd-Kleinman theory (Eq. (2.14)) is $w_{opt} = 22.5\,\mu\text{m}$. For a small beam waist, effects such as gray-tracking and thermal lensing can become important. These effects were studied theoretically and experimentally in our group [110]. It turned out that at a beam waist size of 42 µm thermal lensing is negligible. The waist size was therefore chosen to be 42 µm, which is provided by a distance between the curved mirrors of 119 mm. The waist size is relatively constant over a range of several millimeters around this central distance of the curved mirrors (Fig. 3.4).

Due to birefringence in the crystal, the two polarization modes experience different group velocities causing a delay between signal and idler. This effect, which is present in all type-II setups, leads to a temporal distinguishability of signal and idler photons. To compensate for the temporal delay per round trip, a KTP crystal of the same length as the PPKTP, rotated by 90° with respect to the PPKTP around the beam axis, is added to the long arm of the cavity (Fig. 3.5). The initial temporal distinguishability in the creation process is compensated after the cavity. The ring cavity design avoids problems with pairs generated in the counterpropagating mode, which would not be compensated correctly.

The output coupler (M2) has a reflectivity of $R_{OC} = 93\%$ at 795 nm, while the other cavity mirrors are highly reflective ($\text{R}_{HR,795} > 99.9\%$) at 795 nm and highly transmissive at 397.5 nm ($\text{R}_{HR,397.5} < 3\%$) resulting in

a single-pass through the nonlinear crystal for the blue pump beam. The curved mirrors are anti-reflection (AR) coated for 397.5 nm; the crystal endfaces also for 795 nm.

According to Eq. (2.16) the gain per round trip g_{rt} for 795 nm is

$$g_{rt} = \sqrt{R_{OC} R_{HR}^3 T_{crys}^4}, \tag{3.1}$$

where R_{OC} is the reflectivity of the output coupler, R_{HR} is the reflectivity of the other three high reflecting mirrors and T_{crys} is the transmission efficiency through one crystal surface for both, PPKTP and the compensating KTP crystal. The crystal endfaces were anti-reflection (AR) coated by the manufacturer (Raicol Crystals Ltd.). The specified residual reflectivity is <0.5% per surface. According to Eq. (2.18) These values put a lower limit of 66 on the expected finesse.

The probability that a generated photon is lost within one cavity roundtrip due to absorption or scattering is $P_{loss} = 1 - R_{HR}^3 T_{crys}^4 = 0.015$, which leads to an escape efficiency of $P_{esc} = 82\%$ (Eq. (2.17)).

The effective cavity length was measured to be 610 mm which corresponds to a free spectral range (FSR) of 490 MHz. In order to determine the finesse, an auxiliary beam was injected into the cavity and detected at the output while the cavity length was scanned. The finesse is given by the ratio between the FSR, i.e., the distance between two fundamental transmission modes and the linewidth of the cavity. The finesse was measured to be 70 yielding a cavity linewidth of 7 MHz.

The four cavity mirrors are mounted on a solid block of aluminum to provide a high passive stability. Additionally, to ensure a reliable operation despite mechanical vibrations, the cavity can be actively locked. As in the case of the lock of the laser frequency to an atomic transition and the lock of the SHG cavity to the laser, the FM spectroscopy scheme was chosen (see Section 3.2.2). The error signal is again generated by the Labview-controlled FPGA system and fed back to a piezo-electric transducer (PZT), onto which one of the cavity mirrors (M1) is glued.

3.3 Characterization measurements

3.3.1 Characterization setup

The cavity-enhanced SPDC setup was characterized in terms of brightness, indistinguishability and photon statistics in a characterization setup

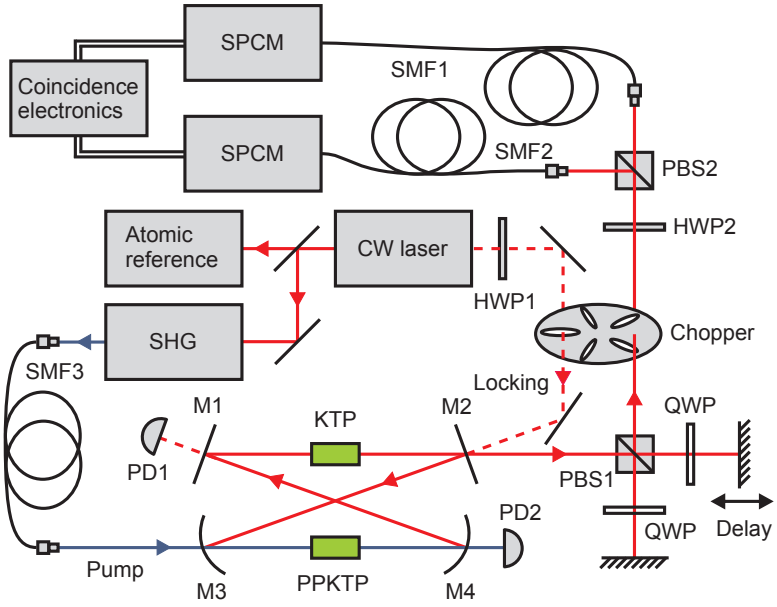

Figure 3.5: Cavity-enhanced SPDC characterization setup. PPKTP, phase-matched nonlinear crystal; KTP, compensating crystal; M1-4, cavity mirrors; PBS, polarizing beam splitter; HWP, half-wave plate; QWP, quarter-wave plate; SMF, single-mode fiber; PD, photodiode; SPCM, single photon counting module.

shown in Fig. 3.5. The cavity output passes through a Michelson-geometry compensator, in which signal and idler photons are split by a polarizing beam splitter (PBS1). Each of the arms of the interferometer contains a quarter-wave plate (QWP) set to rotate the polarization by 90° at a double-pass. The relative delay between the two orthogonally polarized photons of a pair can be varied by changing the arm length of one of the interferometer arms. This delay line is also used to compensate for the initial timing distinguishability induced by the creation process in the birefringent PPKTP. After the recombination of a pair, it is sent through a half-wave plate (HWP2) that determines the measurement basis followed by PBS2. Both output ports of PBS2 are coupled into single-mode fibers and sent to single-photon counting modules (SPCM, Perkin Elmer, AQ4C). The pulse events are registered and processed by coincidence electronics (FAST ComTec, P7888) with a resolution of 1 ns. To eliminate the background noise caused by the locking beam and to protect the SPCM, the locking and measuring intervals are alternated using a mechanical

chopper.

In the experiment, we first set the locking beam to a polarization of 45° and measured the cavity transmission for horizontally (H) and vertically (V) polarized components. The transmission peaks for the two polarizations were overlapped utilizing temperature tuning of the compensating KTP crystal, whereas the temperature of the PPKTP crystal was kept stable at the phase-matching temperature for degenerate operation at 41.4°C. Both crystals were temperature-controlled with a long-term stability of better than 5 mK. The optimization of the pump-beam mode matching was performed by maximizing the count rates on the single-photon detectors.

3.3.2 Brightness

At a pump power of 200 µW the photon rate in each arm (R_{SMF1},R_{SMF2}) was measured to be 142 000 counts/s during the measurement period (when the chopper was open) with a coincidence rate of 34 000 pairs/s. These numbers are not corrected for any losses. The unavoidable accidental coincidence rate R_{acc} in the coincidence time window of $\tau = 256$ ns is calculated to be

$$R_{acc} = R_{SMF1}\ R_{SMF2}\ \tau = 5\ 000 \text{ pairs/s}, \tag{3.2}$$

resulting in a corrected coincidence rate of 29 000 pairs/s, that is, an overall detection efficiency of 20%. Assuming a quantum efficiency of 49% for the SPCM, the collection efficiency is estimated to be 41%.

Considering the bandwidth, a spectral brightness of 450 000 pairs per second per mW of pump power per nm of bandwidth is calculated. Within the crystal bandwidth, the output spectrum consists of roughly 600 modes, the degenerate one at the rubidium D_1 line. The modes are spaced by a FSR of 490 MHz. While the bandwidth of the cavity is 7 MHz, the bandwidth of the correlated photon pairs is smaller than that by a factor of $\sqrt{\sqrt{2}-1}$ [34], i.e., their bandwidth is 4.5 MHz.

Taking into account the limited quantum efficiency of the detectors (49%), the single-mode fiber-coupling efficiency (58%), the escape efficiency of the cavity (82%) and the overall transmission through all optical elements after the cavity (90%) a conditional detection efficiency of 21% is expected. Given this parameter, we estimate the pair production rate of photons in the cavity to be 3.4×10^6 pairs/(s mW).

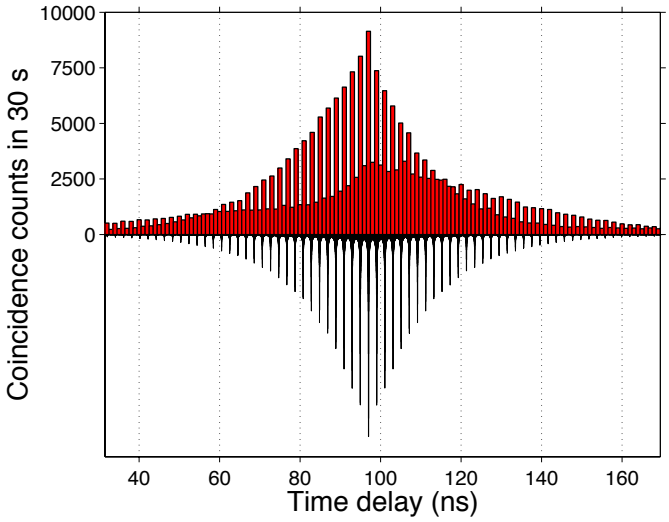

Figure 3.6: Arrival time histogram of photon pairs. Experimental data (upper bars) and theory (lower bars). The visibility of the experimental data are limited by time resolution of the counting electronics and by aliasing.

3.3.3 Arrival-time correlation measurement

The arrival-time correlation function contains information about the temporal shape of the wave function. The temporal photon wave function of photons from cavity-enhanced SPDC shows features based on three time scales: the ring-down time of the cavity, the round-trip time of the cavity and the coherence time of the SPDC process.

We measured the arrival time correlation function (Fig. 3.6) by monitoring the coincidences between detection events on the two SPCM in a time window of 256 ns for 30 seconds in the H/V basis. The experimental data (upper bars) are shown together with the theoretical predictions based on Eq. (2.25) (lower bars). Due to compensation, $\Delta\omega_s = \Delta\omega_i \equiv \Delta\omega$ in our cavity. The time correlation function shows the typical double-exponential decay reflecting the cavity linewidth of $\Delta\nu = 7\,\mathrm{MHz}$, the inverse of the cavity ring-down time. The difference between two peaks corresponds to the round trip time of the cavity of $\tau_{rt} = 2.032\,\mathrm{ns}$ and is the inverse of the free spectral range of 490 MHz. As the round trip time is not an integer multiple of the resolution of our detection system of 1 ns, the arriving photons fall in between two measurement time bins every 1 / 0.032 = 31 peaks leading to a decrease in fringe visibility with

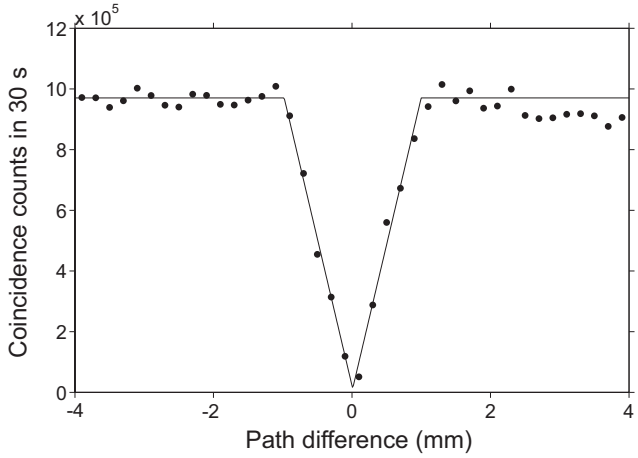

Figure 3.7: Hong-Ou-Mandel Dip. Points show measured coincidence rates, line shows a fit to Eq. (3.4).

a period of 31 peaks as can be seen in Fig. 3.6. These results agree with the theory given in [33] for the case of compensated birefringence. The coherence time of the SPDC process is below the measurement resolution and cannot be measured in this way.

3.3.4 Hong-Ou-Mandel measurement

When the relative delay between the two photons of a pair is changed, their degree of temporal indistinguishability is varied and the Hong-Ou-Mandel effect can be observed. HWP2 was set to rotate the polarization state of the photons from H (V) to +45° (-45°) (Fig. 3.5). When we measure in the ±45° basis and with no delay, signal and idler photons of a pair impinging on PBS2 are indistinguishable and exit on the same output port of PBS2 leading to a drop in the coincidence rate as shown in Fig. 3.7. The coincidence rate in the ±45° basis was measured for different mirror positions in the Michelson-geometry delay line over a range of 8 mm with a step width of 0.2 mm, accumulating coincidence counts at each point for 30 seconds. All coincidences within the time window of $\tau = 256$ ns are counted. The number of accidental counts due to double pairs is calculated using Eq. (3.2) and is subtracted. The data are also corrected for power fluctuations in the pump. These fluctuations are quantified by monitoring the singles counts (R_{SMF1}, R_{SMF2}) in both channels. The coincidences are

then corrected in the following way:

$$R_{coin} = \frac{R_{coin,raw}}{\sqrt{R_{SMF1} R_{SMF2}}} \tag{3.3}$$

As expected for an unfiltered type-II SPDC source, the HOM dip shows a triangular shape [111, 112, 113]. The statistical error bars are too small to be displayed.

The model that we use for the fit is based on the theory given in [24]. The coincidence rate R_{coin} is expressed in terms of the difference Δl between signal and idler paths, the average coincidence rate for large time differences R_{avg} and a parameter ζ with $\zeta = 4/(l|k_s' - k_i'|)$, that depends on the crystal length l and the spectral derivative of the k-parameters of signal and idler photons as introduced in Section 2.1.2:

$$R_{coin}(\Delta l) = R_{avg}\left(1 - \wedge\left(\frac{\Delta l \zeta}{2c}\right)\right) \tag{3.4}$$

The function $\wedge(x)$ takes the value $\wedge(x) = 1 - |x|$ for $|x| < 1$ and $\wedge(x) = 0$ elsewhere. The theoretical prediction of the base-to-base width of the triangle $4c/\zeta = 2.03\,\text{mm}$ agrees well with the fitted value of 2.0 mm. The drop of the coincidence rate for path differences larger than $+2.5\,\text{mm}$ is due to a change in coupling efficiency to the single-mode fibers, as the efficiency was optimized for translation stage positions close to the bottom of the dip. Therefore, data points over $+2.5\,\text{mm}$ were disregarded for the fit. The visibility V of the HOM dip that is defined by

$$V = \frac{C_{max} - C_{min}}{C_{max} + C_{min}}\,, \tag{3.5}$$

where C_{max} and C_{min} are the extreme points of the coincidence rate, is a quantification of the degree of indistinguishability of the two photons of a pair. The fit function displays a visibility of 96% with subtraction of accidental counts and 83% without; the lowest point measured directly shows a visibility of 90%. To reduce the rate of accidental counts due to double pair generation even more, the HOM dip was also measured for a very low pump power of 12 µW. For this measurement the visibility for the lowest data point is 95% with subtraction of the accidentals and 90% for the raw data. This visibility clearly indicates the non-classical character of the down-converted photon pairs and their indistinguishability [114]. It should be noted that all our measurements were done without any spectral filtering.

As demonstrated in this section, the cavity-enhanced photon-pair source fulfills all our requirements in terms of brightness and indistinguishability. The next section describes the careful characterization of the polarization state of the created photon pairs by quantum state tomography.

3.4 Quantum state tomography

As mentioned already in the previous section, many applications in quantum information, quantum imaging and quantum metrology rely on the availability of high-quality single photons or entangled photon pairs. Depending on the kind of application, the requirements on a source of photonic quantum states not only include brightness and efficiency as discussed in Section 3.3.2, but also the degree of indistinguishability, purity and entanglement of the output state. This section presents characterization measurements regarding these properties. The work described in this section was published in reference [104].

Many type-II SPDC sources with and without cavity-enhancement suffer from relatively low indistinguishability of the generated pair-photons that result in a low Hong-Ou-Mandel (HOM) dip visibility [37], e.g., in [33], where the reported visibility was 76.8% and not all reasons for the low visibility could be identified.

A limited visibility can be caused by distinguishing timing information, coherent state-preparation errors, and decoherence. These three possibilities cannot be differentiated by a HOM measurement. Nevertheless, multiparticle states can be fully characterized, including decoherence and distinguishability of particles by tomographic techniques [53]. We apply these techniques to the output pairs from the cavity-enhanced down-conversion source, and show that cavity-enhanced down-conversion not only provides a large photon flux, but is also capable of producing highly indistinguishable photons that can be used to create interesting and useful quantum states such as a high-fidelity NOON state.

3.4.1 Experimental setup

The experimental setup consists of two parts, one for the preparation of the state and the other for its analysis. The state preparation part is based on the high-brightness cavity-enhanced down-conversion source described in detail in the previous section. As principal light source we

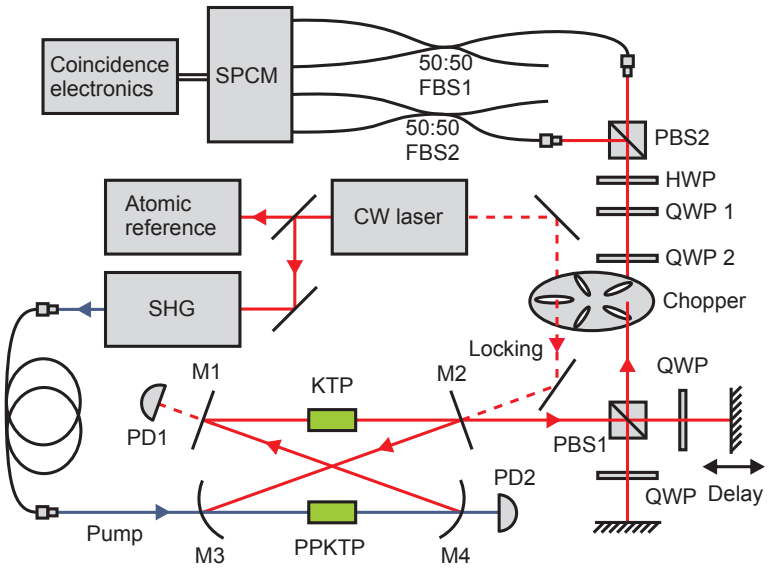

Figure 3.8: Quantum state tomography setup. SHG, second-harmonic generation cavity; PPKTP, phase-matched nonlinear crystal; KTP, compensating crystal; M1-4, cavity mirrors; PBS, polarizing beam splitter; HWP, half-wave plate; QWP, quarter-wave plate; SMF, single-mode fiber; PD, photodiode; FBS, fiber beam splitter; SPCM, single photon counting module.

use a single-frequency diode laser locked to the D_1 transition of atomic rubidium at 795 nm (Fig. 3.8). The frequency-doubled part of the laser pumps a type-II phase-matched PPKTP crystal inside an optical cavity. After the photons leave the cavity, a variable retarder consisting of a polarizing beam splitter, two quarter-wave plates and two mirrors in a Michelson geometry produces a relative delay between the horizontally (H) and vertically (V) polarized photons.

A general polarization analyzer, consisting of a quarter-wave plate (QWP1) followed by a half-wave plate (HWP) and a polarizing beam splitter (PBS2) is used to determine the measurement basis as shown in Fig. 3.8. To generate a NOON state in the H/V basis another quarter-wave plate (QWP2) can be added. The two output ports of PBS2 are coupled to single-mode fibers and split with 50:50 fiber beam splitters. The four outputs are connected to a set of single photon counting modules (Perkin Elmer SPCM-AQ4C). Time-stamping was performed by coincidence electronics. The counting board (FAST ComTec P7888) that was also used in

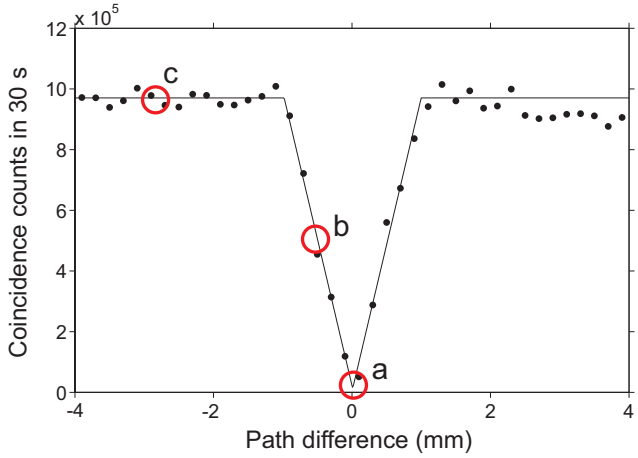

Figure 3.9: Hong-Ou-Mandel data of Fig. 3.2. Labelled points indicate locations of tomographic reconstructions in Fig. 3.10.

the experiment described in Section 3.3 has a reduced resolution of 2 ns, when detection events on all four channels are measured. By considering a time window of 150 ns, that is longer than the coherence time of each individual photon, we can evaluate the coincidences between any two of the four channels. Using this detection setup we can both observe the standard HOM interference that requires two detectors and also implement multi-particle tomography [49, 53, 54, 51].

3.4.2 Multi-particle state tomography

We follow the tomography method developed in [53, 54] and presented in Section 2.2.5 in order to get a polarization characterization of the output state of the cavity-enhanced down-conversion process. In the case of perfect indistinguishability of the photons of a pair, the photons are supposed to be in the state $|\psi^+\rangle$. We evaluated the coincidence counts for the same 10 different wave plate settings of HWP and QWP1 as in [53].

The acquisition time for each wave plate setting was 60 seconds. Applying a maximum likelihood reconstruction, we obtain the polarization density matrix. The singles count rate corrected for accidentals during the measurements was typically 10 000 counts/s.

The density matrix was measured for different delays between the photons corresponding to different positions in the HOM dip, i.e., to different amounts of distinguishing information (Fig. 3.9). We generated different

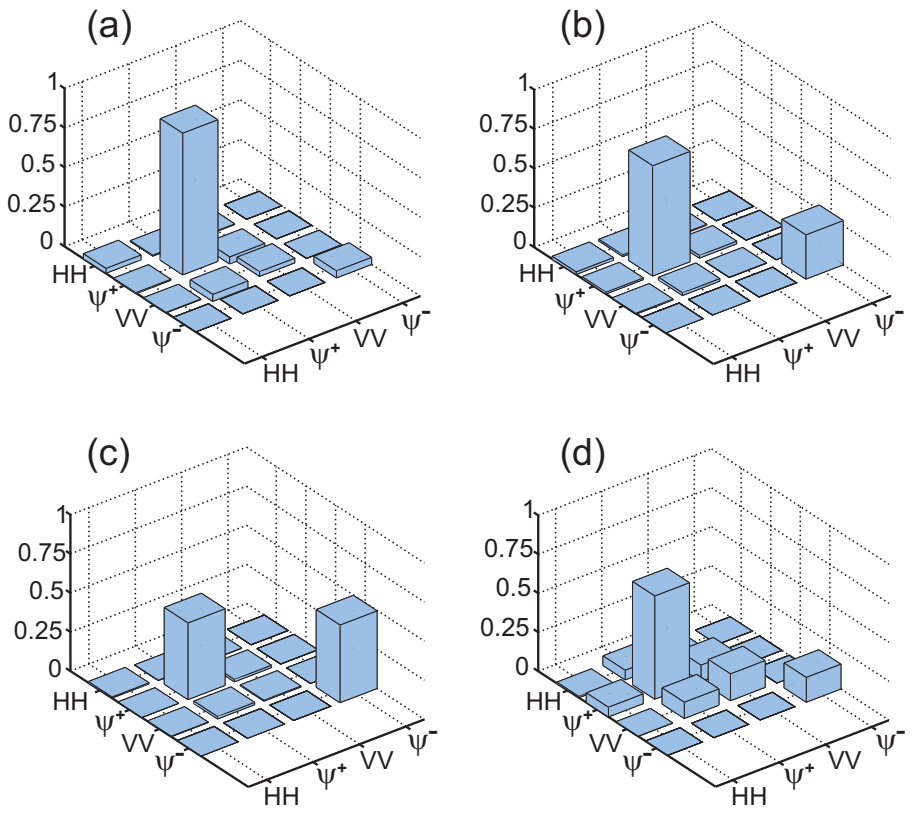

Figure 3.10: Reconstructed polarization density matrices. (a) center of HOM dip, (b) edge of HOM dip, (c) outside of HOM dip (corresponding to points in Fig. 3.9), (d) center of dip, but with system tuned to a different frequency.

states as follows: a) center of dip b) mid-point of dip c) outside of dip. In addition, we produced an unknown state d) by tuning the fundamental laser by about 3.1 GHz from the frequency used in a) – c). No compensations such as the adjusting of the crystal temperature were performed. At this detuning we observe a reduced HOM visibility. Data for d) were taken at the center of the dip, i.e., with zero relative delay.

For all these states we applied the same tomography procedure. Fig. 3.10 shows the elements of the real parts of the density matrices. The imaginary parts are close to zero and are not shown.

We note that the populations in $|\psi^+\rangle$ and $|\psi^-\rangle$ change for different dip positions: a) 94% and 4%, b) 68% and 28%, c) 49% and 50%, d) 66% and 16%. We also note that while b) and d) have a similar amount of HOM dip visibility, their density matrices look very different. In b) only

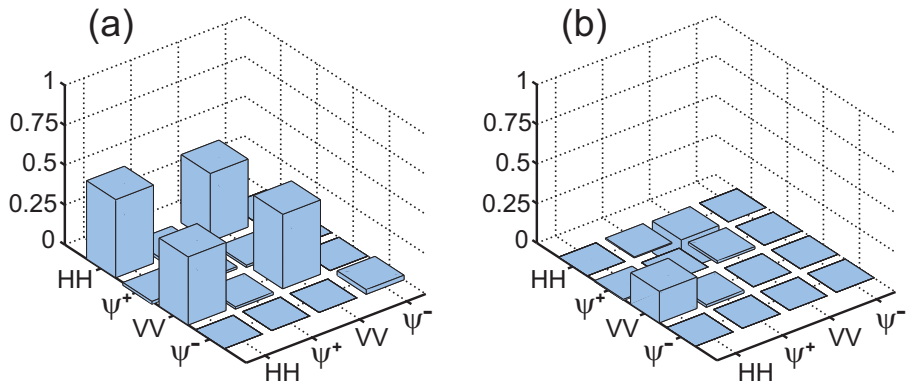

Figure 3.11: Reconstructed NOON state density matrix. (a) Real and (b) imaginary part of the polarization density matrix of the pair-photon state transformed to a two-photon NOON state.

the $|\psi^+\rangle$ and $|\psi^-\rangle$ populations are significant, while d) shows also VV population and coherence between $|\psi^+\rangle$ and VV. Thus b) shows distinguishability while d) shows some distinguishability but also decoherence and coherent errors which cause non-zero off-diagonal elements to appear in the density matrix. This shows clearly that multi-particle tomography provides information not present in the HOM visibility, and can be useful for identifying imperfections in generated states.

3.5 High-quality NOON state

The achieved high indistinguishability of the photons of a pair is the requirement for the generation a high-fidelity NOON state. We introduce another quarter-wave plate (QWP2) before the analyzing part of the setup to create a two-photon NOON state in the H/V basis, which can be written $1/\sqrt{2}(|H_1, H_2\rangle + e^{i\phi}|V_1, V_2\rangle)$. Since the output state of the cavity $|HV\rangle$ is already a NOON state in the basis formed by right-hand (R) and left-hand (L) circular polarization modes $|HV\rangle = i/\sqrt{2}(|L_1, L_2\rangle + |R_1, R_2\rangle)$, this state can be transferred into a NOON state in the H/V basis by sending it through an additional quarter-wave plate at 45 degrees. In Fig. 3.11 real and imaginary parts of the reconstructed density matrix of a NOON state are displayed. The coherence of the state is partly imaginary leading to a phase of $\phi = 0.10$ between HH and VV components (Fig. 3.11.(b)), which is, however, of no importance in the following. The fidelity of this state with the corresponding ideal two-photon

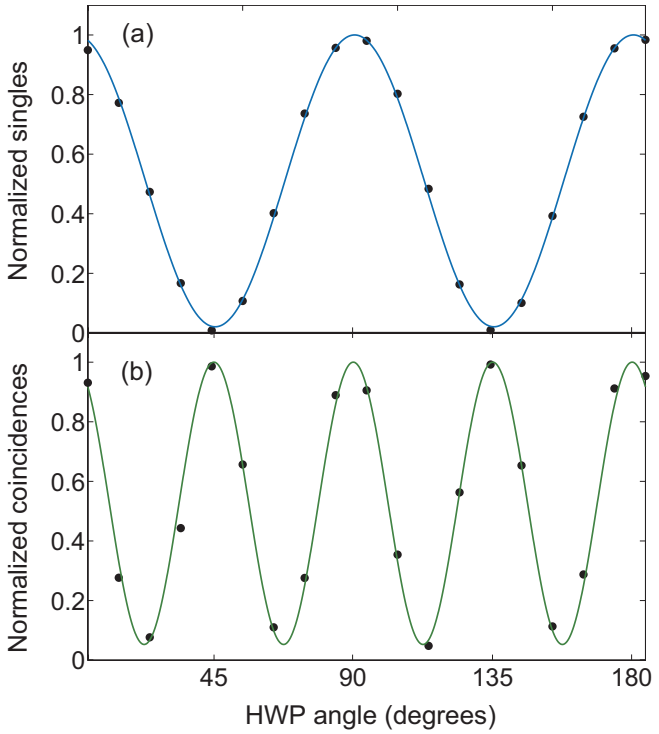

Figure 3.12: Phase super-resolution measurements. (a) Standard phase measurement. Normalized singles detection at the transmitted port of PBS2. In this measurement, only the H polarized part of the pair-photon state was sent to the analyzer. (b) Super-resolving phase measurement. Normalized coincidence detection between reflected and transmitted port of PBS2 for a NOON state input. The shorter period of the coincidence oscillations indicates super-resolution.

NOON state $1/\sqrt{2}(|H_1, H_2\rangle + e^{2i\phi}|V_1, V_2\rangle)$ is 99%, making the state suitable for applications such as phase-estimation [14]. To demonstrate this ability, we performed a super-resolving phase experiment. After passing the NOON state, for this experiment in the circular basis (without QWP1 and QWP2), through the HWP, the coincidence counts between the output ports of PBS2 for different HWP settings were recorded. In Fig. 3.12 the interference fringes of the coincidences are displayed together with singles counts from a measurement in which one polarization of the cavity output was blocked. The pump power in this experiment was 200 μW and accidental coincidences have been subtracted. The period of the coincidence oscillations is shorter by a factor of two compared to the singles, as expected for a two-photon NOON state. The sinusoidal fit function of the

coincidences shows a high visibility of 90%. Reasons for a non-perfect visibility are slight imperfections of the polarization optics and of the beam alignment.

After the description of the photon-pair source in Section 3.2 and its characterization in terms of brightness and HOM visibility in Section 3.3, Section 3.4 extended the characterization to quantum state tomography. The generated NOON states show a metrological advantage compared to coherent states. In order to be useful for a measurement on an atomic ensemble, the photon states need to be atom-resonant. The necessary filtering of the two-photon state will be the subject of the next chapter.

Mr. Bond, they have a saying in Chicago: 'Once is happenstance. Twice is coincidence. The third time it's enemy action'.

– Ian Flemming, *Goldfinger*

4

Atom-resonant heralded single photons

For light-matter interaction at the single-photon level, the spectral resonance of single photons with atomic systems is a crucial requirement. This chapter describes the design and performance of a novel ultra-narrow atomic-based filter. The filtering of photons from the cavity-enhanced down-conversion source of the previous chapter is presented. Furthermore, the implementation of a heralded source of narrowband, atom-resonant single photons is demonstrated.

4.1 Introduction

One of the paramount requirements for atomic quantum metrology with photons is atom resonance and narrow bandwidth of the photons. Other applications of quantum optics that also rely on the interaction of single photons or entangled photon pairs with atomic systems have very similar requirements [3, 95]. Especially, quantum memories in the discrete variable regime that store a single photon in a crystal or atomic vapor are in need of narrowband photon sources [115, 116, 117].

The cavity-enhanced SPDC design described in the previous chapter restricts the photon spectrum to the cavity modes resulting in a multimode spectrum. As the cavity is operated far below threshold to avoid

stimulated processes, no mode competition takes place and all of the cavity modes within the phase-matching bandwidth of the SPDC process are populated. Locking of the cavity to a laser that itself is locked to an atomic transition guarantees the atom resonance of the frequency-degenerate mode. To select this mode, a very narrowband filter is necessary that shows a high extinction ratio over the whole cavity emission bandwidth. Further requirements on the filter are: frequency stability, atom resonance, and single-spatial-mode operation.

Another way to select the degenerate frequency mode is to use one or more consecutive filter cavities or etalons with incommensurate FSR [103, 99, 102, 95]. Usually, one filter cavity is not sufficient, as it would require a very high finesse. The high finesse is necessary to achieve a high extinction ratio over the whole emission spectrum of the SPDC process (large FSR) and at the same time a narrow linewidth, at least smaller than the FSR of the SPDC cavity to block non-degenerate frequency modes. Filter cavities, however, are sensitive to misalignment and need to be locked to an atomic resonance, which creates problems of scattering of locking light into the detection mode.

In our group we followed a new approach and developed a filter that meets all of the above mentioned requirements. Two different versions of the filter were built by A. Cerè and coworkers. A description of setup and performance of the first version was published in [118]. The application of the second version to the filtering of cavity-enhanced SPDC photons was published in [119]. The following section summarizes the working principle of the filter and the implementation of the two filter versions.

4.2 Atomic-based filter

4.2.1 Working principle

While atoms are very specific in what frequencies they *absorb*, the desired filter should *transmit* at those frequencies. It is possible to take advantage of the frequency spectrum of an atomic system to build a filter that is transmissive exactly for those frequencies that are at an atomic resonance. We achieve this using an atomic-based filter, inspired by the "interaction-free measurement" (IFM) strategy of A. Elitzur and L. Vaidman [120, 121, 122] (also known as "quantum interrogation" [123]).

The idea of the IFM proposal is the following: Consider a Mach-

Zehnder interferometer with its two spatial modes between two 50:50 beam splitters. If the interferometer is balanced, the fields interfere destructively in one output port ('bright' port) and constructively in the other ('dark' port). For perfect interference all light exits at the 'bright' port. When an opaque object is inserted into one of the interferometer arms, no interference takes place anymore and the light at the last beam splitter exits equally into both outputs. The detection of a photon in the formerly 'dark' port therefore indicates the presence of the opaque object, although the photon obviously did not interact with the object (otherwise it would have been absorbed). The cost that the experimenter has to pay is that the scheme is probabilistic and does not work every time. The success probability is 25%, because each photon has only 50% chance to be not absorbed and out of these photons only 50% exit at the formerly 'dark' output port. This efficiency can in principle be improved to values arbitrarily close to 100% by taking advantage of the quantum Zeno effect as was shown by P. Kwiat *et al.* [122, 123]. IFM experiments have been proposed and demonstrated in different systems [124] and for a variety of applications including imaging [125] and quantum computing [126, 127, 128].

In our version of the IFM scheme, the opaque object is a hot atomic vapor which is opaque (only) at the transition frequencies. This guarantees that photons, that exit at the formerly 'dark' port, are spectrally at an atomic transition frequency. A very robust and alignment-insensitive interferometer is achieved, since the interferometer arms are not spatial modes, but orthogonal polarization modes. Consequently, our filter has a large angular acceptance and is thus practically insensitive to mode misalignment. This is – along with intrinsic stability and intrinsic atom-resonance – one advantage over filter cavities.

As the Faraday effect between crossed polarizers can be understood as a polarization interferometer, we implement the filter using the paramagnetic Faraday effect (see Section 2.5). To produce an imbalance between the absorption coefficients of the two circular polarizations, a counter-propagating pump beam is applied to optically pump the atomic ensemble into a maximally-polarized spin state, in which the ensemble is transparent for the left-circularly polarized component and absorptive for the right-circularly component. Therefore, if the absorption is saturated, the beam after the cell is left-circularly polarized and the photons exit on both ports of the analyzing polarizing beam splitter with equal probability. The efficiency of 25% is mathematically described by the factor of 1/4 in Eq. (2.113).

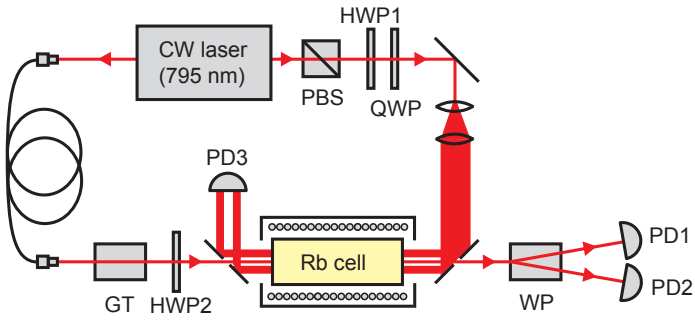

Figure 4.1: Setup of first filter version. PBS, polarizing beam splitter; HWP, half-wave plate; QWP, quarter-wave plate; WP, Wollaston prism; GT, Glan-Thompson polarizer; PD, photodiode.

4.2.2 First filter version

The setup of the first filter version is shown in Fig. 4.1. A diode laser locked to the $5^2S_{1/2}(F{=}2){\rightarrow}5^2P_{1/2}(F'{=}1)$ transition of the D_1 line of ^{87}Rb at 795 nm is used as probe beam. The interferometer setup consists of two polarizers, a Glan-Thomson polarizer and a Wollaston prism, both with extinction ratios of $>10^5$. The atomic sample is a hot rubidium vapor of natural abundance contained in a cylindric glass cell. The cell has a length of 15 cm and a diameter of 2.5 cm and the windows are AR coated on both sides. The cell is heated to a temperature of 65°C to achieve an optical depth of 1.1. A coil around the cell produces a small orienting magnetic field. The cell is shielded against other external magnetic fields, such as the earth magnetic field by a μ-metal shielding.

To prepare the atomic sample, the atoms are optically pumped by a circularly polarized pump beam resonant to the same $F{=}2{\rightarrow}F'{=}1$ transition of ^{87}Rb as the probe beam. In order to send the pump beam counter-propagating to the probe beam, mirrors with holes in the center are used (Fig. 4.1). The pump beam of large beam diameter (12 mm) is reflected partially by these mirrors, while the probe beam passes through the holes. Due to Doppler shifts, the optical pumping only effects a portion of the thermal velocity distribution and creates circular dichroism in a narrow spectral region. The atom-resonant fraction of the originally H-polarized beam is partly rotated to V-polarization. After the cell, a Wollaston prism splits the beam in H- and V-polarized components. The filter achieves a transmission of 14.6% and a power-broadened sub-Doppler linewidth of 80 MHz. Off-resonance, the extinction ratio is given by the extinction of

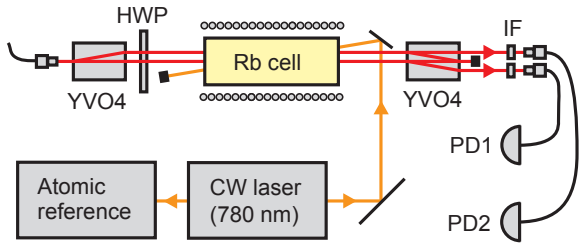

Figure 4.2: Setup of second filter version. HWP, half-wave plate; YVO4, Yttrium Vanadate crystal; IF, interference filter; PD, photodiode.

the polarizers and was measured to be $\geqslant$35 dB.

4.2.3 Second filter version

The filter design was changed and improved in several ways, mainly in order to be able to use the filter at the single-photon level and with two orthogonal input polarizations.

One improvement is that the pump beam which was frequency-degenerate with the probe beam in the first version, is now implemented by a laser resonant to the F=2→F'=3 transition of the D_2 line of ^{87}Rb. The large spectral separation between pump and probe beam enables the removal of contaminating pump photons by spectral filters before the detection setup. Interference filters centered on 795 nm further reject the 780 nm pump light with an extinction ratio of $>10^5$. A pump power of up to 20 mW is used. In this new setup, the beam diameter of the pump beam is chosen to be smaller in order to achieve a more efficient pumping. Instead of mirrors with holes in the center, d-shaped mirrors are used and pump and probe beams form a very small angle.

Generation of narrowband 2-NOON states requires simultaneous filtering of both orthogonal polarizations. Therefore, the polarizers (Glan-Thompson polarizer and Wollaston prism) were replaced by two YVO_4 crystals. The first crystal separates H- and V-polarized light by 1 mm and lets the two polarization modes travel parallel to each other through the rubidium vapor cell (Fig. 4.2). The vapor cell contains isotopically pure ^{87}Rb to increase the optical depth at the same temperature compared to a cell of natural abundance. The windows of the cell are wedged and angled to reduce back-reflection, mainly of the strong pump beam, into the single-photon detectors. For the same reason, the output beams are coupled into

single-mode fibers. Despite these measures, for high pump power levels, a contribution of pump light on the photon counters is seen. To reduce this contribution to a level of the same magnitude than the detector dark counts, the alignment of the pump beam needs to be adjusted.

A second YVO_4 crystal introduces a second relative displacement, which can re-combine or further separate the photons, depending on polarization. Separated photons are collected, while re-combined photons are blocked. A half-wave plate is used to switch between the "active" configuration, in which only photons that change polarization in the cell are collected, and the "inactive" configuration, in which photons that do not change are collected. In the "active" configuration, the system acts as an IFM detector for polarized atoms: a photon is collected only if it experiences a polarization change, i.e., if it is resonant with the optically pumped atoms, which absorb one circular component of the photon polarization state.

This setup is well suited for blocking the non-degenerate modes of the cavity-enhanced SPDC setup, since the neighboring modes of the degenerate mode at the rubidium transition are already 490 MHz detuned and therefore outside of the filter linewidth of 80 MHz. The out-of-band extinction ratio is $\geqslant$35 dB over the whole SPDC phase-matching bandwidth. The filter transmission is optimized by adjusting the overlap between pump and single-photon mode, the rubidium vapor temperature and the magnitude of a small orienting applied magnetic field. The temperature is set to 65°C, which corresponds to an atomic density of $5 \cdot 10^{11}\,\mathrm{cm}^{-3}$. The measured filter transmission of 10.0% for horizontal polarization and 9.5% for vertical polarization is limited by pump power.

4.3 Filtering of photon pairs

4.3.1 Time-correlation measurements

The improved version of the atomic-based filter can be used to filter the down-converted photons. The whole setup is shown schematically in Fig. 4.3. After leaving the SPDC cavity, the generated photon pairs are coupled into single-mode fiber and brought to a different optical table in our laboratory where the filtering setup is located. The normal photo-detectors are replaced by fiber-coupled avalanche photodiodes (APD, Perkin Elmer SPCM-AQ4C). The APDs show a dark count rate of approximately 400 counts per second. The measured contribution from pump photons is be-

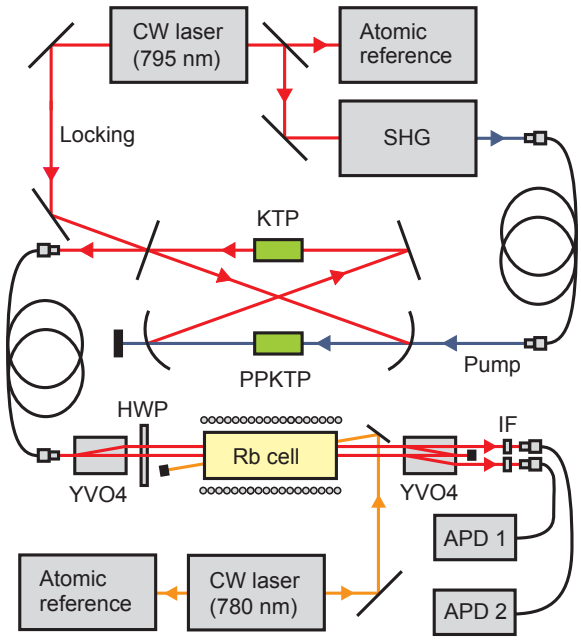

Figure 4.3: Setup for time-correlation measurement. SHG, second-harmonic generation cavity; PPKTP, phase-matched nonlinear crystal; KTP, compensating crystal; YVO4, Yttrium Vanadate crystal; HWP, half-wave plate; IF, interference filter; APD, avalanche photodiode.

low the detectors' dark count rate. Photon detections are recorded by a counting board (FAST ComTec P7888) for later analysis.

First, the time distribution of the difference in arrival time between signal and idler photons, i.e., the $g^{(2)}_{S,I}(\tau)$-function, is measured with the filter in the "inactive" configuration at a much reduced pump power. The histogram of the difference in arrival time between detection events in the two APDs is shown in Fig. 4.4. It corresponds to the measurement of the $g^{(2)}_{S,I}(\tau)$-function directly after the SPDC cavity presented in Section 3.3. The blue bars represent the coincidence event detections within time bins of 1 ns, the resolution of the counting board. The black bars, drawn inverted for better visibility, show the theoretical prediction based on Eq. (2.25). The height of the theory histogram, the only free parameter, has been set to match the height of the data. Experimental and theoretical results are in excellent agreement. When the filter is "active", the arrival time difference histogram shows a smooth double-exponential shape, without multi-mode interference (Fig. 4.5). This already indicates that only

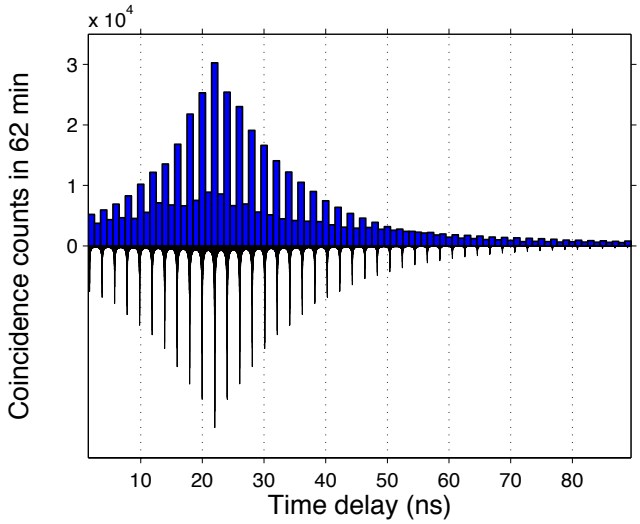

Figure 4.4: Arrival time histogram of unfiltered photon pairs. Experimental data (upper bars) and theory (lower bars). The frequency-comb structure is reflected by a comb-like structure in the temporal domain. The visibility of the experimental data is limited by time resolution of the counting electronics.

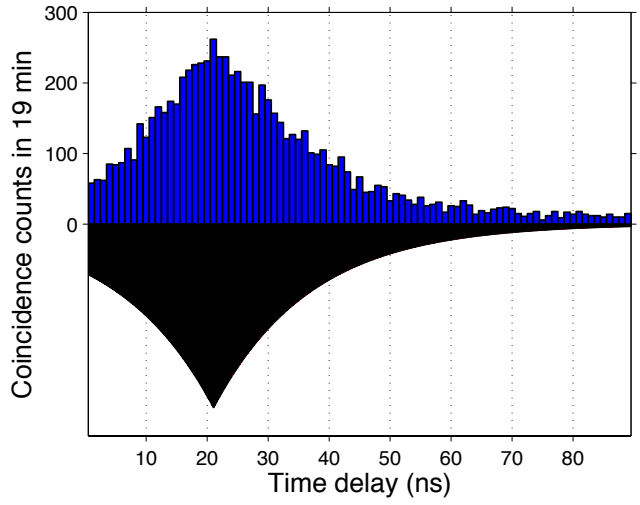

Figure 4.5: Arrival time histogram of filtered photon pairs. experimental data (upper bars) and theory (lower bars). The disappearance of the comb structure in the filtered case indicates the single-mode character of the filtered fields.

a single frequency mode is transmitted through the filter. The theory (lower black bars) is given by Eq. (2.25) for a single mode ($\Gamma_{s,i}=\gamma_{s,i}/2$). It should be noted that the data shows a very low background noise level. Throughout, raw data are shown; background coincidences have not been subtracted.

In this experiment we are interested in time correlations, but it is interesting to ask if other kinds of correlations and possible entanglement, e.g., in polarization or in frequency, are also preserved by the filter, because this will become important for the filtering of NOON states in the following chapter. By design, the filter should transmit nearly equally different frequency and polarization components of the selected cavity mode, preserving correlations: absorptive and refractive effects vary on the scale of the 80 MHz absorption linewidth, large relative to the 7 MHz of the cavity mode. Also, the axial magnetic field scrambles any linear birefringence or dichroism, giving equal response for the two linear polarizations.

4.3.2 Atom-resonance

To measure the atom-resonant fraction, we let the filtered photons of the signal arm propagate through a rubidium vapor cell (Fig. 4.6). At room temperature, the cell's optical density (OD) is low (0.3) corresponding to a transmission of 74% and coincidences between the detection events on the two APDs are observed (Fig. 4.7, upper green bars). By heating the rubidium cell, an optical density of 6, or 0.25% resonant transmission, is reached. The coincidences drop to the background level (Fig. 4.7, lower

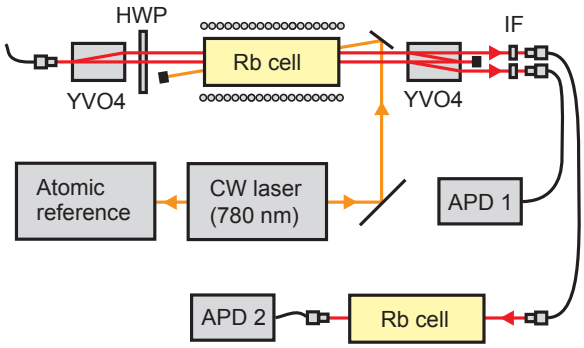

Figure 4.6: Setup for measuring atom-resonant fraction. YVO4, Yttrium Vanadate crystal; HWP, half-wave plate; APD, avalanche photodiode.

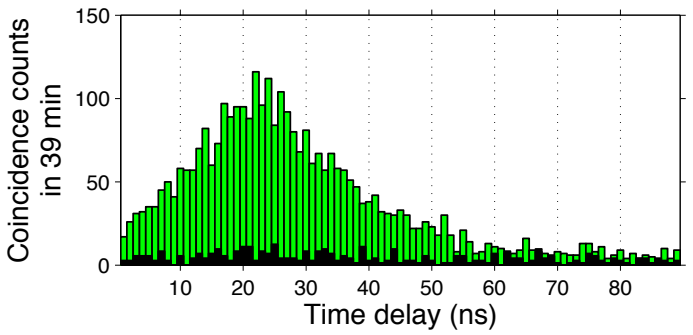

Figure 4.7: Arrival time histogram of atom-resonant photons. Signal photons pass through a rubidium vapor cell at an optical density of 0.3 (upper green bars) and at an optical density of 6 (lower black bars).

black bars). Within a coincidence window of 40 ns, the ratio of raw OD 0.3 coincidences to raw OD 6 coincidences is 11.6:1, indicating rubidium resonance of at least 94% of the photons.

4.4 Heralded single-photon source

For a heralded single-photon source of high quality it is important that the trigger photon heralds the presence of only one photon with negligible contributions from higher photon numbers. The figure of merit for that is the conditional signal auto-correlation function at $\tau = 0$, $g_c^{(2)}(0)$, introduced in Section 2.1.6.

We measure $g_c^{(2)}(0)$ as shown in Fig. 4.8. The signal mode is split by a 50:50 beam splitting fiber and the coincidences between the idler detector (APD1) and the two signal detectors (APD2 and APD3) are analyzed. The detection of an idler photon defines a coincidence window of 40 ns, symmetrical around the detection time. Individual and coincident detections in this time window give singles counts N_2, N_3, while detections at both APD2 and APD3 give the coincidence count N_{23}. N_{23} corresponds to unwanted multi-photon contributions which are very low in our experiment. To accurately estimate N_{23}, we measure for large coincidence windows of up to 2000 ns, extrapolate down to 40 ns, and multiply by two, to account for possible bunching [40, 34]. N_1 is the number of idler trigger events. $g_c^{(2)}(0)$ is given by Eq. 2.29. The probabilities can be deduced from the detected counts by normalizing on trigger events: $p_{ab} = N_{23}/N_1$,

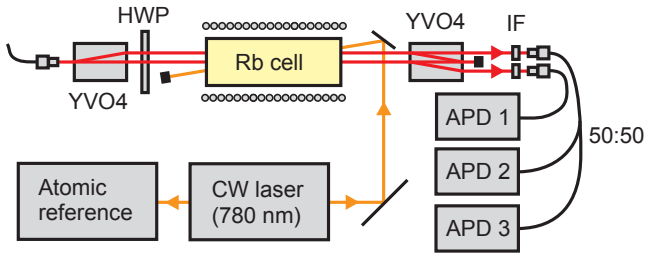

Figure 4.8: Setup for measuring $g_c^{(2)}(0)$. YVO4, Yttrium Vanadate crystal; HWP, half-wave plate; IF, interference filter; APD, avalanche photodiode.

$p_a = N_2/N_1$, $p_b = N_3/N_1$. This results in

$$g_c^{(2)}(0) = \frac{p_{ab}}{p_a p_b} = \frac{N_{23} N_1}{N_2 N_3}. \tag{4.1}$$

We note that this gives an upper limit for $g_c^{(2)}(0)$, due to the conservative bunching factor and the finite time window. We find $g_c^{(2)}(0) \leq 0.040 \pm 0.012$, 80 standard deviations below the classical limit of 1.

All this is a dream. Still examine it by a few experiments. Nothing is too wonderful to be true, if it be consistent with the laws of nature.

– Michael Faraday, *Laboratory journal entry #10 040*

5

NOON state atomic magnetometry

Atomic magnetometers are among the most sensitive instruments for measuring low-frequency magnetic fields. In recent years, the sensitivity of atomic magnetometers has improved so much that it is approaching fundamental limits: The projection noise of atoms and the shot noise of light. This chapter describes how NOON states can be used to improve the performance of these magnetometers beyond the shot-noise limit of light. The chapter presents the careful characterization of the atomic vapor cell, the analysis of experimental results on super-resolution, reconstruction of the density matrix and the quantification of the metrological advantage of the NOON state in terms of Fisher information.

5.1 Introduction

The NOON state described in Chapter 3 acquires the highest information per photon in a phase estimation measurement. NOON-state probing is therefore especially attractive for measurements of delicate systems, which can be damaged or altered by excessive illumination. Examples of delicate systems are single atoms [3], single molecules [5] and quantum simulators [6] as well as atomic ensembles, including atomic magnetometers. Furthermore, the optical sensing of much larger and much more complex systems,

such as biological cells, is limited by the power of the probe light [9] and could potentially benefit from quantum-light probing techniques.

NOON states have proven to achieve super-resolution [11, 14] and to break the shot-noise limit [129, 15]. To date, however, all measurements with NOON states that show an advantage in sensitivity have been performed on robust systems, in measurements of wave-plate orientations [14, 129, 60], liquid crystal wave retarders [15] and optical path differences [130]. For these robust systems, the advantage provided by NOON states could also be obtained by using a larger number of non-entangled particles. Instead, for delicate systems, the entanglement produces an advantage unobtainable by other means.

One major goal of this thesis is to demonstrate the metrological advantage of NOON states on such a delicate system: the atomic ensemble of an atomic magnetometer. Atomic magnetometers rely on interactions between atom-tuned probe light and atomic vapors, often in form of the Faraday effect (see Section 2.5). The Faraday rotation angle is linear

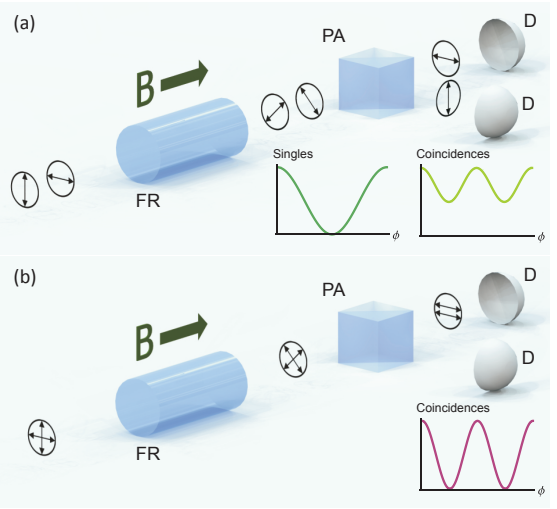

Figure 5.1: Working principle of an atomic magnetometer. Polarized photons pass through a rubidium vapor cell (FR) where they experience an optical rotation dependent on the applied magnetic field $\vec{B}$ (the Faraday effect) and are detected by a polarization analyzer (PA) with photon counting detectors (D). (a) With non-entangled photons, "singles detection" can give high visibility, while "coincidence detection" can give (low visibility) super-resolution. (b) By Hong-Ou-Mandel interference, NOON states can give both super-resolution and high visibility, providing more information per photon than possible without entanglement.

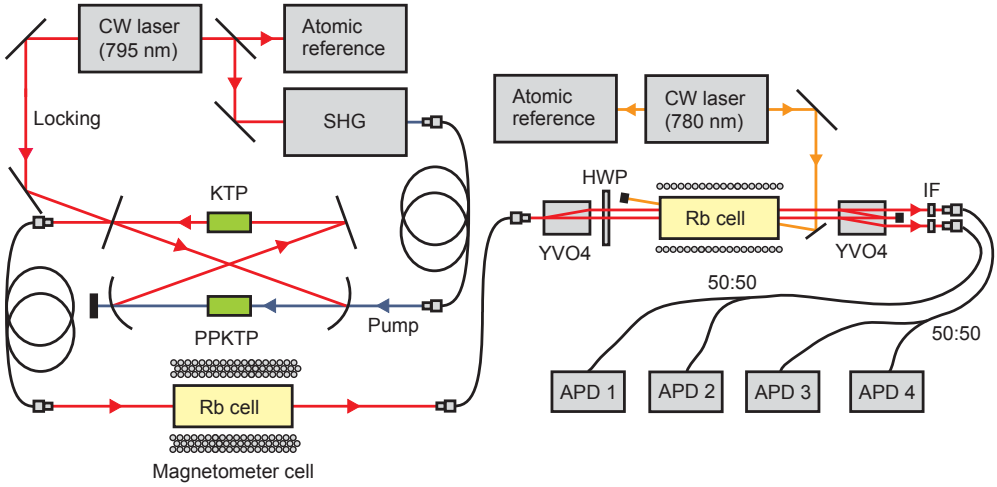

Figure 5.2: NOON state magnetometry setup. SHG, second-harmonic generation cavity; PPKTP, phase-matched nonlinear crystal; KTP, compensating crystal; YVO4, Yttrium Vanadate crystal; HWP, half-wave plate; IF, interference filter; APD, avalanche photodiode.

with the component of the applied magnetic field in the direction of beam propagation and can therefore be used as a way to measure the magnetic field [131, 21]. A polarimeter setup after the atomic vapor cell analyzes the rotation angle from which the magnetic field is estimated (Fig. 5.1). An extensive review of optical magnetometry was written by D. Budker and M. Romalis [19].

While so far atomic magnetometry used coherent light as probe beam, a polarization NOON state ideally shows high-visibility super-resolution and improves the sensitivity by a factor of $\sqrt{N}$. In this chapter we demonstrate sensitivity enhancement of an atomic magnetometer using the narrowband, atom-tuned NOON states described in the previous chapters. The work presented in this chapter was submitted for publication [132].

5.2 Magnetometry setup

The experimental setup consists of three stages: the generation stage of the NOON state, the atomic magnetometer, and the detection stage (Figs. 5.1 and 5.2).

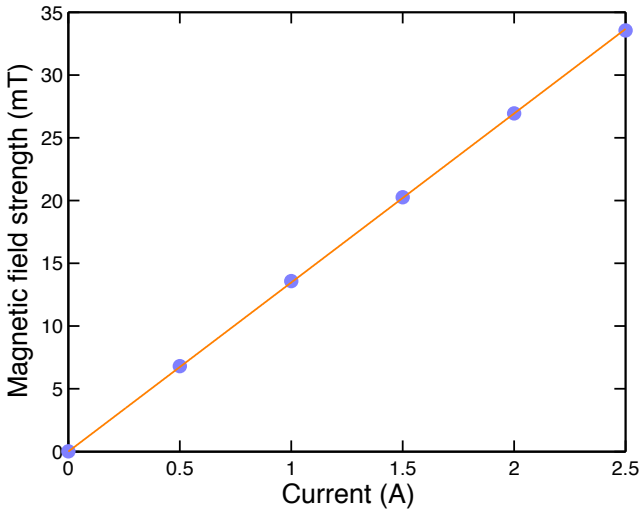

Figure 5.3: Magnetic field calibration. Circles represent data points, line shows linear fit. The magnetic field strength increases linearly with the current through the coil.

5.2.1 Generation stage

The generation stage is formed by the cavity-enhanced SPDC source described in Chapter 3. The NOON states produced in the SPDC cavity are of the form $(|L_1, L_2\rangle + e^{i\phi}|R_1, R_2\rangle)/\sqrt{2}$ and resonant to the $5^2S_{1/2}$(F=2)→ $5^2P_{1/2}$(F'=1) transition of the D_1 line of ^{87}Rb. The photon pairs are coupled into a single-mode optical fiber and sent to the magnetometer.

5.2.2 Magnetometer stage

The atomic magnetometer consists of a 75 mm-long vapor cell containing ^{85}Rb and ^{87}Rb at an isotope ratio of 200:1. An isotopically purified rubidium cell offers the possibility to lock the NOON state frequency to a ^{87}Rb transition and at the same time enables high transmission of the NOON state through the magnetometer cell. The NOON state is 1.5 GHz detuned from the closest (D_1: F=3→F'=2) ^{85}Rb resonance. The cell is temperature stabilized at 70°C to achieve a high optical density.

A large magnetic field of up to 50 mT is applied by running an electric current of up to 4.5 A through a coil of copper wire. A first calibration of the magnetic field strength was performed using a linear magnetic field sensor for currents between 0 A and 2.5 A (Fig. 5.3). The calibra-

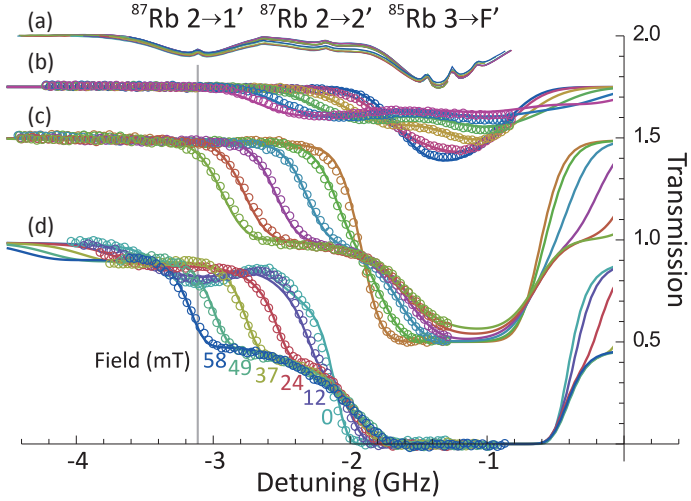

Figure 5.4: Spectroscopic characterization of the atomic ensemble. Circles show measured values, curves show predictions of first-principles model (see text). (a) Saturated-absorption spectra acquired with a natural-abundance cell at room temperature, as a frequency reference. Horizontal axis shows detuning from the center of the D_1 spectral line. (b)-(d) Transmission spectra for the ^{85}Rb magnetometer cell at temperatures of 22°C, 53°C and 83°C, respectively. For each temperature, spectra with measured field strengths (in mT) of 0, 12, 24, 37, 49, and 58 are shown, in order of increasing line broadening. Grey vertical line shows ω_{NOON}, the probe detuning. For clarity, parts (a)-(c) have been offset vertically by 1, 0.75, and 0.5, respectively.

tion range was limited by saturation of the flux-gate voltage. This first calibration was improved by using the atomic ensemble itself as an accurate way to measure the magnetic field. We took transmission spectra at various temperatures and magnetic fields and compared the measured absorption spectra to theoretical predictions (Fig. 5.4). Also, the isotope ratio and the cell temperature were quantified in this way. The frequency scale of the spectra is determined from simultaneous saturated absorption spectroscopy. Spectra taken at temperatures 22°C, 53°C, and 83°C, and fields in the range 0-58 mT are fitted with first-principle model predictions. The grey vertical line indicates the frequency of the NOON state ω_{NOON}, 1.5 GHz detuned from the closest ^{85}Rb transition. This operating point gives strong Faraday rotation with low absorption over the range 0-49 mT. Absorption from the small (0.5%) residual ^{87}Rb component can be seen in Fig. 5.4.(d). The cell with no buffer gas and no wall coatings that might preserve polarization, is modeled as a thermal equilibrium,

Doppler-broadened vapor subject to Zeeman shifts in the intermediate regime [133]. The atomic structure is calculated by diagonalization of the atomic Hamiltonians

$$\hat{H}_{\mathrm{At}}^{(\mathrm{iso})} = \hat{H}_{0}^{(\mathrm{iso})} + \hat{H}_{\mathrm{HFS}}^{(\mathrm{iso})} + \hat{H}_{\mathrm{Z}}^{(\mathrm{iso})}, \tag{5.1}$$

where $\hat{H}_{0}^{(\mathrm{iso})}$ is the energy structure of the atom, including fine-structure contribution, $\hat{H}_{\mathrm{HFS}}^{(\mathrm{iso})} = g_{\mathrm{HFS}}\mathbf{J}\cdot\mathbf{I}$ is the hyperfine contribution, and $\hat{H}_{\mathrm{Z}}^{(\mathrm{iso})} = \mathbf{B}\cdot(\mathbf{g_J J} + \mathbf{g_I I})$ is the Zeeman contribution. This gives field-dependent energy eigenstates, from which the complex linear optical polarizability is calculated, including radiative damping. The complex refractive index $n_{\pm}$ for $\sigma_{\pm}$ polarizations is computed including Doppler broadening and a temperature-dependent atom density given by the vapor pressure [134, 133] times the isotope fraction. The transfer function for the cell is calculated from the integral of the index along the beam path, including a measured drop in field strength of 15% from the center to the faces of the cell. Fig. 5.5 shows the computed phase retardation for the $\sigma_{\pm}$ polarizations at the frequency of the F=2→F'=1 transition. The differential $\sigma_{\pm}$ retardation produces optical rotation. Contribution of ^{85}Rb is two orders of magnitude larger than that of ^{87}Rb, as expected from the isotopic ratio, and in the opposite sense. Fig. 5.6 shows the attenuation for both polarizations. It should be noted that for large fields, both, the absorption and the phase variation increase for σ_{-} polarization. The reason is that for larger fields the Zeeman splitting of the ^{85}Rb F=3→F'=2

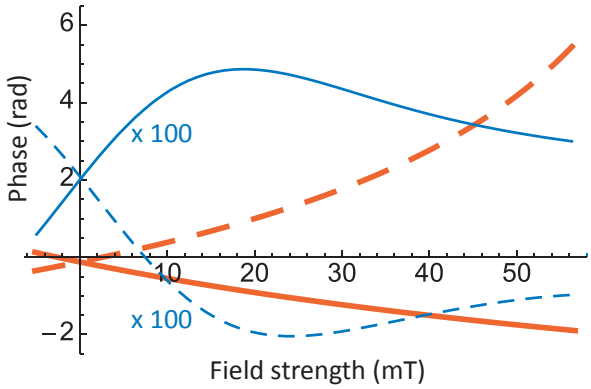

Figure 5.5: Phase retardation vs. field strength, computed from model. Polarizations are shown by solid (σ_{+}) and dashed (σ_{-}) curves. Isotopic contributions are shown by thick orange (^{85}Rb) and thin blue (^{87}Rb) lines.

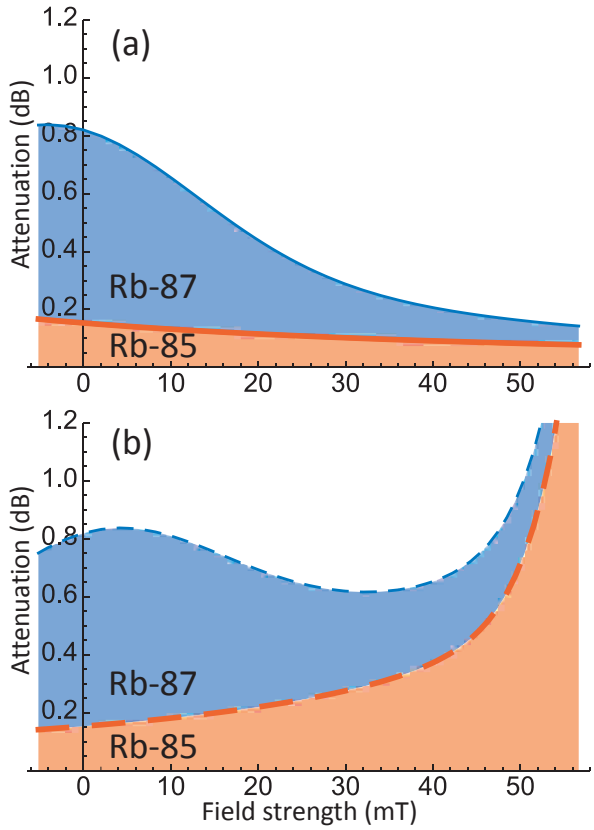

Figure 5.6: Attenuation vs. field strength, computed from model. Isotopic contributions are shown by thick orange (^{85}Rb) and thin blue (^{87}Rb) lines. (a) Attenuation for σ_+ polarization. (b) Attenuation for σ_- polarization.

transition increases and the σ_- line moves closer to the optical frequency of the NOON state.

5.2.3 Detection stage

After the magnetometer, the polarization-rotated NOON state is sent through a single-mode fiber to the detection stage. It consists of the ultra-narrowband filter based on the "interaction-free measurement" idea presented in Chapter 4 and single-photon detectors. The detection setup works in post-selection: It selects those NOON state photon pairs that are at the Rb transition frequency [118, 119].

In the filter setup (Fig. 5.2) a first Yttrium Vanadate (YVO4) crystal

splits H and V components into two parallel beams that travel through an isotopically pure ^{87}Rb cell. The atoms are optically pumped by a circularly polarized laser resonant to the F=2→F'=3 transition of the D_2 line at 780 nm. At a pump power of 16.6 mW the filter efficiency was 13.8%. After the filter setup, the two separated horizontal (H) and vertical (V) polarization modes are coupled into single-mode fibers, detected by single-photon counting detectors and processed by counting electronics. Polarization-resolved coincidence detection, in the H/V basis, efficiently determines the degree of rotation, and is described by projective measurement. A pair of counters on each polarization channel allows post-selection of all possible outcomes, i.e., HH, HV, and VV polarizations. The probability of observing an outcome i is

$$P_i(B) = \mathrm{Tr}\{\hat{\Pi}_i \hat{T}(B) \hat{\rho} \hat{T}^\dagger(B)\}, \tag{5.2}$$

where $\hat{\rho}$ is the two-photon state before the cell, B is the magnetic field, $\hat{T}(B)$ describes the transmission through the cell, and $\hat{\Pi}_i$ is the positive-operator-valued measure (POVM) element for the i'th outcome.

If $t_\pm$ are the transmission amplitudes for $\sigma_\pm$ polarizations, then $\hat{T}(B) = \mathrm{diag}(t_+^2, t_+t_-, t_-t_+, t_-^2)$ in the $\sigma_\pm$ basis. In the H/V basis, $\hat{\Pi}_{HH}, \hat{\Pi}_{HV}$ and $\hat{\Pi}_{VV}$ are $\mathrm{diag}(1,0,0,0)$, $\mathrm{diag}(0,1,1,0)$, and $\mathrm{diag}(0,0,0,1)$, respectively. A completely analogous description is used for single-photon probabilities. Due to atomic absorption and scattering, $|t_\pm| < 1$ so that $\sum_i P_i < 1$ in general.

5.3 Magnetometry results

5.3.1 Super-resolution measurements

The detection apparatus registers both, single and coincident detection events. When the magnetic field is increased, the V singles detections show a small oscillation amplitude, due to a small imbalance between transmission of H and V polarization. This oscillation period is taken as phase reference (Fig. 5.7). The coincidence curves oscillate showing a high visibility at twice the frequency of the singles curve. It should be noted that no background was subtracted. All curves are taken between 0 and 50 mT and are offset by 8°, due to the orientation of the fiber collimator before the filter setup.

The NOON state in the circular basis can be written in the following way in the H/V basis: $(|L_1, L_2\rangle + e^{i\phi}|R_1, R_2\rangle)/\sqrt{2} = |H_1, V_2\rangle$. When

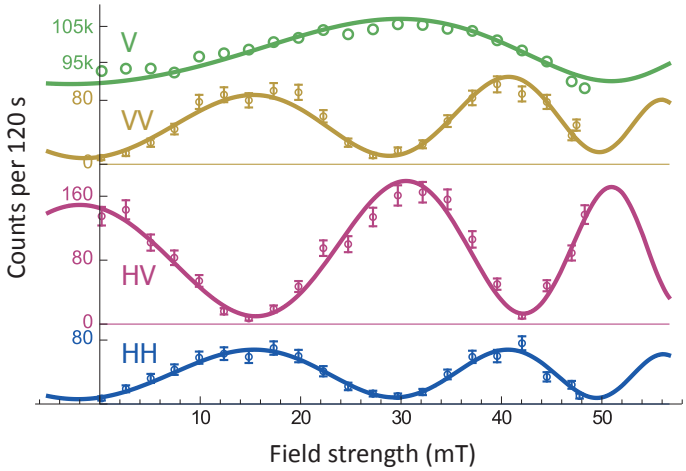

Figure 5.7: Magnetometry super-resolution measurements. Singles (thousands) and coincidences versus field strength in mT. Counts per 120 seconds for V, HH, HV, and VV outcomes, respectively. Circles represent measured data with errorbars given by the standard deviation. Curves show best fit to Eq. (5.2) with the elements of the state $\hat{\rho}$ as free parameters.

the NOON state rotation is zero, the photons of a pair split on the first polarizing beam splitter of the filter setup and give maximum HV coincidences for zero field (Fig. 5.7). When the magnetic field is increased, the polarization plane of the NOON state is rotated and the number of HV coincidences decreases. At a rotation of $\pi/4$ (at approx. 15 mT), the photon pairs are indistinguishable and perform the HOM effect: Ideally, both photons of a pair are detected in the HH or in the VV mode with 50% probability. This leads to a minimum of HV coincidences and a maximum of HH and VV coincidences with an amplitude half as large as for HV coincidences. For larger rotations this behavior repeats periodically. The oscillations become faster for larger fields as predicted from the model (see Fig. 5.5).

It is also possible to see the small effect of residual ^{87}Rb: The second maximum of the HV coincidences curve is higher than the first one because the first one suffers from some absorption from the 87 line. At the magnetic field of the second maximum, the 87 line broadens, which results in less absorption.

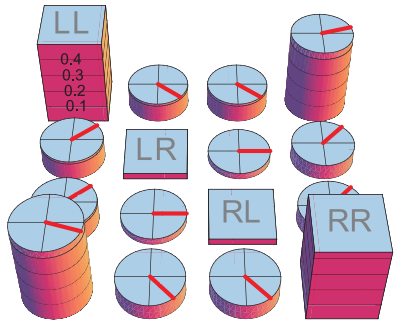

Figure 5.8: Best-fit NOON state density matrix $\hat{\rho}$. Radial lines on off-diagonal elements indicate phases.

5.3.2 Density matrix

From the coincidence data in Fig. 5.7 and the known field-dependent transmission coefficients $t_{\pm}(B)$ it is possible to perform polarization quantum state tomography of the NOON state. The reconstruction procedure is similar to the standard scheme introduced in Section 3.4. No additional wave plates are necessary, since the polarization rotation in the atomic ensemble itself gives information in different bases. A least-squares optimization determines $\hat{\rho}$.

The reconstructed density matrix $\hat{\rho}$ in the R/L basis is shown in Fig. 5.8. The figure shows the elements of the real part of the matrix with the phases shown by radial lines on the off-diagonal elements. Large coherence between $|2_L, 0_R\rangle$ and $|0_L, 2_R\rangle$ components is evident. The density matrix describes a state with high purity $\mathrm{Tr}\{\hat{\rho}^2\} = 0.88$ and low photon distinguishability [53] $\langle\psi^-|\,\hat{\rho}\,|\psi^-\rangle = 0.02$. The state show a high fidelity of $\langle N_\phi|\,\hat{\rho}\,|N_\phi\rangle = 0.90$ with the ideal NOON state $|N_\phi\rangle \equiv (|2_L 0_R\rangle + \exp[i\phi]\,|0_L 2_R\rangle)/\sqrt{2}$, $\phi = 0.44$ rad. The tomography confirms the generation of a NOON state with ideal characteristics for atomic measurements: single-spatial mode, near-perfect indistinguishability, and extremely high temporal coherence.

5.3.3 Fisher information

In order to quantify the metrological advantage of the NOON state probing, we analyzed the super-resolution results in terms of Fisher information (see Section 2.3.3). From the coincidence data we computed the Fisher information per incident photon into the magnetometer as a function of

the magnetic field strength. The colored regions in Fig. 5.9 represent the amount of information that is acquired by HH, HV and VV coincidence

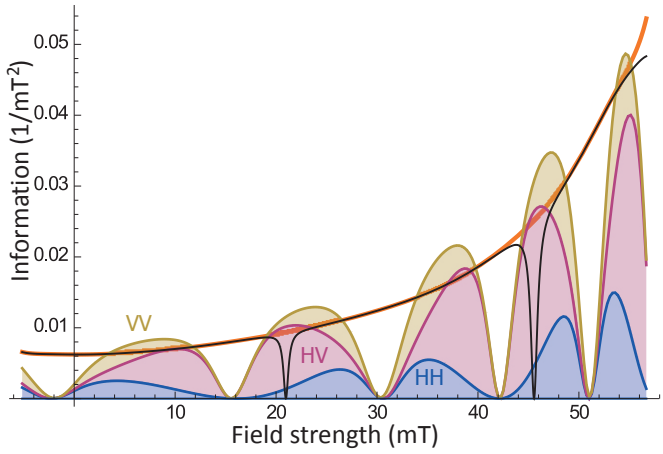

Figure 5.9: Fisher information per input photon in the magnetometer. Thin black curve shows FI for non-entangled photons of an arbitrary linear polarization. Thick orange curve shows the "standard quantum limit," the largest FI obtainable with non-entangled states. Solid regions indicate contributions of HH, HV, and VV outcomes to the NOON-state FI, calculated using $\hat{\rho}$ from Fig. 5.8.

counts. The orange line shows the "standard quantum limit", the largest FI obtainable with the ideally polarized non-entangled state. The black line shows the largest FI for an input state of linear polarization.

Over a large range of field strengths, the NOON state outperforms the best non-entangled two-photon state with up to $(30 \pm 5)\%$ more information. In general, the FI is increasing for larger fields. This is due to the line shift that leads to a faster polarization rotation and therefore to a steeper slope of the coincidence data.

The colored regions show several maxima and minima of Fisher information. Since the FI is related to the derivative of the coincidence function of Fig. 5.7, the FI is at a minimum for the extreme points of the coincidence curves. The maxima of FI are not in the middle between a minimum and a maximum of the coincidence counts, but closer to the minima, because at these points the derivative as well as the relative change are large. This explains the different field strengths of the maxima, e.g., for HH and HV coincidences. Similarly, phase values exist, for which the single-photon curve shows a minimum. This minimum (and also the one of the coincidences) depends on the input polarization and a possible

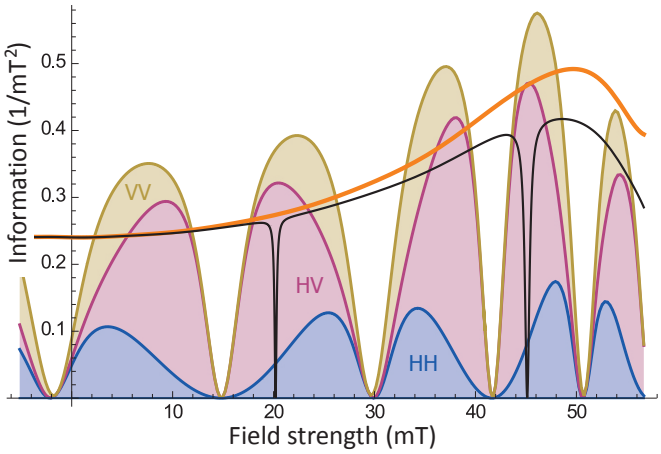

Figure 5.10: Fisher information per depolarization of the ensemble. Labeling as in 5.9.

offset magnetic field. In a real phase estimation, it can be chosen to lie at a convenient phase, i.e., far away from the phase of interest. In Fig. 5.9, this phase has been set arbitrarily (not connected to the phase of V single detections in Fig. 5.7).

Another interesting way of quantifying the information gain with NOON states is by calculating the FI taking into account losses in the sample. We precisely quantify damage to the ^{85}Rb ensemble by computing the number of scattered photons, given by $\mathrm{Tr}\{\hat{\rho}\hat{\Pi}_{\mathrm{dep}}\}$, where $\hat{\Pi}_{\mathrm{dep}} \equiv \mathrm{diag}(s_{++}, s_{+-}, s_{-+}, s_{--})$ in the $\sigma_\pm$ basis and the mean number of scattering events is $s_{ab} \equiv 1 - |t_a^{(85)}|^2 + 1 - |t_b^{(85)}|^2$, where $t_\pm^{(85)}$ is the ^{85}Rb contribution to $t_\pm$. In the same way as above, we can compare FI per scattering, shown in Fig. 5.10. We find the NOON state has an advantage of 1.23 ± 0.04 relative to the best possible single-photon state (the SQL). The difference between black and orange curve is larger for the FI per depolarization, because the photon is partially absorbed in the cell in a polarization-selective way.

The FI per depolarization is decreasing for field values above 50 mT, because of the stronger absorption due to the shift of the ^{85}Rb line. Only at these field strengths, where absorption starts to become important, does the metrological advantage of the NOON state decline relative to the single photon. Thomas-Peter *et al.* [135] note that NOON states are more loss-sensitive than single-photon states, and derive visibility thresholds in a constant-loss model. Here it is important to distinguish between intrin-

sic losses, i.e., those due to the ensemble itself, and extrinsic losses such as imperfect detector efficiency, which can in principle be reduced to arbitrarily low levels. Intrinsic losses are included in the FI calculated above, and because they are field-dependent, provide some information about B, offsetting the loss of FI due to non-arrival of pairs. Extrinsic losses reduce the NOON FI by η_{ex}^2 versus η_{ex} for any single-photon state. Current technology can achieve extrinsic efficiency of $\eta_{\mathrm{ex}} = \eta_{\mathrm{det}}\eta_{\mathrm{path}}$, with detector efficiency $\eta_{\mathrm{det}} = 0.95$ [136] and source-to-detector path efficiency (including escape from the source cavity) $\eta_{\mathrm{path}} = 0.984$ [137]. The achievable advantage, given current technology, is thus 1.21 ± 0.05 per sent photon and 1.15 ± 0.04 per scattered photon.

Part II

Continuous-variable regime

Physicists use the particle theory on Mondays, Wednesdays and Fridays, and the wave theory on Tuesdays, Thursdays and Saturdays.

– William H. Bragg

6

Squeezed-light atomic magnetometry

Apart from single-photon and NOON states in the discrete-variable regime, also quantum states in the continuous-variable regime can be employed for quantum metrology. As the squeezed state shows reduced noise compared to a coherent state, injecting squeezed light into the open input port of an interferometer leads to an increase in signal-to-noise ratio of the measurement. This chapter describes the generation, characterization and the application of polarization-squeezed states of light. Squeezed vacuum states are produced in an optical parametric oscillator and used as probe beam in an atomic magnetometer.

6.1 Introduction

The previous chapters described the design and implementation of a source of atom-resonant NOON states and their application in an atomic magnetometer scheme, in which the shot-noise limit is surpassed. As explained in Section 2.4, in addition to NOON states, also squeezed states can give an advantage in phase estimation. While with NOON states it is easier to come close to the Heisenberg scaling, i.e., to achieve the most information per photon, squeezed states can provide more overall information as they usually contain a macroscopic amount of photons. Recent exper-

iments, the production of squeezed states in the few-photon regime [138] and of squeezed light from a single atom [139] as well as the generation of "photon-added" and "photon-subtracted" states [140, 141] show the deep connection between both kinds of non-classical light.

One motivation in the first proposals of squeezed light was to apply squeezing to shot-noise-limited instruments [55]. To date, the application of squeezed light has been demonstrated in polarization interferometry [80], Mach-Zehnder interferometry [142], atomic spectroscopy [143], atomic spin measurements [81] and in gravitational wave detection [144, 145]. Other shot-noise-limited applications that can benefit from squeezed light are absorption spectroscopy [146], laser gyroscopes [147], and atomic magnetometers.

The sensitivity of atomic magnetometers is fundamentally limited by two distinct sources of quantum noise: the projection noise of the atomic ensemble and the optical shot noise of the probe beam [148, 149, 8, 22]. As atomic magnetometers approach the standard quantum noise limits, it becomes crucial to understand and overcome these limits [131, 148, 150]. For magnetometers based on Faraday rotation and optimized for sensitivity, contributions from projection noise and light shot noise are comparable [148, 19], and simultaneous reduction of both sources is advantageous. A pair of techniques for reducing these fundamental noise sources has been proposed, spin squeezing of the atomic ensemble [151, 152] and polarization squeezing of the probe light [153, 148], with potential to reduce the noise to the Heisenberg limit [22], except in the long-time regime where spin relaxation is limiting [148]. Recent experiments have demonstrated spin squeezing using optical quantum non-demolition (QND) measurements [154, 155, 156] or controlled atomic interactions [157, 158]. While the application of spin squeezing in magnetometry has been shown [150], the proof-of-principle experiment presented in this chapter aims at the reduction of the other fundamental noise source in optical magnetometry, the shot noise of light. The results shown in this chapter were published in [159]. The following section presents the magnetometer's mode of operation in comparison with other highly-sensitive magnetometers.

6.2 Mode of operation

The heart of the magnetometer used in our experiment is an atomic vapor cell that contains rubidium atoms at room temperature. By the Faraday

effect, an axial magnetic field creates a circular birefringence in the vapor. The resulting rotation of the polarization plane of a linearly polarized input beam is seen in the detected signal. This rotation is described in terms of the probe beam Stokes parameters (see Section 2.4.2). The detected signal is

$$S_y^{(\mathrm{out})} = S_y^{(\mathrm{in})} + S_x(\mathcal{V}B_z + \alpha F_z)l \ , \tag{6.1}$$

where $\mathcal{V}$ is the Verdet constant of the vapor, $\mathbf{B}$ is the magnetic field, α is proportional to the vector component of the atomic polarizability, $\mathbf{F}$ is the collective atomic spin, and l is the length of the medium. For a horizontally polarized probe beam, $\langle S_x \rangle$ is maximal and $\langle S_y^{(\mathrm{in})} \rangle$ is zero. The magnetometer signal comes from the terms $\mathcal{V}B_z$ and αF_z, the latter being sensitive to field-induced spin precession. Projection noise is present in F_z, while shot noise is present in $S_y^{(\mathrm{in})}$. We work in a regime where these fundamental noise sources are dominant to show clearly the advantage of squeezed light for optical magnetometry.

6.2.1 Paramagnetic Faraday effect operation

In one usual mode of operation, based on the paramagnetic Faraday effect (see Section 2.5), a magnetometer operates via precession of a polarized spin. The initial polarization rotates into the z direction in response to the field, e.g., from x toward z due to B_y as $\langle F_z \rangle = |F|\mu_0 g B_y \tau$, where g is the Landé factor, μ_0 is the Bohr magneton, and τ is the precession time [19]. This gives a gain due to precession of $G_y \equiv \partial S_y^{(\mathrm{out})}/\partial B_y = S_x \alpha \mu_0 g \tau |F| l$. Technical noise sources, e.g., in the initial orientation of $\mathbf{F}$, and environmental noise in $\mathbf{B}$ contribute to $\mathrm{var}(S_y)$ as G_y^2, i.e., as $|F|^2$. Similarly, $G_z \equiv \partial S_y^{(\mathrm{out})}/\partial B_z = S_x \mathcal{V} l$, with associated technical noise.

6.2.2 Normal Faraday effect operation

While important progress has been made toward reducing technical and environmental noise below the quantum noise [19, 150], this is far from trivial and we adopt the simpler strategy of reducing the gain by reducing $|F|$. We work with an unpolarized ensemble, i.e., a thermal distribution within the hyperfine and Zeeman levels, with $\langle \mathbf{F} \rangle = 0$. G_y, the gain due to precession and the associated technical noise are then zero, while G_z remains and we operate in the Faraday rotation mode.

The fundamental noise sources are largely unchanged in this mode of operation, and we can demonstrate shot-noise-limited performance under conditions that would be present in a highly-sensitive magnetometer with greatly reduced technical noise. The thermal distribution has an intrinsic spin noise of $\mathrm{var}(F_z) = F(F+1)N_A/3$, compared to $\mathrm{var}(F_z) = |F|/2 = FN_A/2$ for an ideal polarized state [8]. In the experiment below, the light is tuned close to the transitions from the $F = 2$ manifold of the D_1 line of ^{87}Rb, which contains $5N_A/8$ atoms and for which $F(F+1)/3 = 2$. The resulting spin noise detected via the last term in Eq. (6.1) is $\approx 5N_A/4$, versus $\approx N_A$ for a fully polarized $F = 2$ ensemble. The shot-noise contribution is unchanged. In this way, we can see the full effects of fundamental noise sources, but with a greatly reduced sensitivity.

6.2.3 Alignment-to-orientation conversion

Even when no additional optical pumping is applied and the atomic system is operated in the normal Faraday effect mode, polarization properties of the atomic ensemble can play an important role. The probe beam itself can lead to a non-negligible optical pumping of the atoms. This regime in which the Faraday rotation angle shows a nonlinear dependence on the optical probe power, is called nonlinear magneto-optical rotation (NMOR) and is explained in detail in [88].

Although in the presented experiment a relatively weak probe beam is used, that is composed of the local oscillator beam and the negligible power of the squeezed vacuum, the intensity of the beam is strong enough to provoke nonlinear effects. In the following, we consider a situation in which a magnetic field is applied along the axis of beam propagation.

When the average time interval between two optical pumping events of an atom becomes comparable to the relaxation time of ground state coherences, which is the case in our experiment, an effect called alignment-to-orientation conversion (AOC) becomes relevant [160, 88]. AOC is caused by the optical electric effect in the presence of an external magnetic field [161].

Orientation in this context refers to the polarization of an atomic ensemble, i.e., a population imbalance of Zeeman substates m_F and $-m_F$ [160]. It can also be described as the first (dipole) polarization moment [162] and can be detected by monitoring a difference in the absorption of right- and left-circularly polarized light.

In contrast, an atomic system is called aligned if the population in a

Zeeman substate depends on the absolute value of m_F [160]. Alignment corresponds to the second (quadrupole) polarization moment [162] and can be produced by optical pumping, but also by any anisotropic interaction such as collisional excitations [160].

In our experiment, the probe beam optically pumps the atoms, which leads to alignment. When the atomic alignment axis undergoes Larmor spin precession around the direction of an applied magnetic field, the population is redistributed, which leads to orientation of the atomic ground state [163]. In effect, the probe beam intensity influences the atomic polarization state, which acts back on the light state leading to a nonlinear rotation of the optical polarization plane.

6.3 Experimental setup

The experimental setup is based on an optical parametric oscillator (OPO) designed for squeezing experiments, which was built by A. Predojević and coworkers and is presented in [164, 110]. The cavity-enhanced SPDC setup described in Chapter 3 and this OPO have very similar cavity designs. The main differences are the following: The PPKTP crystal of the OPO is phase-matched for type-I SPDC, i.e., this setup achieves double-resonance without an additional compensation crystal. Another important difference is that the OPO is pumped at a higher power of 42 mW and therefore closer to threshold.

The experimental setup is shown schematically in Fig. 6.1. As principal light source we use an external-cavity diode laser at 794.7 nm, tunable over the D_1 transition of atomic rubidium. The frequency can be stabilized by FM saturated absorption spectroscopy to individual transitions of the D_1 line of Rb. The laser output passes through a tapered amplifier and is split in two parts: The weaker part is spatially filtered with a single-mode fiber and serves as local oscillator (LO) beam. The stronger part is frequency doubled to 397.4 nm and then sent through a single-mode fiber for mode-cleaning. After the fiber, a power of 42 mW is used to pump a sub-threshold OPO in which squeezed vacuum is produced. The nonlinear medium in the OPO is a type-I phase-matched PPKTP crystal with a length of 1 cm. In contrast to the design presented in [164, 110], the active cavity lock was improved and a quantum noise lock of the phase between LO and squeezed vacuum was implemented.

The homodyne detection system is not as sensitive to scattered locking

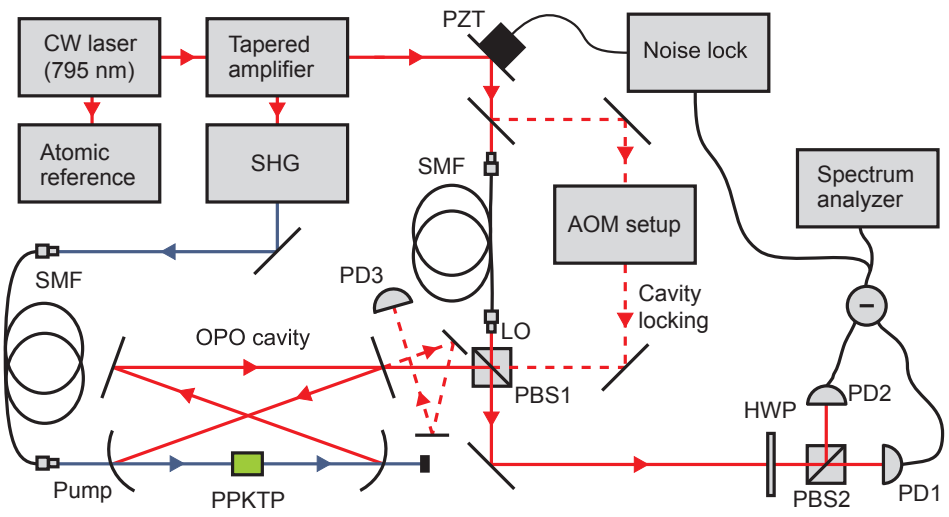

Figure 6.1: Atom-resonant polarization-squeezed light setup. SHG, second harmonic generation; OPO, optical parametric oscillator; PPKTP, phase-matched nonlinear crystal; LO, local oscillator beam; PBS, polarizing beam splitter; AOM, acousto optical modulator; PZT, piezo-electric transducer; HWP, half-wave plate; SMF, single-mode fiber; PD, photodiode.

light that reaches the detectors as in the case of single-photon detection. For this reason, the experiment is performed without alternating between locking and detection periods, i.e., without a mechanical chopper. To reduce the amount of locking light in the detection, it is sent counter-propagating to the squeezed light into the cavity. It is possible to perform measurements with this setup, but the additional noise decreases the quality of the measured squeezing.

In the improved setup, a locking beam polarized orthogonally to the squeezed light was injected. In this way, a separation of residual locking light and squeezing takes place at PBS1 after the OPO cavity (Fig. 6.1). Due to the birefringence in the PPKTP crystal, beams of horizontal and vertical polarization show different resonance frequencies in the cavity. To achieve double-resonance, the horizontally polarized locking beam is frequency-shifted by about 150 MHz by an acousto optical modulator (AOM).

The vertically-polarized cavity output is combined with the horizontally-polarized LO at a polarizing beam splitter (PBS1) with a degree of overlap of 99%. The resulting light is horizontally polarized, with squeezed fluc-

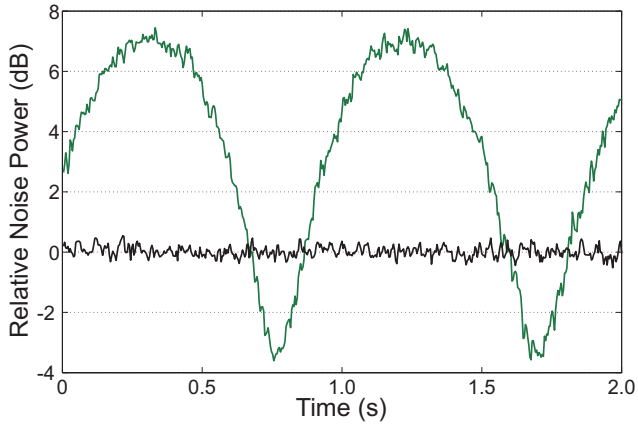

Figure 6.2: Phase-dependent polarization squeezing. Polarization noise power as the phase of the local oscillator is scanned. Center frequency 1 MHz, zero-span mode, RBW=30 kHz, VBW=30 Hz. Horizontal trace shows noise with a polarized (but not squeezed) probe, i.e., with OPO off, and is taken as the reference 0 dB. The oscillating trace shows noise with OPO on, including regions below the shot-noise level.

tuations in the diagonal or circular polarization basis. The squeezing is detected by a balanced detection setup: after a half-wave plate at 22.5°, a polarizing beam splitter (PBS2) splits the horizontally and vertically polarized components of the beam and directs them to two photodiodes of a balanced amplified photo-detector that shows a quantum efficiency of 95%. The signal is then monitored on a spectrum analyzer.

6.4 Polarization squeezing

First, the polarization squeezing is characterized in terms of noise level. The polarization noise is detected with the spectrum analyzer, as the LO phase is scanned with a piezo-electric actuator, giving rise to the squeezing trace shown in Fig. 6.2. The electronic noise is more than 13 dB below the shot-noise level for all phase angles and is subtracted from data. The minimum of the noise level in the squeezed phase is -3.6 dB below the shot-noise level and the maximum 7.4 dB above shot noise in the anti-squeezed phase.

This measurement was performed at a central frequency of 1 MHz with zero span and a resolution bandwidth of 30 kHz, a video bandwidth of 30 Hz and a sweep time of 2 s. The total detection efficiency after cre-

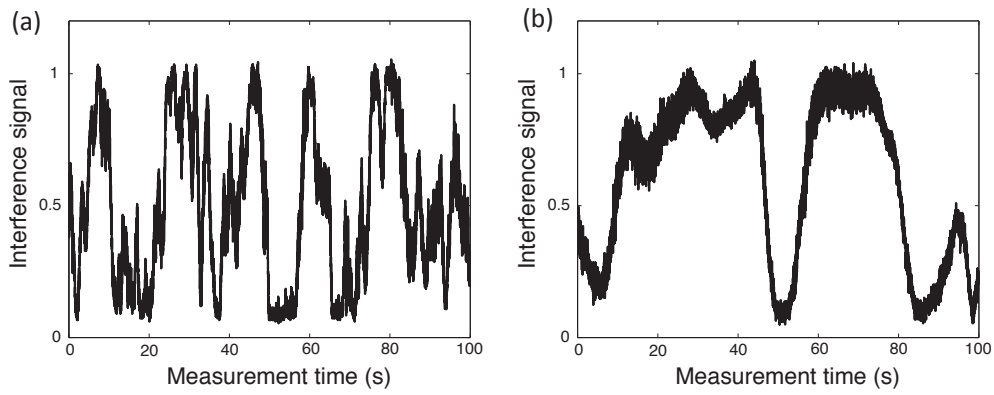

Figure 6.3: Passive optical phase stability. Interference signal between LO arm and SHG-OPO arm over a period of 100 seconds (a) before and (b) after the improvement of the passive phase stability of the paths.

ation is 82% and includes the escape efficiency (96%), the homodyne efficiency (98%), transmission through the atomic cell (97%) and the optical elements (95%), and the quantum efficiency of the detector (95%). The parametric gain, defined here as the ratio between the maximum transmission of a classical beam through the cavity with and without the presence of the copropagating pump beam, was measured to be 4.8.

While the degree of squeezing is one of the highest obtained in a diode-laser-pumped system, it could be further improved by, e.g., a longer nonlinear crystal, a higher finesse of the cavity, a higher escape efficiency of the cavity or lower losses between the cavity and the detection. A higher finesse could be achieved by a better AR coating of the crystal endfaces or by a monolithic cavity design [165].

6.4.1 Phase stability

In Fig. 6.2 the phase between LO and squeezed vacuum is scanned by applying an oscillating voltage to a piezo-electric transducer, while the central frequency of the spectrum analyzer is fixed. For the magnetometry application, a fixed phase at the maximum squeezing level has to be guaranteed.

As a first step, we increased the passive stability of the interferometer formed by the LO arm and the SHG-OPO-arm (Fig. 6.1). The interference signal was monitored over time. Fig. 6.3.(a) shows the signal fluctuations over a period of 100 seconds. To improve the passive stability that was lim-

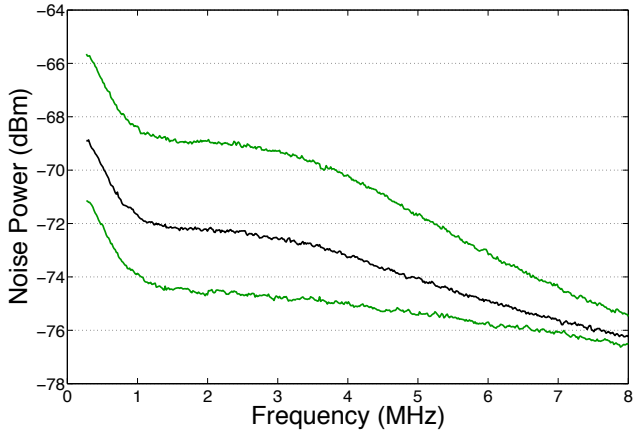

Figure 6.4: Squeezing spectrum. The black trace shows the shot-noise limit, while the upper green trace shows the anti-squeezed noise level and the lower green trace the squeezed noise level.

ited mostly by temperature fluctuations in the optical single-mode fibers, the temperature stability of the whole setup was increased by reducing the air flow on the optical table with curtains. In addition, the optical fibers were fixed on the optical table in a way that reduces mechanical stress. The improved stability is shown in Fig. 6.3.(b).

To actively stabilize the phase between LO and squeezed vacuum at the level of maximum squeezing or maximum anti-squeezing, a quantum noise lock was implemented [166]. The difference signal of the balanced detector is used as input signal in a FM spectroscopy locking scheme.

Fig. 6.4 shows the squeezing and anti-squeezing levels as a function of the central frequency of the spectrum analyzer. The lower degree of squeezing compared to Fig. 6.2 stems from a lower optical pump power of the OPO.

6.5 Magnetometry

After the characterization measurements, the polarization-squeezed light is used as probe beam in an atomic magnetometer setup.

It should be noted that, as opposed to the single-photon regime operation, for squeezing the requirement of narrow bandwidth is easier to fulfill as the narrowband LO beam selects a narrowband portion of the squeezed cavity spectrum.

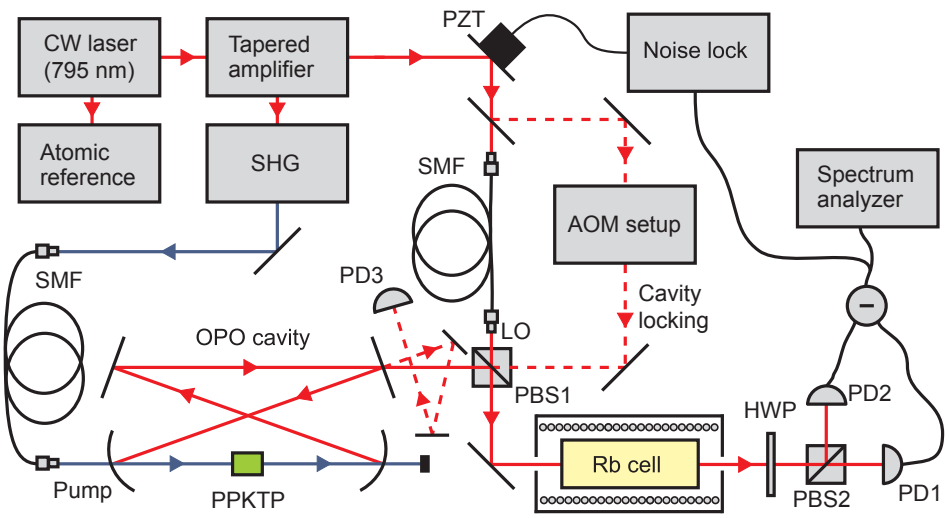

Figure 6.5: Squeezed-light magnetometry setup. Rb cell, rubidium vapor cell with magnetic coil and magnetic shielding; SHG, second harmonic generation; OPO, optical parametric oscillator; PPKTP, phase-matched nonlinear crystal; LO, local oscillator beam; PBS, polarizing beam splitter; AOM, acousto optical modulator; PZT, piezo-electric transducer; HWP, half-wave plate; SMF, single-mode fiber; PD, photodiode.

6.5.1 Magnetometry setup

The magnetometer consists of a 15 cm-long atomic vapor cell at room temperature that is placed between PBS1 and the detection setup (Fig. 6.5). The isotopically purified atomic vapor contains >99% ^{87}Rb with a small concentration of ^{85}Rb. The cell is contained within a single-layer μ-metal cylinder to shield external magnetic fields while a coil within the cylinder generates the desired field B_z.

We lock the laser to the $5^2S_{1/2}(F{=}3){\rightarrow}5^2P_{1/2}(F'{=}2)$ transition of the D_1 line of ^{85}Rb. This corresponds to a detuning of about 700 MHz from the closest ^{87}Rb resonance. The LO beam has a power of 620 μW and a beam waist of 950 μm inside the vapor cell. For this intensity, beam shape, and detuning, the magnetometer operates in a regime of nonlinear magneto-optical rotation (NMOR) [19]. A small fraction of the atoms are optically pumped while passing through the linearly-polarized probe beam, creating coherences within the $F = 2$ manifold. Rotation of these coherences by the z-polarized magnetic field creates the conditions for alignment-to-orientation conversion [161, 88, 167], again by the probe beam. Measurements of rotation angle versus input power show a

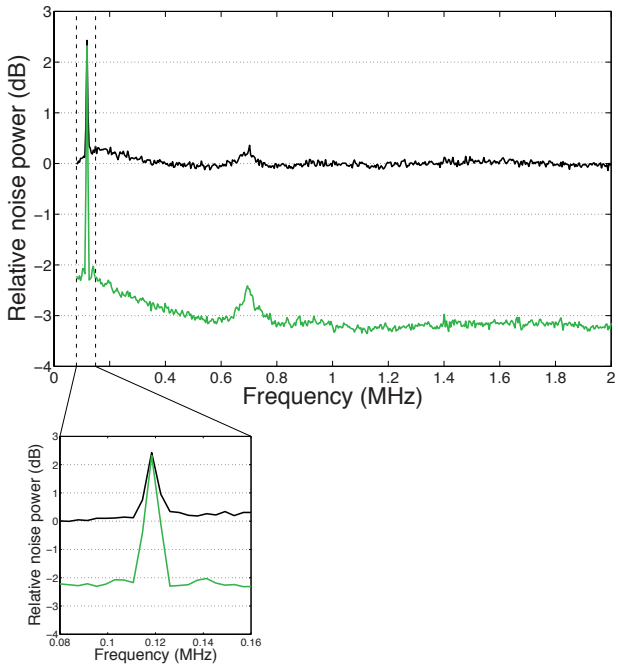

Figure 6.6: Faraday rotation measurement. Power of the polarization signal as center frequency is scanned, RBW=3 kHz, VBW=30 Hz. The (upper) black curve shows the applied magnetic signal at 120 kHz above the shot-noise background of a polarized (but not squeezed) probe. The (lower) green line depicts the same signal with polarization-squeezing. A zoomed view around the calibration peak at 120 kHz is shown.

quadratic scaling consistent with this nonlinear mechanism. Unlike optical self-rotation [168, 169], this nonlinearity does not strongly couple optical noise into S_y, so long as the rotation angle remains small.

6.5.2 Sensitivity measurements

To measure the magnetometric sensitivity, we observe the Faraday rotation signal in response to an applied sinusoidal magnetic field at a frequency of 120 kHz. The sensitivity is measured with two different input polarization states: a coherent polarization state (OPO off) and a state squeezed in S_y. Quantum noise locking is used to stabilize the LO phase during the measurements. In both cases the average polarization is horizontal, due to the strong LO contribution, but the quantum fluctuations differ. As shown in Fig. 6.6, the observed power spectrum in both cases

shows the reference signal due to the applied oscillating magnetic field at 120 kHz above differing noise backgrounds.

The rotation angle was calculated to be $\phi = (I_1 - I_2)/(I_1 + I_2) = 1.2\,\mu\text{rad}$, where $I_{1,2}$ are the beam intensities at the two detectors. The spectrum analyzer frequency is scanned from 80 kHz to 2 MHz, in a sweep time of 8 s. The resolution bandwidth and the video bandwidth were set to 3 kHz and 30 Hz, respectively and the signal was averaged over 130 cycles.

The polarimeter signal was calibrated against a linear magnetic field sensor inserted within the coil and shielding, thus permitting a direct conversion from measured voltage to axial magnetic field B_z. The sensitivity, i.e., field noise density as measured with the spectrum analyzer, is 4.6×10^{-8} T/$\sqrt{\text{Hz}}$ for a polarized input, and reduced by 3.2 dB to 3.2×10^{-8} T/$\sqrt{\text{Hz}}$ with a polarization-squeezed input.

It should be noted that the squeezing extends over >2 MHz of bandwidth, allowing magnetic field measurements in the μs-regime with squeezing-enhanced sensitivity. This technique is thus also suitable to improve μs-scale QND measurements [8]. Additionally, the light source could find application in the storage and retrieval of squeezing in atomic ensembles [170, 171].

As for the future, your task is not to foresee it, but to enable it.

– Antoine de Saint-Exupéry

7

Conclusions

7.1 Summary

The work presented in this thesis contributes to the quest to develop atom-resonant quantum light sources and apply them to light-matter interaction for the use in fundamental research as well as in quantum technologies.

First, a cavity-enhanced SPDC setup was designed and built. The use of cavity enhancement allowed for ultra-bright generation of photon pairs. The *detected* coincidence rate is 1.7×10^5 photon pairs per second per mW of pump power, one of the highest brightnesses of indistinguishable photon pairs. The cavity shows a good passive stability and is additionally actively locked to a CW diode laser. The laser itself is locked to a rubidium transition, which guarantees atom-resonance of the central frequency-degenerate down-conversion mode. This is an advantage over other implementations, in which the cavity is not locked at all [33] or locked to the pump wavelength [34, 172]. Without any spectral or spatial filtering the cavity output shows a HOM visibility of 96%. This proves the high indistinguishability of two photons of a pair, a crucial requirement for the generation of high-fidelity NOON states in quantum metrology [10] and for the use in linear optical quantum computation (LOQC) proposals [23]. The thorough characterization of the photon pair state included a

full quantum state tomography of the polarization degree of freedom.

The cavity output was converted into a polarization NOON state in the H/V basis. The most important metrological property of NOON states, phase super-resolution, was demonstrated with high visibility. Furthermore, the polarization density matrix of the NOON state was reconstructed showing a fidelity of 99% with an ideal NOON state.

As the cavity output consists of many frequency modes, the output is not directly atom-compatible. To select the rubidium resonant mode, a very narrowband filter had to be used. Instead of consecutive filter cavities [99, 172, 95], we used a novel atomic-based filter, which guarantees a very robust and intrinsically atom-resonant operation. The filter achieves a transmission efficiency of up to 20% with a theoretical maximum transmission of 25%.

After a successful demonstration of its performance with classical probe light [118], the filter was used to select the rubidium-resonant mode of the cavity-enhanced SPDC process. To efficiently block all other cavity frequency modes, a high out-of-band rejection is crucial. This filter achieves a high extinction ratio of >35 dB over the whole phase-matching bandwidth of the SPDC process. The ultra-high coincidence count rate enables filtering of both photons of a pair, as opposed to many previous experiments, in which only one arm was filtered [99, 172, 95]. More than 94% of the photons are resonant to a rubidium transition frequency with a single-photon bandwidth of 4.5 MHz, which makes it the first SPDC single-photon source that has demonstrated atom-resonance of more than a small fraction of its output.

Since the SPDC process is based on type-II phase-matching, the filtered photon pairs can be split deterministically by their orthogonal polarization on a polarizing beam splitter. The detection of one photon of a pair heralds the presence of the other photon in a state that is a good approximation of a single-photon Fock state. The figures of merit of a heralded single-photon source, cross-correlation and auto-correlation functions were measured and a value of the cross-correlation function of the signal photon of $g_c^{(2)}(0) \leqslant 0.040 \pm 0.012$ was measured, 80 standard deviation below the classical limit of 1.

Finally, the filtered photon pairs were used as NOON state input in an atomic magnetometer. The NOON states probe the applied magnetic field with super-resolution of high visibility. The experimental results were carefully analyzed in terms of Fisher information. The super-resolution translates into a phase super-sensitivity as the Fisher information per

photon pair surpasses the classical limit by up to 30%. This constitutes the first controlled interaction between an entangled photon pair and atoms.

In addition to the previously discussed quantum states in the discrete-variable regime, the thesis also reports on the generation, characterization and application of quantum states of light in the continuous-variable regime. An existing optical parametric oscillator setup was improved and produced atom-resonant polarization-squeezed light with a degree of squeezing of -3.6 dB. Initially, measurements were performed while scanning the phase between squeezed vacuum and local oscillator beam. Subsequently, a quantum noise lock was implemented to lock the phase between the local oscillator beam and the squeezed vacuum beam to the maximally squeezed or anti-squeezed phase, respectively.

The application of these states in a magnetometry setup was investigated. Atomic magnetometers are fundamentally limited by two kinds of noise sources: atomic projection noise and shot noise of light [19]. While some experiments so far aimed at the reduction of the projection noise of atoms and obtained spin squeezing of the atomic spin [154, 155, 156, 150], our goal was to reduce the light noise in a magnetometry measurement below the standard quantum limit. A shot-noise-limited atomic magnetometry setup was built and characterized with classical light input. The application of the polarization-squeezed light improved the measurement by 3.2 dB below the SQL.

7.2 Outlook

There are several possible directions in which the existing setup could be developed.

One line of applications could be the combination with an atomic dipole trap setup of about 10^6 cold rubidium atoms that was built in our group and is so far mainly used for quantum non-demolition (QND) measurements [89], spin squeezing measurements [8, 173] and nonlinear magnetometry [174]. The NOON state setup is already fiber-coupled and could easily be connected to the trap setup. Measurements with cold atomic ensembles would allow for longer coherence times and higher optical depths. The squeezing setup is not fiber-coupled because the inevitable fiber-coupling losses would decrease the amount of squeezing. For this reason, the setup is mounted on a breadboard that could be moved as a whole to the laboratory of the atomic trap. This would open the possibility to demonstrate

an atomic magnetometer which shows at the same time reduction below both fundamental limits, atomic projection noise and light shot noise.

Another possible direction of applications includes further measurements in hot atomic vapors. One example is the study of stimulated emission processes of a photon by an atom. This fundamental process is difficult to study, because it requires an atom-resonant deterministic or heralded single-photon source. The presented single-photon source would enable such an experiment.

Certain improvements could be made to the setup to increase the coincidence rate further. The current design of the atomic-based filter is based on the paramagnetic Faraday effect, which sets the maximum efficiency to 25%. A new filter design was developed and tested in our group that is based on the normal Faraday effect and has no limitation on the maximum efficiency. So far, 71% transmission could be demonstrated [175]. This would increase the coincidence rate by one order of magnitude. Another mean to increase the coincidence rate would be the use of a longer nonlinear crystal. PPKTP crystals are now available at longer lengths that could increase the production rate of the SPDC process.

In a more general context, the presented techniques could find application in other quantum metrological schemes. While the scalability of the number of photons in a NOON state remains an issue, progress has been made recently toward a scalable approach [15]. Also, the development of robust and high-efficient quantum memories could enable the generation of larger NOON states. On the other hand, already high-brightness 2-NOON states will be useful in further proof-of-principle experiments of ghost imaging [176] or quantum illumination [177]. The squeezed-light techniques are already sufficiently mature to be used in real devices, such as advanced magnetometers or gravitational wave detectors [178].

An interesting and promising development is the integration of optical setups into tiny devices. Magnetometers smaller than the size of a grain of rice have been implemented [179]. Many hundreds or thousands of these magnetometers could be combined to achieve a high spatial resolution with applications, e.g., in the imaging of the human heart or brain.

While the thesis demonstrates the application in a quantum metrological context, the same sources are also directly applicable to quantum information tasks. These include linear optics quantum computing (LOQC), where indistinguishable photons are the main resource as well as quantum communication, where single photons are exploited as carri-

ers of quantum information over long distances. In a quantum network, single photons could transmit information between stationary nodes implemented by atomic ensembles or single trapped atoms. To distribute the entanglement over distances of many hundreds of kilometers, quantum repeaters will be necessary [180, 181]. A requirement for quantum repeaters is the storage of entanglement or squeezing and therefore high-quality quantum memories [182, 183], possibly based on atomic ensembles [170, 184, 185, 186] or solid state devices [116, 187, 188].

In general, the techniques used in this thesis are very promising candidates for the generation of narrowband atom-resonant single photons, photon pairs, NOON states and quadrature- or polarization-squeezed states. These could find application in a variety of experimental studies of atom-photon interaction at the single-photon level, including interaction with single atoms, hot and cold atomic ensembles, solid-state devices and Bose-Einstein condensates. The ability to generate photonic quantum states compatible with atomic resonances will possibly enable advances in many fields of optical science including future applications in fundamental research and applied technology that are yet to be explored.

Work. Finish. Publish.
– Michael Faraday

List of publications

The work presented in this thesis has been the basis of the following publications:

- F. Wolfgramm, X. Xing, A. Cerè, A. Predojević, A. M. Steinberg, and M. W. Mitchell, "Bright filter-free source of indistinguishable photon pairs," Opt. Express **16**, 18145 (2008).

- F. Wolfgramm, A. Cerè, and M. W. Mitchell, "NOON states from cavity-enhanced down-conversion: High quality and super-resolution," J. Opt. Soc. Am. B **27**, A25-A29 (2010).

- F. Wolfgramm, A. Cerè, F. A. Beduini, A. Predojević, M. Koschorreck, and M. W. Mitchell, "Squeezed-Light Optical Magnetometry," Phys. Rev. Lett. **105**, 053601 (2010).

- F. Wolfgramm, Y. A. de Icaza Astiz, F. A. Beduini, A. Cerè, and M. W. Mitchell, "Atom-Resonant Heralded Single Photons by Interaction-Free Measurement," Phys. Rev. Lett. **106**, 053602 (2011).

- F. Wolfgramm, C. Vitelli, F. A. Beduini, N. Godbout, and M. W. Mitchell, "NOON-state probing of a delicate system," submitted.

PLZ, UPS und DPD
BMX, BPM und XTC
EMI, CBS und BMG
ADAC, DLRG - ojemine
– Die fantastischen Vier, *MfG*

List of abbreviations

AOC	Alignment-to-orientation conversion
AOM	Acousto optical modulator
APD	Avalanche photo-diode
AR	Anti-reflection
BEC	Bose-Einstein condensate
BS	Beam splitter
CW	Continuous wave
D	Detector
FR	Faraday rotator
FSR	Free spectral range
FWHM	Full width at half maximum
FWM	Four-wave mixing
GT	Glan-Thompson polarizer
HOM	Hong-Ou-Mandel
HWP	Half-wave plate
IF	Interference filter
IFM	Interaction-free measurement
KLM	Knill, Laflamme, and Milburn
KTP	Potassium titanyl phosphate
LBO	Lithium triborate
LO	Local oscillator
LOQC	Linear optical quantum computing
OD	Optical density
OPO	Optical parametric oscillator
PA	Polarization analyzer

PBS	Polarizing beam splitter
PD	Photodiode
PID	Proportional-integral-differential
PM	Polarization-maintaining
PPKTP	Periodically-poled potassium titanyl phosphate
PZT	Piezo-electric transducer
QND	Quantum non-demolition
QPM	Quasi-phase matching
QWP	Quarter-wave plate
SHG	Second-harmonic generation
SMF	Single-mode fiber
SPDC	Spontaneous parametric down-conversion
SQL	Standard quantum limit
THG	Third-harmonic generation
WP	Wollaston prism

"What is the use of a book," thought Alice, "without pictures or conversations?"

– Lewis Carroll, *Alice's Adventures in Wonderland*

List of figures

There are three stages in scientific discovery: first, people deny that it is true; then they deny that it is important; finally they credit the wrong person.

– Alexander von Humboldt

Bibliography

[1] A. Kuhn, M. Hennrich, and G. Rempe, *Deterministic Single-Photon Source for Distributed Quantum Networking*, Phys. Rev. Lett. **89**(6), 067901 (2002).

[2] J. McKeever, A. Boca, A. D. Boozer, R. Miller, J. R. Buck, A. Kuzmich, and H. J. Kimble, *Deterministic Generation of Single Photons from One Atom Trapped in a Cavity*, Science **303**(5666), 1992 (2004).

[3] M. K. Tey, Z. Chen, S. A. Aljunid, B. Chng, F. Huber, G. Maslennikov, and C. Kurtsiefer, *Strong interaction between light and a single trapped atom without the need for a cavity*, Nature Phys. **4**(12), 924 (2008).

[4] A. Stiebeiner, O. Rehband, R. Garcia-Fernandez, and A. Rauschenbeutel, *Ultra-sensitive fluorescence spectroscopy of isolated surface-adsorbed molecules using an optical nanofiber*, Opt. Express **17**(24), 21704 (2009).

[5] M. Pototschnig, Y. Chassagneux, J. Hwang, G. Zumofen, A. Renn, and V. Sandoghdar, *Controlling the Phase of a Light Beam with a Single Molecule*, Phys. Rev. Lett. **107**(6), 063001 (2011).

[6] K. Eckert, O. Romero-Isart, M. Rodriguez, M. Lewenstein, E. S. Polzik, and A. Sanpera, *Quantum non-demolition detection of strongly correlated systems*, Nature Phys. **4**(1), 50 (2008).

[7] T. Roscilde, M. Rodriguez, K. Eckert, O. Romero-Isart, M. Lewenstein, E. Polzik, and A. Sanpera, *Quantum polarization spectroscopy of correlations in attractive fermionic gases*, New J. Phys. **11**(5), 055041 (2009).

[8] M. Koschorreck, M. Napolitano, B. Dubost, and M. W. Mitchell, *Sub-Projection-Noise Sensitivity in Broadband Atomic Magnetometry*, Phys. Rev. Lett. **104**(9), 093602 (2010).

[9] P. M. Carlton, J. Boulanger, C. Kervrann, J.-B. Sibarita, J. Salamero, S. Gordon-Messer, D. Bressan, J. E. Haber, S. Haase, L. Shao, *et al.*, *Fast live simultaneous multiwavelength four-dimensional optical microscopy*, Proc. Natl. Acad. Sci. **107**, 16016 (2010).

[10] J. P. Dowling, *Quantum optical metrology - the lowdown on high-N00N states*, Contemp. Phys. **49**(2), 125 (2008).

[11] A. Kuzmich and L. Mandel, *Sub-shot-noise interferometric measurements with two-photon states*, Quantum Semiclass. Opt. **10**(3), 493 (1998).

[12] E. J. S. Fonseca, C. H. Monken, and S. Pádua, *Measurement of the de Broglie Wavelength of a Multiphoton Wave Packet*, Phys. Rev. Lett. **82**(14), 2868 (1999).

[13] Z. Y. Ou, X. Y. Zou, L. J. Wang, and L. Mandel, *Experiment on nonclassical fourth-order interference*, Phys. Rev. A **42**(5), 2957 (1990).

[14] M. W. Mitchell, J. S. Lundeen, and A. M. Steinberg, *Super-resolving phase measurements with a multiphoton entangled state*, Nature **429**(6988), 161 (2004).

[15] I. Afek, O. Ambar, and Y. Silberberg, *High-NOON States by Mixing Quantum and Classical Light*, Science **328**(5980), 879 (2010).

[16] P. Walther, J.-W. Pan, M. Aspelmeyer, R. Ursin, S. Gasparoni, and A. Zeilinger, *De Broglie wavelength of a non-local four-photon state*, Nature **429**(6988), 158 (2004).

[17] Z. Y. Ou and Y. J. Lu, *Cavity Enhanced Spontaneous Parametric Down-Conversion for the Prolongation of Correlation Time between Conjugate Photons*, Phys. Rev. Lett. **83**(13), 2556 (1999).

[18] Y. J. Lu and Z. Y. Ou, *Optical parametric oscillator far below threshold: Experiment versus theory*, Phys. Rev. A **62**(3), 033804 (2000).

[19] D. Budker and M. Romalis, *Optical magnetometry*, Nature Phys. **3**(4), 227 (2007).

[20] H. Xia, A. B. Baranga, D. Hoffman, and M. V. Romalis, *Magnetoencephalography with an atomic magnetometer*, Appl. Phys. Lett. **89**(21), 211104 (2006).

[21] H. B. Dang, A. C. Maloof, and M. V. Romalis, *Ultrahigh sensitivity magnetic field and magnetization measurements with an atomic magnetometer*, Appl. Phys. Lett. **97**(15), 151110 (2010).

[22] V. Shah, G. Vasilakis, and M. V. Romalis, *High Bandwidth Atomic Magnetometery with Continuous Quantum Nondemolition Measurements*, Phys. Rev. Lett. **104**(1), 013601 (2010).

[23] E. Knill, R. Laflamme, and G. J. Milburn, *A scheme for efficient quantum computation with linear optics*, Nature **409**(6816), 46 (2001).

[24] A. Fedrizzi, T. Herbst, M. Aspelmeyer, M. Barbieri, T. Jennewein, and A. Zeilinger, *Anti-symmetrization reveals hidden entanglement*, New J. Phys. **11**(10), 103052 (2009).

[25] V. G. Dmitriev, G. G. Gurzadyan, and D. N. Nikogosyan, *Handbook of Nonlinear Optical Crystals* (Springer, 1999).

[26] D. N. Nikogosyan, *Nonlinear Optical Crystals: A Complete Survey* (Springer, 2005).

[27] M. W. Mitchell, *Parametric down-conversion from a wave-equation approach: Geometry and absolute brightness*, Phys. Rev. A **79**(4), 043835 (2009).

[28] A. Fedrizzi, T. Herbst, A. Poppe, T. Jennewein, and A. Zeilinger, *A wavelength-tunable fiber-coupled source of narrowband entangled photons*, Opt. Express **15**(23), 15377 (2007).

[29] G. D. Boyd and D. A. Kleinman, *Parametric Interaction of Focused Gaussian Light Beams*, J. Appl. Phys. **39**(8), 3597 (1968).

[30] M. J. Collett and C. W. Gardiner, *Squeezing of intracavity and traveling-wave light fields produced in parametric amplification*, Phys. Rev. A **30**(3), 1386 (1984).

[31] U. Herzog, M. Scholz, and O. Benson, *Theory of biphoton generation in a single-resonant optical parametric oscillator far below threshold*, Phys. Rev. A **77**(2), 023826 (2008).

[32] C. E. Kuklewicz, *Ultrabright Source of Polarization-Entangled Photons from Cavity-Enhanced Downconversion*, Ph.D. thesis, Massachusetts Institute of Technology (2005).

[33] C. E. Kuklewicz, F. N. C. Wong, and J. H. Shapiro, *Time-Bin-Modulated Biphotons from Cavity-Enhanced Down-Conversion*, Phys. Rev. Lett. **97**(22), 223601, 223601 (2006).

[34] M. Scholz, L. Koch, and O. Benson, *Statistics of Narrow-Band Single Photons for Quantum Memories Generated by Ultrabright Cavity-Enhanced Parametric Down-Conversion*, Phys. Rev. Lett. **102**(6), 063603 (2009).

[35] M. Scholz, *New Light Sources for Quantum Information Processing*, Ph.D. thesis, Humboldt-Universität zu Berlin (2009).

[36] D. F. Walls and G. J. Milburn, *Quantum Optics* (Springer, 1994).

[37] C. K. Hong, Z. Y. Ou, and L. Mandel, *Measurement of subpicosecond time intervals between two photons by interference*, Phys. Rev. Lett. **59**(18), 2044 (1987).

[38] Y. H. Shih and C. O. Alley, *New Type of Einstein-Podolsky-Rosen-Bohm Experiment Using Pairs of Light Quanta Produced by Optical Parametric Down Conversion*, Phys. Rev. Lett. **61**(26), 2921 (1988).

[39] T. B. Pittman, D. V. Strekalov, A. Migdall, M. H. Rubin, A. V. Sergienko, and Y. H. Shih, *Can Two-Photon Interference be Considered the Interference of Two Photons?*, Phys. Rev. Lett. **77**(10), 1917 (1996).

[40] E. Bocquillon, C. Couteau, M. Razavi, R. Laflamme, and G. Weihs, *Coherence measures for heralded single-photon sources*, Phys. Rev. A **79**(3), 035801 (2009).

[41] S. Fasel, O. Alibart, S. Tanzilli, P. Baldi, A. Beveratos, N. Gisin, and H. Zbinden, *High-quality asynchronous heralded single-photon source at telecom wavelength*, New J. Phys. **6**(1), 163 (2004).

[42] P. Grangier, G. Roger, and A. Aspect, *Experimental Evidence for a Photon Anticorrelation Effect on a Beam Splitter: A New Light on Single-Photon Interferences*, Europhys. Lett. **1**(4), 173 (1986).

[43] M. A. Nielsen and I. L. Chuang, *Quantum Computation and Quantum Information* (Cambridge Univ. Press, 2000).

[44] H. Häffner, W. Hansel, C. F. Roos, J. Benhelm, D. Chek-al kar, M. Chwalla, T. Korber, U. D. Rapol, M. Riebe, P. O. Schmidt, *et al.*, *Scalable multiparticle entanglement of trapped ions*, Nature **438**(7068), 643 (2005).

[45] M. Steffen, M. Ansmann, R. C. Bialczak, N. Katz, E. Lucero, R. McDermott, M. Neeley, E. M. Weig, A. N. Cleland, and J. M. Martinis, *Measurement of the Entanglement of Two Superconducting Qubits via State Tomography*, Science **313**(5792), 1423 (2006).

[46] M. Neeley, R. C. Bialczak, M. Lenander, E. Lucero, M. Mariantoni, A. D. O'Connell, D. Sank, H. Wang, M. Weides, J. Wenner, *et al.*, *Generation of three-qubit entangled states using superconducting phase qubits*, Nature **467**(7315), 570 (2010).

[47] L. DiCarlo, M. D. Reed, L. Sun, B. R. Johnson, J. M. Chow, J. M. Gambetta, L. Frunzio, S. M. Girvin, M. H. Devoret, and R. J. Schoelkopf, *Preparation and measurement of three-qubit entanglement in a superconducting circuit*, Nature **467**(7315), 574 (2010).

[48] A. G. White, D. F. V. James, P. H. Eberhard, and P. G. Kwiat, *Nonmaximally Entangled States: Production, Characterization, and Utilization*, Phys. Rev. Lett. **83**(16), 3103 (1999).

[49] D. F. V. James, P. G. Kwiat, W. J. Munro, and A. G. White, *Measurement of qubits*, Phys. Rev. A **64**(5), 052312 (2001).

[50] J. B. Altepeter, D. F. V. James, and P. G. Kwiat, *Quantum State Estimation*, vol. 649 of *Lect. Notes Phys.* (Springer, 2004).

[51] R. B. A. Adamson, *Characterization of Quantum States of Light*, Ph.D. thesis, University of Toronto (2009).

[52] J. Lagarias, J. A. Reeds, M. H. Wright, and P. E. Wright, *Convergence Properties of the Nelder-Mead Simplex Method in Low Dimensions*, SIAM Journal of Optimization **9**, 112 (1998).

[53] R. B. A. Adamson, L. K. Shalm, M. W. Mitchell, and A. M. Steinberg, *Multiparticle State Tomography: Hidden Differences*, Phys. Rev. Lett. **98**(4), 043601 (2007).

[54] R. B. A. Adamson, P. S. Turner, M. W. Mitchell, and A. M. Steinberg, *Detecting hidden differences via permutation symmetries*, Phys. Rev. A **78**(3), 033832 (2008).

[55] C. M. Caves, *Quantum-mechanical noise in an interferometer*, Phys. Rev. D **23**(8), 1693 (1981).

[56] H. Lee, P. Kok, and J. P. Dowling, *A quantum Rosetta stone for interferometry*, J. Mod. Opt. **49**(6816), 2325 (2002).

[57] M. A. Rubin and S. Kaushik, *Loss-induced limits to phase measurement precision with maximally entangled states*, Phys. Rev. A **75**(5), 053805 (2007).

[58] R. Demkowicz-Dobrzański, U. Dorner, B. J. Smith, J. S. Lundeen, W. Wasilewski, K. Banaszek, and I. A. Walmsley, *Quantum phase estimation with lossy interferometers*, Phys. Rev. A **80**(1), 013825 (2009).

[59] U. Dorner, R. Demkowicz-Dobrzanski, B. J. Smith, J. S. Lundeen, W. Wasilewski, K. Banaszek, and I. A. Walmsley, *Optimal Quantum Phase Estimation*, Phys. Rev. Lett. **102**(4), 040403 (2009).

[60] M. Kacprowicz, R. Demkowicz-Dobrzanski, W. Wasilewski, K. Banaszek, and I. A. Walmsley, *Experimental quantum-enhanced estimation of a lossy phase shift*, Nature Phys. **4**(6), 357 (2010).

[61] T. Ono and H. F. Hofmann, *Effects of photon losses on phase estimation near the Heisenberg limit using coherent light and squeezed vacuum*, Phys. Rev. A **81**(3), 033819 (2010).

[62] Z. Y. Ou, *Complementarity and Fundamental Limit in Precision Phase Measurement*, Phys. Rev. Lett. **77**(12), 2352 (1996).

[63] A. S. Lane, S. L. Braunstein, and C. M. Caves, *Maximum-likelihood statistics of multiple quantum phase measurements*, Phys. Rev. A **47**(3), 1667 (1993).

[64] J. G. Rarity, P. R. Tapster, E. Jakeman, T. Larchuk, R. A. Campos, M. C. Teich, and B. E. A. Saleh, *Two-photon interference in a Mach-Zehnder interferometer*, Phys. Rev. Lett. **65**(11), 1348 (1990).

[65] M. J. Holland and K. Burnett, *Interferometric detection of optical phase shifts at the Heisenberg limit*, Phys. Rev. Lett. **71**(9), 1355 (1993).

[66] Z. Y. Ou, *Fundamental quantum limit in precision phase measurement*, Phys. Rev. A **55**(4), 2598 (1997).

[67] M. D'Angelo, M. V. Chekhova, and Y. Shih, *Two-Photon Diffraction and Quantum Lithography*, Phys. Rev. Lett. **87**(1), 013602 (2001).

[68] R. A. Fisher, *Theory of Statistical Estimation*, Proc. Camb. Soc. **22**(05), 700 (1925).

[69] S. L. Braunstein and C. M. Caves, *Statistical distance and the geometry of quantum states*, Phys. Rev. Lett. **72**(22), 3439 (1994).

[70] Z. Hradil and J. Rehácek, *Quantum interference and Fisher information*, Phys. Lett. A **334**(4), 267 (2005).

[71] J. Joo, W. J. Munro, and T. P. Spiller, *Quantum Metrology with Entangled Coherent States*, Phys. Rev. Lett. **107**(8), 083601 (2011).

[72] H. Cramér, *Mathematical Methods of Statistics* (Princeton Univ. Press, 1946).

[73] C. W. Helstrom, *Quantum detection and estimation theory*, J. Stat. Phys. **1**(2), 231 (1969).

[74] N. Korolkova, G. Leuchs, R. Loudon, T. C. Ralph, and C. Silberhorn, *Polarization squeezing and continuous-variable polarization entanglement*, Phys. Rev. A **65**(5), 052306 (2002).

[75] H.-A. Bachor and T. C. Ralph, *A Guide to Experiments in Quantum Optics* (Wiley-VCH Verlag, 2004).

[76] C. C. Gerry and P. L. Knight, *Introductory Quantum Optics* (Cambridge Univ. Press, 2005).

[77] H. P. Yuen, *Two-photon coherent states of the radiation field*, Phys. Rev. A **13**(6), 2226 (1976).

[78] W. P. Bowen, R. Schnabel, H.-A. Bachor, and P. K. Lam, *Polarization Squeezing of Continuous Variable Stokes Parameters*, Phys. Rev. Lett. **88**(9), 093601 (2002).

[79] R. Schnabel, W. P. Bowen, N. Treps, T. C. Ralph, H.-A. Bachor, and P. K. Lam, *Stokes-operator-squeezed continuous-variable polarization states*, Phys. Rev. A **67**(1), 012316 (2003).

[80] P. Grangier, R. E. Slusher, B. Yurke, and A. LaPorta, *Squeezed-light-enhanced polarization interferometer*, Phys. Rev. Lett. **59**(19), 2153 (1987).

[81] J. L. Sørensen, J. Hald, and E. S. Polzik, *Quantum Noise of an Atomic Spin Polarization Measurement*, Phys. Rev. Lett. **80**(16), 3487 (1998).

[82] U. Leonhardt, *Measuring the Quantum State of Light* (Cambridge Univ. Press, 1997).

[83] B. Yurke, S. L. McCall, and J. R. Klauder, *SU(2) and SU(1,1) interferometers*, Phys. Rev. A **33**(6), 4033 (1986).

[84] J. Gea-Banacloche and G. Leuchs, *Squeezed States for Interferometric Gravitational-wave Detectors*, J. Mod. Opt. **34**(6-7), 793 (1987).

[85] M. Faraday, *On the magnetization of light and the illumination of magnetic lines of force*, Philos. Trans. R. Soc. London **136**(1) (1846).

[86] P. Siddons, N. C. Bell, Y. Cai, C. S. Adams, and I. G. Hughes, *A gigahertz-bandwidth atomic probe based on the slow-light Faraday effect*, Nature Photon. **3**(4), 225 (2009).

[87] P. Siddons, C. S. Adams, and I. G. Hughes, *Optical control of Faraday rotation in hot Rb vapor*, Phys. Rev. A **81**(4), 043838 (2010).

[88] D. Budker, W. Gawlik, D. F. Kimball, S. M. Rochester, V. V. Yashchuk, and A. Weis, *Resonant nonlinear magneto-optical effects in atoms*, Rev. Mod. Phys. **74**(4), 1153 (2002).

[89] M. Koschorreck, M. Napolitano, B. Dubost, and M. W. Mitchell, *Quantum Nondemolition Measurement of Large-Spin Ensembles by Dynamical Decoupling*, Phys. Rev. Lett. **105**(9), 093602 (2010).

[90] W. Happer, *Optical Pumping*, Rev. Mod. Phys. **44**(2), 169 (1972).

[91] W. Gawlik, J. Kowalski, R. Neumann, and H. B. Wiegemann, *A new method for measuring oscillator strengths using the resonant Faraday effect in monochromatic light*, J. Phys. B: At. Mol. Opt. Phys. **12**(23), 3873 (1979).

[92] I. Hirano, *Forward scattering magneto-optical spectra of the Cs D2 line*, Phys. Rev. A **50**(6), 4650 (1994).

[93] I. Hirano, *Forward-scattering magneto-optical effects*, Phys. Rev. A **52**(5), 3594 (1995).

[94] M. B. Nasr, S. Carrasco, B. E. A. Saleh, A. V. Sergienko, M. C. Teich, J. P. Torres, L. Torner, D. S. Hum, and M. M. Fejer, *Ultrabroadband Biphotons Generated via Chirped Quasi-Phase-Matched Optical Parametric Down-Conversion*, Phys. Rev. Lett. **100**(18), 183601 (2008).

[95] N. Piro, F. Rohde, C. Schuck, M. Almendros, J. Huwer, J. Ghosh, A. Haase, M. Hennrich, F. Dubin, and J. Eschner, *Heralded single-photon absorption by a single atom*, Nature Phys. **7**(1), 17 (2011).

[96] Y. J. Lu, R. L. Campbell, and Z. Y. Ou, *Mode-Locked Two-Photon States*, Phys. Rev. Lett. **91**(16), 163602 (2003).

[97] M. Oberparleiter and H. Weinfurter, *Cavity-enhanced generation of polarization-entangled photon pairs*, Opt. Commun. **183**(1-4), 133 (2000).

[98] H. Wang, T. Horikiri, and T. Kobayashi, *Polarization-entangled mode-locked photons from cavity-enhanced spontaneous parametric down-conversion*, Phys. Rev. A **70**(4), 043804 (2004).

[99] J. S. Neergaard-Nielsen, B. M. Nielsen, H. Takahashi, A. I. Vistnes, and E. S. Polzik, *High purity bright single photon source*, Opt. Express **15**(13), 7940 (2007).

[100] M. Scholz, F. Wolfgramm, U. Herzog, and O. Benson, *Narrow-band single photons from a single-resonant optical parametric oscillator far below threshold*, Appl. Phys. Lett. **91**(19), 191104, 191104 (2007).

[101] F. Wolfgramm, X. Xing, A. Cerè, A. Predojević, A. M. Steinberg, and M. W. Mitchell, *Bright filter-free source of indistinguishable photon pairs*, Opt. Express **16**(22), 18145 (2008).

[102] X.-H. Bao, Y. Qian, J. Yang, H. Zhang, Z.-B. Chen, T. Yang, and J.-W. Pan, *Generation of Narrow-Band Polarization-Entangled Photon Pairs for Atomic Quantum Memories*, Phys. Rev. Lett. **101**(19), 190501, 190501 (2008).

[103] J. S. Neergaard-Nielsen, B. M. Nielsen, C. Hettich, K. Mølmer, and E. S. Polzik, *Generation of a Superposition of Odd Photon Number States for Quantum Information Networks*, Phys. Rev. Lett. **97**(8), 083604 (2006).

[104] F. Wolfgramm, A. Cerè, and M. W. Mitchell, *NOON states from cavity-enhanced down-conversion: high quality and super-resolution*, J. Opt. Soc. Am. B **27**(6), A25 (2010).

[105] H. Zhang, X.-M. Jin, J. Yang, H.-N. Dai, S.-J. Yang, T.-M. Zhao, J. Rui, Y. He, X. Jiang, F. Yang, *et al.*, *Preparation and storage of frequency-uncorrelated entangled photons from cavity-enhanced spontaneous parametric downconversion*, Nature Photon. **5**(10), 628 (2011).

[106] R. V. Pound, *Electronic Frequency Stabilization of Microwave Oscillators*, Rev. Sci. Instrum. **17**(11), 490 (1946).

[107] G. C. Bjorklund, M. D. Levenson, W. Lenth, and C. Ortiz, *Frequency modulation (FM) spectroscopy*, Appl. Phys. B **32**(3), 145 (1983).

[108] R. W. P. Drever, J. L. Hall, F. V. Kowalski, J. Hough, G. M. Ford, A. J. Munley, and H. Ward, *Laser phase and frequency stabilization using an optical resonator*, Appl. Phys. B **31**, 97 (1983).

[109] W. Wiechmann, S. Kubota, T. Fukui, and H. Masuda, *Refractive-index temperature derivatives of potassium titanyl phosphate*, Opt. Lett. **18**(15), 1208 (1993).

[110] A. Predojević, *Rubidium resonant squeezed light from a diode-pumped optical-parametric oscillator*, Ph.D. thesis, Universitat Politècnica de Catalunya (2009).

[111] M. H. Rubin, D. N. Klyshko, Y. H. Shih, and A. V. Sergienko, *Theory of two-photon entanglement in type-II optical parametric down-conversion*, Phys. Rev. A **50**(6), 5122 (1994).

[112] W. P. Grice and I. A. Walmsley, *Spectral information and distinguishability in type-II down-conversion with a broadband pump*, Phys. Rev. A **56**(2), 1627 (1997).

[113] Z.-Y. J. Ou, *Multi-Photon Quantum Interference* (Springer, 2007).

[114] Z. Y. Ou and L. Mandel, *Further evidence of nonclassical behavior in optical interference*, Phys. Rev. Lett. **62**(25), 2941 (1989).

[115] M. D. Eisaman, A. Andre, F. Massou, M. Fleischhauer, A. S. Zibrov, and M. D. Lukin, *Electromagnetically induced transparency with tunable single-photon pulses*, Nature **438**(7069), 837 (2005).

[116] H. de Riedmatten, M. Afzelius, M. U. Staudt, C. Simon, and N. Gisin, *A solid-state light-matter interface at the single-photon level*, Nature **456**(7223), 773 (2008).

[117] M. P. Hedges, J. J. Longdell, Y. Li, and M. J. Sellars, *Efficient quantum memory for light*, Nature **465**(7301), 1052 (2010).

[118] A. Cerè, V. Parigi, M. Abad, F. Wolfgramm, A. Predojević, and M. W. Mitchell, *Narrowband tunable filter based on velocity-selective optical pumping in an atomic vapor*, Opt. Lett. **34**(7), 1012 (2009).

[119] F. Wolfgramm, Y. A. de Icaza Astiz, F. A. Beduini, A. Cerè, and M. W. Mitchell, *Atom-Resonant Heralded Single Photons by Interaction-Free Measurement*, Phys. Rev. Lett. **106**(5), 053602 (2011).

[120] A. Elitzur and L. Vaidman, *Quantum mechanical interaction-free measurements*, Found. Phys. **23**, 987 (1993).

[121] L. Vaidman, *On the realization of interaction-free-measurements*, Quantum Opt. **6**, 119 (1994).

[122] P. Kwiat, H. Weinfurter, T. Herzog, A. Zeilinger, and M. A. Kasevich, *Interaction-Free Measurement*, Phys. Rev. Lett. **74**(24), 4763 (1995).

[123] P. G. Kwiat, A. G. White, J. R. Mitchell, O. Nairz, G. Weihs, H. Weinfurter, and A. Zeilinger, *High-Efficiency Quantum Interrogation Measurements via the Quantum Zeno Effect*, Phys. Rev. Lett. **83**(23), 4725 (1999).

[124] G. S. Paraoanu, *Interaction-Free Measurements with Superconducting Qubits*, Phys. Rev. Lett. **97**(18), 180406 (2006).

[125] A. G. White, J. R. Mitchell, O. Nairz, and P. G. Kwiat, *"Interaction-free" imaging*, Phys. Rev. A **58**(1), 605 (1998).

[126] O. Hosten, M. T. Rakher, J. T. Barreiro, N. A. Peters, and P. G. Kwiat, *Counterfactual quantum computation through quantum interrogation*, Nature **439**(7079), 949 (2006).

[127] G. Mitchison and R. Jozsa, *The limits of counterfactual computation*, arXiv:quant-ph/0606092 (2007).

[128] L. Vaidman, *Impossibility of the Counterfactual Computation for All Possible Outcomes*, Phys. Rev. Lett. **98**(16), 160403 (2007).

[129] T. Nagata, R. Okamoto, J. L. O'Brien, K. Sasaki, and S. Takeuchi, *Beating the Standard Quantum Limit with Four-Entangled Photons*, Science **316**(5825), 726 (2007).

[130] J. C. F. Matthews, A. Politi, A. Stefanov, and J. L. O'Brien, *Manipulation of multiphoton entanglement in waveguide quantum circuits*, Nature Photon. **3**(6), 346 (2009).

[131] I. K. Kominis, T. W. Kornack, J. C. Allred, and M. V. Romalis, *A subfemtotesla multichannel atomic magnetometer*, Nature **422**(6932), 596 (2003).

[132] F. Wolfgramm, C. Vitelli, F. A. Beduini, N. Godbout, and M. W. Mitchell, *Entanglement-enhanced non-destructive probing of an atomic ensemble*, submitted (2011).

[133] D. A. Steck, *Rubidium 87 D Line Data* (2001), `http://steck.us/alkalidata`.

[134] D. A. Steck, *Rubidium 85 D Line Data* (2001), `http://steck.us/alkalidata`.

[135] N. Thomas-Peter, B. J. Smith, A. Datta, L. Zhang, U. Dorner, and I. A. Walmsley, *Real-World Quantum Sensors: Evaluating Resources for Precision Measurement*, Phys. Rev. Lett. **107**(11), 113603 (2011).

[136] A. E. Lita, A. J. Miller, and S. W. Nam, *Counting near-infrared single-photons with 95% efficiency*, Opt. Express **16**(5), 3032 (2008).

[137] H. Vahlbruch, M. Mehmet, S. Chelkowski, B. Hage, A. Franzen, N. Lastzka, S. Gossler, K. Danzmann, and R. Schnabel, *Observation of Squeezed Light with 10-dB Quantum-Noise Reduction*, Phys. Rev. Lett. **100**(3), 033602 (2008).

[138] L. K. Shalm, R. B. A. Adamson, and A. M. Steinberg, *Squeezing and over-squeezing of triphotons*, Nature **457**(7225), 67 (2009).

[139] A. Ourjoumtsev, A. Kubanek, M. Koch, C. Sames, P. W. H. Pinkse, G. Rempe, and K. Murr, *Observation of squeezed light from one atom excited with two photons*, Nature **474**(7353), 623 (2011).

[140] A. Zavatta, S. Viciani, and M. Bellini, *Quantum-to-Classical Transition with Single-Photon-Added Coherent States of Light*, Science **306**(5696), 660 (2004).

[141] V. Parigi, A. Zavatta, M. Kim, and M. Bellini, *Probing Quantum Commutation Rules by Addition and Subtraction of Single Photons to/from a Light Field*, Science **317**(5846), 1890 (2007).

[142] M. Xiao, L.-A. Wu, and H. J. Kimble, *Precision measurement beyond the shot-noise limit*, Phys. Rev. Lett. **59**(3), 278 (1987).

[143] E. S. Polzik, J. Carri, and H. J. Kimble, *Spectroscopy with squeezed light*, Phys. Rev. Lett. **68**(20), 3020 (1992).

[144] K. McKenzie, D. A. Shaddock, D. E. McClelland, B. C. Buchler, and P. K. Lam, *Experimental Demonstration of a Squeezing-Enhanced Power-Recycled Michelson Interferometer for Gravitational Wave Detection*, Phys. Rev. Lett. **88**(23), 231102 (2002).

[145] K. Goda, O. Miyakawa, E. E. Mikhailov, S. Saraf, R. Adhikari, K. McKenzie, R. Ward, S. Vass, A. J. Weinstein, and N. Mavalvala, *A quantum-enhanced prototype gravitational-wave detector*, Nature Phys. **4**(6), 472 (2008).

[146] A. Foltynowicz, T. Ban, P. Masłowski, F. Adler, and J. Ye, *Quantum-Noise-Limited Optical Frequency Comb Spectroscopy*, Phys. Rev. Lett. **107**(23), 233002 (2011).

[147] G. A. Sanders, M. G. Prentiss, and S. Ezekiel, *Passive ring resonator method for sensitive inertial rotation measurements in geophysics and relativity*, Opt. Lett. **6**(11), 569 (1981).

[148] M. Auzinsh, D. Budker, D. F. Kimball, S. M. Rochester, J. E. Stalnaker, A. O. Sushkov, and V. V. Yashchuk, *Can a Quantum Nondemolition Measurement Improve the Sensitivity of an Atomic Magnetometer?*, Phys. Rev. Lett. **93**(17), 173002 (2004).

[149] I. K. Kominis, *Sub-Shot-Noise Magnetometry with a Correlated Spin-Relaxation Dominated Alkali-Metal Vapor*, Phys. Rev. Lett. **100**(7), 073002 (2008).

[150] W. Wasilewski, K. Jensen, H. Krauter, J. J. Renema, M. V. Balabas, and E. S. Polzik, *Quantum Noise Limited and Entanglement-Assisted Magnetometry*, Phys. Rev. Lett. **104**(13), 133601 (2010).

[151] A. Kuzmich, K. Mølmer, and E. S. Polzik, *Spin Squeezing in an Ensemble of Atoms Illuminated with Squeezed Light*, Phys. Rev. Lett. **79**(24), 4782 (1997).

[152] A. Kuzmich, N. P. Bigelow, and L. Mandel, *Atomic quantum nondemolition measurements and squeezing*, Europhys. Lett. **42**(5), 481 (1998).

[153] D. V. Kupriyanov and I. M. Sokolov, *Optical detection of magnetic resonance by classical and squeezed light*, Quantum Optics: Journal of the European Optical Society Part B **4**(1), 55 (1992).

[154] P. J. Windpassinger, D. Oblak, U. B. Hoff, A. Louchet, J. Appel, N. Kjærgaard, and E. S. Polzik, *Squeezing of atomic quantum projection noise*, J. Mod. Opt. **56**(18), 1993 (2009).

[155] M. H. Schleier-Smith, I. D. Leroux, and V. Vuletić, *States of an Ensemble of Two-Level Atoms with Reduced Quantum Uncertainty*, Phys. Rev. Lett. **104**(7), 073604 (2010).

[156] I. D. Leroux, M. H. Schleier-Smith, and V. Vuletić, *Implementation of Cavity Squeezing of a Collective Atomic Spin*, Phys. Rev. Lett. **104**(7), 073602 (2010).

[157] C. Gross, T. Zibold, E. Nicklas, J. Estève, and M. K. Oberthaler, *Nonlinear atom interferometer surpasses classical precision limit*, Nature **464**(7292), 1165 (2010).

[158] M. F. Riedel, P. Böhi, Y. Li, T. W. Hänsch, A. Sinatra, and P. Treutlein, *Atom-chip-based generation of entanglement for quantum metrology*, Nature **464**(7292), 1170 (2010).

[159] F. Wolfgramm, A. Cerè, F. A. Beduini, A. Predojevic, M. Koschorreck, and M. W. Mitchell, *Squeezed-Light Optical Magnetometry*, Phys. Rev. Lett. **105**(5), 053601 (2010).

[160] R. C. Hilborn, L. R. Hunter, K. Johnson, S. K. Peck, A. Spencer, and J. Watson, *Atomic barium and cesium alignment-to-orientation conversion in external electric and magnetic fields*, Phys. Rev. A **50**(3), 2467 (1994).

[161] D. Budker, D. F. Kimball, S. M. Rochester, and V. V. Yashchuk, *Nonlinear Magneto-optical Rotation via Alignment-to-Orientation Conversion*, Phys. Rev. Lett. **85**(10), 2088 (2000).

[162] D. Budker, D. F. Kimball, S. M. Rochester, V. V. Yashchuk, and M. Zolotorev, *Sensitive magnetometry based on nonlinear magneto-optical rotation*, Phys. Rev. A **62**(4), 043403 (2000).

[163] D. Budker, D. J. Orlando, and V. Yashchuk, *Nonlinear laser spectroscopy and magneto-optics*, Am. J. Phys. **67**(7), 584 (1999).

[164] A. Predojević, Z. Zhai, J. M. Caballero, and M. W. Mitchell, *Rubidium resonant squeezed light from a diode-pumped optical-parametric oscillator*, Phys. Rev. A **78**(6), 063820 (2008).

[165] H. Yonezawa, K. Nagashima, and A. Furusawa, *Generation of squeezed light with a monolithic optical parametric oscillator: Simultaneous achievement of phase matching and cavity resonance by temperature control*, Opt. Express **18**(19), 20143 (2010).

[166] K. McKenzie, E. E. Mikhailov, K. Goda, P. K. Lam, N. Grosse, M. B. Gray, N. Mavalvala, and D. E. McClelland, *Quantum noise locking*, J. Opt. B **7**(10), S421 (2005).

[167] M. Lombardi, *Création d'orientation par combinaison de deux alignements alignement et orientation des niveaux excités d'une décharge haute fréquence*, J. Phys. (Les Ulis, Fr.) **30**(8-9), 631 (1969).

[168] M. Fleischhauer, A. B. Matsko, and M. O. Scully, *Quantum limit of optical magnetometry in the presence of ac Stark shifts*, Phys. Rev. A **62**(1), 013808 (2000).

[169] J. Ries, B. Brezger, and A. I. Lvovsky, *Experimental vacuum squeezing in rubidium vapor via self-rotation*, Phys. Rev. A **68**(2), 025801 (2003).

[170] M. Fleischhauer and M. D. Lukin, *Quantum memory for photons: Dark-state polaritons*, Phys. Rev. A **65**(2), 022314 (2002).

[171] A. Dantan and M. Pinard, *Quantum-state transfer between fields and atoms in electromagnetically induced transparency*, Phys. Rev. A **69**(4), 043810 (2004).

[172] M. Scholz, L. Koch, R. Ullmann, and O. Benson, *Single-mode operation of a high-brightness narrow-band single-photon source*, Appl. Phys. Lett. **94**(20), 201105 (2009).

[173] R. J. Sewell, M. Koschorreck, M. Napolitano, B. Dubost, N. Behbood, and M. W. Mitchell, *Spin-squeezing of a large-spin system via QND measurement*, arXiv:quant-ph/1111.6969 (2011).

[174] M. Napolitano, M. Koschorreck, B. Dubost, N. Behbood, R. J. Sewell, and M. W. Mitchell, *Interaction-based quantum metrology showing scaling beyond the Heisenberg limit*, Nature **471**(7339), 486 (2011).

[175] J. A. Zielińska, F. A. Beduini, N. Godbout, and M. W. Mitchell, *Ultra-Narrow Faraday Rotation Filter at the Rb D1 Line*, arXiv:quant-ph/1110.2362 (2011).

[176] T. B. Pittman, Y. H. Shih, D. V. Strekalov, and A. V. Sergienko, *Optical imaging by means of two-photon quantum entanglement*, Phys. Rev. A **52**(5), R3429 (1995).

[177] S. Lloyd, *Enhanced Sensitivity of Photodetection via Quantum Illumination*, Science **321**(5895), 1463 (2008).

[178] The LIGO Scientific Collaboration, *A gravitational wave observatory operating beyond the quantum shot-noise limit*, Nature Phys. **7**(12), 962 (2011).

[179] V. Shah, S. Knappe, P. D. D. Schwindt, and J. Kitching, *Subpicotesla atomic magnetometry with a microfabricated vapour cell*, Nature Photon. **1**(11), 649 (2007).

[180] L.-M. Duan, M. D. Lukin, J. I. Cirac, and P. Zoller, *Long-distance quantum communication with atomic ensembles and linear optics*, Nature **414**(6862), 413 (2001).

[181] N. Sangouard, C. Simon, H. de Riedmatten, and N. Gisin, *Quantum repeaters based on atomic ensembles and linear optics*, Rev. Mod. Phys. **83**(1), 33 (2011).

[182] C. Simon, M. Afzelius, J. Appel, A. Boyer de la Giroday, S. J. Dewhurst, N. Gisin, C. Y. Hu, F. Jelezko, S. Kröll, J. H. Müller, *et al.*, *Quantum memories*, Eur. Phys. J. D **58**(1), 1 (2010).

[183] A. I. Lvovsky, B. C. Sanders, and W. Tittel, *Optical quantum memory*, Nature Photon. **3,**, 706, 1002.4659 (2010).

[184] B. Julsgaard, J. Sherson, J. I. Cirac, J. Fiurasek, and E. S. Polzik, *Experimental demonstration of quantum memory for light*, Nature **432**(7016), 482 (2004).

[185] K. F. Reim, J. Nunn, V. O. Lorenz, B. J. Sussman, K. C. Lee, N. K. Langford, D. Jaksch, and I. A. Walmsley, *Towards high-speed optical quantum memories*, Nature Photon. **4**(4), 218 (2010).

[186] K. F. Reim, P. Michelberger, K. C. Lee, J. Nunn, N. K. Langford, and I. A. Walmsley, *Single-Photon-Level Quantum Memory at Room Temperature*, Phys. Rev. Lett. **107**(5), 053603 (2011).

[187] B. Lauritzen, J. Minář, H. de Riedmatten, M. Afzelius, N. Sangouard, C. Simon, and N. Gisin, *Telecommunication-Wavelength Solid-State Memory at the Single Photon Level*, Phys. Rev. Lett. **104**(8), 080502 (2010).

[188] C. Clausen, I. Usmani, F. Bussieres, N. Sangouard, M. Afzelius, H. de Riedmatten, and N. Gisin, *Quantum storage of photonic entanglement in a crystal*, Nature **469**(7331), 508 (2011).

El Manchester es el actual campeón y es un equipo increíble, con un entrenador con enorme experiencia. Pero nosotros somos el Barcelona.

– Pep Guardiola, *before the Champions League Final 2009*

Acknowledgments

The work presented in this thesis has been made possible thanks to the support and guidance by many people.

First of all, I want to express my deep gratitude to Morgan Mitchell, who has advised this thesis and has been a great teacher and mentor. It has been a privilege and a pleasure to work with him and to learn from his vast knowledge and amazing wisdom.

I am also indebted to Alessandro Cerè, who I have worked with during the first three years of my time at ICFO. Without his hard work and commitment, it would not have been possible to achieve our ambitious goals. I consider myself very fortunate to have worked with and learned from such an experienced scientist. I thank him for his invaluable support, advice and friendship.

I want to thank Xingxing Xing, who visited our lab for three months during which we built the SPDC cavity and measured the first HOM interference. It was a great experience to spend so many hours in the lab with someone who is so energetic, even at 2 a.m. I have learned a lot from him, e.g., that, if you never miss the last train back to Barcelona, you are wasting too much time waiting at the train station.

Furthermore, I am grateful to all the people who have worked with me in the lab over the last years: Federica Beduini, Yannick de Icaza Astiz, Gianvito Lucivero, Chiara Vitelli, Nicolas Godbout, Valentina Parigi, Jeff Lundeen, José Gabriel Aguirre, Ana Predojević, Zehui Zhai, Marta Abad, and Marduk Bolaños.

Certainly, I also want to thank the present and previous members of the other half of our group, working in the 'atoms lab', for their unconditional support and all the stimulating discussions about physics and beyond:

Marco Koschorreck, Mario Napolitano, Brice Dubost, Naeimeh Behbood, Rob Sewell, Giorgio Colangelo, Silvana Palacios Álvarez, Sebastián de Echaniz, Marcin Kubasik, and Klaus Reim.

In summer 2008, Aephraim Steinberg invited me to join his group at the University of Toronto for three months. This was a fantastic experience, both on a professional as well as on a personal level. I thank him and all the people of the Toronto group for their hospitality and kindness, especially Krister Shalm, Rob Adamson, Luciano Cruz, Chris Ellenor, Chris Paul, Chao Zhuang, Rockson Chang, and Samansa Maneshi.

I am grateful to Hugues de Riedmatten and his group, especially Julia Fekete and Matteo Cristiani, for adopting me at lunch time and for interesting discussions about single-photon sources and quantum memories.

ICFO is a unique place for research. I like to thank the director and management of ICFO and all the people working in the administration, IT unit, electronic workshop and mechanical workshop for doing a great job in helping us scientists to concentrate on science by relieving us from most of the other work. Moreover, I want to thank everyone who made my stay at ICFO so stimulating and pleasant: the 'German office': Lars Neumann, Sibylle Braungardt, Danny Krautz for a good start at ICFO and nice 'office parties' as well as Omid Kokabee, who joined our office later, Alejandra Valencia, Clara Inés Osorio Tamayo, Marc Jofre, Fabian Steinlechner, Eleonora Nagali, Nicolas Piro, Hannes Gothe, Jan Huwer, Mathieu Alloing, Martin Hendrych, François Dubin, Felix Rohde, Markus Hennrich, Srdjan Aćimović, Mark Kreuzer, Osamu Takayama, Jana Nieder, Giorgio Volpe, Udo Weigel, Laura Grau, Adolfo Esteban Martín, Chaitanya Kumar Suddapalli, Ossi Kimmelma, Jan Gieseler, Daan Brinks, Candan Aydin, Jan Renger, Taisuke Minagawa, Sukanya Randhawa, Sotiris Psilodimitrakopoulos, and Francesca Arcara.

I owe a huge debt of thanks to Peter Zieger, Adriana Acevedo and Michael Marien for their friendship and their generous help and advice throughout the last years.

Of course, this work would not have been possible without support by my family, especially by my parents Lothar and Monika, my aunt Renate and my brother Ronald and his family.

Finally, very special thanks go to Alicja for her love and invaluable support and for waiting for me for almost 4 years in Berlin.